

Copyright
by
Drew Ryan Jones
2013

The Dissertation Committee for Drew Ryan Jones
certifies that this is the approved version of the following dissertation:

**A Dynamical Systems Theory Analysis of
Coulomb Spacecraft Formations**

Committee:

Cesar Ocampo, Supervisor

Hanspeter Schaub, Supervisor

Ryan Russell

Todd Humphreys

David Hull

**A Dynamical Systems Theory Analysis of
Coulomb Spacecraft Formations**

by

Drew Ryan Jones, B.S.E., M.S.E.

DISSERTATION

Presented to the Faculty of the Graduate School of
The University of Texas at Austin
in Partial Fulfillment
of the Requirements
for the Degree of

DOCTOR OF PHILOSOPHY

THE UNIVERSITY OF TEXAS AT AUSTIN

August 2013

For my little one.

Acknowledgments

This research was made possible with Government support under and awarded by the Department of Defense (DoD), Air Force Office of Scientific Research, National Defense Science and Engineering Graduate (NDSEG) Fellowship. Therefore, I would like to express my gratitude to all people involved with this extremely enabling award. I sincerely thank each member of my dissertation committee. You all made yourselves available while challenging me to produce the very best work possible. In particular, I acknowledge my cosupervisor and advisor at UT, Dr. Cesar Ocampo, for being an inspiring figure and invigorating my thirst for knowledge. As well as my other cosupervisor, Dr. Hanspeter Schaub, for his invaluable collaboration and confident support of my work. He is an excellent person to do research with, and his passion for teaching has significantly impacted me.

I also wish to recognize Dr. Belinda Marchand (currently at Purdue University), whose course *Nonlinear Dynamical Systems* motivated portions of this investigation. Thank you Dr. Robin Vaughn, Dr. Yanping Guo, and others at the Applied Physics Laboratory for inspiration and encouragement, during the time of my internship. I wish to thank NASA's Johnson Space Center for some early graduate-level research experience, and for the knowledge I gained. Thanks to the University of Texas Graduate Studies Office and the Department of Aerospace Engineering and Engineering Mechanics for guidance and assistance throughout this endeavor.

I sincerely thank all of my colleagues at UT for providing intellectual stimulation, collaboration, and your highly respected opinions. A special thanks to Nick Bradley, Ricardo Restrepo, Sonia Hernandez, Noble Hatten, Greg Johnson, Robin Saudemont, and Ravi Mathur. Moreover, I would like to acknowledge my friend and colleague Mark Jesick for fielding many of my questions over the years, and for engaging in discussion about whatever piqued our interest, on any given day.

I wish to extend a very large and heartfelt gratitude to Duane and Anna-Lee Kamins for their unwavering support, assurance, and enthusiasm. To my many close friends, for never failing to deliver that much needed release, that laugh, and that reason to have fun. I wish to thank my sister for her love and admiration. I warmly thank my grandparents, for instilling in me their value of education, and their continual support as I pursued that value, as far as I possibly could. I am forever indebted to my parents, for bestowing their work ethic upon me, and for encouraging me to dream big. To my Mom for the calm she brings, and my Dad for the determination to push further. And most of all, I thank my incredible wife and best friend Ashlee for . . . just about everything.

A Dynamical Systems Theory Analysis of Coulomb Spacecraft Formations

Drew Ryan Jones, Ph.D.
The University of Texas at Austin, 2013

Supervisors: Cesar Ocampo
Hanspeter Schaub

Coulomb forces acting between close flying charged spacecraft provide near zero propellant relative motion control, albeit with added nonlinear coupling and limited controllability. This novel concept has numerous potential applications, but also many technical challenges. In this dissertation, two- and three-craft Coulomb formations near GEO are investigated, using a rotating Hill frame dynamical model, that includes Debye shielding and differential gravity. Aspects of dynamical systems theory and optimization are applied, for insights regarding stability, and how inherent nonlinear complexities may be beneficially exploited to maintain and maneuver these electrostatic formations.

Periodic relative orbits of two spacecraft, enabled by open-loop charge functions, are derived for the first time. These represent a desired extension to more substantially studied, constant charge, static Coulomb formations. An integral of motion is derived for the Hill frame model, and then applied in eliminating otherwise plausible periodic solutions. Stability of orbit families are evaluated using Floquet theory, and asymptotic stability is shown unattainable analytically.

Weak stability boundary dynamics arise upon adding Coulomb forces to the relative motion problem, and therefore invariant manifolds are considered, in part, to more efficiently realize formation shape changes. A methodology to formulate and solve two-craft static Coulomb formation reconfigurations, as parameter optimization problems with minimum inertial thrust, is demonstrated. Manifolds are sought to achieve discontinuous transfers, which are then differentially corrected using charge variations and impulsive thrusting. Two nonlinear programming algorithms, gradient and stochastic, are employed as solvers and their performances are compared.

Necessary and sufficient existence criteria are derived for three-craft collinear Coulomb formations, and a stability analysis is performed for the resulting discrete equilibrium cases. Each specified configuration is enabled by non-unique charge values, and so a method to compute minimum power solutions is outlined. Certain equilibrium cases are proven maintainable using only charge control, and feedback stabilized simulations demonstrate this. Practical scenarios for extending the optimal reconfiguration method are also discussed.

Lastly, particular Hill frame model trajectories are integrated in an inertial frame with primary perturbations and interpolated Debye length variations. This validates qualitative stability properties, reveals particular periodic solutions to exhibit nonlinear boundedness, and illustrates higher-fidelity solution accuracies.

Table of Contents

List of Tables	xi
List of Figures	xii
Nomenclature	xv
Chapter 1. Introduction	1
1.1 Background	1
1.1.1 Applications	3
1.1.2 Coulomb Formation Flying Concept	5
1.2 Motivation	8
1.3 Previous Coulomb Formation Flying Research	9
1.4 Dissertation Contributions and Outline	12
Chapter 2. Dynamical Model and Theoretical Background	14
2.1 Chapter Summary	14
2.2 Physics of Spacecraft Charging	15
2.2.1 Idealized Charging Model	16
2.2.2 Spacecraft Charge Control	18
2.3 General Dynamical Model	20
2.3.1 Approximate Electrostatic Model	21
2.3.2 Hill Frame Formation Dynamics	22
2.3.3 Hill Frame Constant of Motion	23
2.3.4 Two-Craft Hill Frame Constant of Motion	25
2.4 Two-Craft Reduced and Normalized Dynamics	26
2.5 Three-Craft Reduced and Normalized Dynamics	27
2.6 Dynamical Systems Theory	28
2.6.1 Linearized State Space Systems	29
2.6.1.1 Two-Craft Zero-Input Linearized Dynamics	30
2.6.1.2 Three-Craft Zero-Input Linearized Dynamics	31

2.6.2	Eigenspaces and Invariant Manifolds of Equilibria	32
2.7	The Nonlinear Parameter Optimization Problem	34
2.7.1	Stochastic Method: Particle Swarm Optimization	35
2.7.2	Gradient Based Method	37
2.8	Numerical Simulation Constants	38
Chapter 3. Periodic Two-Craft Coulomb Formation Motions		39
3.1	Chapter Summary	39
3.2	Properties of Periodic Coulomb Formations	40
3.3	Periodic Coulomb Formations via Assumed Solutions	42
3.3.1	In-Plane Periodic Motions	43
3.3.2	Orbit-Normal Periodic Motions	45
3.3.3	Full State Periodic Motions	46
3.3.4	Inadmissible Periodic Trajectories	48
3.4	Numerically Simulated Periodic Coulomb Formations	49
3.4.1	In-Plane Periodic Motions	49
3.4.2	In-Plane Periodic Motion Stability	49
3.4.3	Orbit-Normal Periodic Motions	52
3.4.4	Orbit-Normal Periodic Motion Stability	52
3.4.5	Full State Periodic Motions	53
3.4.6	Full State Periodic Motion Stability	54
3.5	Chapter Conclusions	55
Chapter 4. Optimal Two-Craft Reconfigurations along Manifolds		57
4.1	Chapter Summary	57
4.2	Motivation	58
4.3	Two-Craft Static Coulomb Formation Solutions	60
4.4	Radial and Orbit-Normal Case Invariant Manifolds	62
4.5	Optimal Reconfiguration Methodology	65
4.5.1	Particle Swarm Optimization (PSO) Method	68
4.5.2	Sequential Quadratic Programming (SQP) Method	69
4.6	Numerical Examples of Optimal Reconfigurations	71
4.6.1	PSO Method Radial Expansions and Contractions	72
4.6.2	SQP Method Radial Expansions and Contractions	74
4.6.3	Improved Optima with Alternate Problem Formulations	77

4.6.4	Orbit-Normal Expansions and Contractions	80
4.6.5	Transfers between Radial and Orbit-Normal	83
4.6.6	Evaluating the Optimal Costs	86
4.6.7	Performance of SQP versus PSO Method	87
4.7	Chapter Conclusions and Additional Considerations	89
Chapter 5. Three-Craft Collinear Static Equilibria		92
5.1	Chapter Summary	92
5.2	Three-Craft Collinear Equilibria	94
5.2.1	Necessary and Sufficient Conditions with Shielding	95
5.2.2	Computing Optimal Charges to Achieve a Desired Shape	97
5.3	Stabilizability of Radial and Along-Track Cases	99
5.3.1	Radial and Along-Track In-Plane Controllability	101
5.3.2	Radial and Along-Track Uncontrolled Modal Stability	104
5.3.2.1	Along-Track	105
5.3.2.2	Radial Case A	105
5.3.2.3	Radial Cases B and C	106
5.3.3	Sensitivity of In-Plane Controllability	107
5.4	Feedback Stabilized Configurations	108
5.5	Eigenspaces and Manifolds for Three-Craft Equilibria	112
5.5.1	Radial Out-of-Plane Instability	115
5.5.2	Orbit-Normal Out-of-Plane Instability	116
5.5.3	Invariant Manifolds	117
5.5.4	Near-Heteroclinic Orbits for Three-Craft Equilibria	120
5.6	Chapter Conclusions	123
Chapter 6. Perturbed Coulomb Formation Trajectories		125
6.1	Chapter Summary	125
6.2	Inertial Model with Primary Perturbations	126
6.2.1	Perturbation Models	127
6.2.2	Transformations from ECI to Hill Frame	130
6.3	Perturbed Coulomb Formation Numerical Simulations	130
6.3.1	Perturbed In-Plane Periodic Coulomb Formations	131
6.3.2	Perturbed Full State Periodic Coulomb Formations	135
6.3.3	Perturbed Invariant Manifolds of Two-Craft Equilibria	138
6.4	Chapter Conclusions	139

Chapter 7. Conclusions	142
7.1 Overall Summary	142
7.2 Recommended Future Work	144
7.3 Concluding Remarks	147
Appendix A. Parameterized Charge Control Bounds	150
Appendix B. Analytical Gradients	153
Bibliography	156
Vita	165

List of Tables

2.1	Numerical Simulation Constant Parameters	38
3.1	Floquet Stability of Periodic Coulomb Formations	41
4.1	Two-Craft Coulomb Formation Equilibrium Conditions	61
4.2	PSO Method Numerical Result Input Parameters	71
4.3	PSO Method Optimized Radial→Radial Transfers with $N = 3$	74
4.4	SQP Method Optimized Radial→Radial Transfers with $N = 3$	76
4.5	Permutations to PSO Method Optimal Radial→Radial Expansion	78
4.6	Permutations to SQP Method Optimal Radial→Radial Transfers	79
4.7	SQP Method Optimized Orbit-Normal→Orbit-Normal Transfers	83
4.8	SQP Method Optimized Orbit-Normal→Radial Transfers	86
4.9	SQP Method Optimal Costs versus Two Impulse Baseline Costs	88
5.1	Minimum Power Results for Three-Craft Collinear Cases	98
6.1	Coulomb Force Perturbation from Variable Debye Length	129
6.2	Planar Periodic Coulomb Formation Deviations with SRP	131
6.3	Planar Periodic Coulomb Formation Deviations with Varied Debye	134
6.4	Full State Periodic Coulomb Formation Deviations with SRP, $B_z = 2$	135
6.5	Full State Periodic Coulomb Formation Deviations with Varied Debye	136

List of Figures

1.1	Abstract Spacecraft (s/c) Charge Control Diagram	2
1.2	Outer Sphere Spacecraft Charging in a Plasma Environment ¹	2
1.3	Touchless Instrument Deployment with Coulomb Force ²	4
1.4	Example Two-Craft Coulomb Formation Concept ³	5
1.5	Basic Plasma Shielding Model	7
2.1	Net Environmental Current versus Spacecraft Potential ⁴	16
2.2	Relative Motion in the Rotating Hill Frame	20
3.1	Full State Periodic Solutions: Eq. (3.13) vs. B_z and θ	47
3.2	Planar Periodic Solution Position Histories: $A_x = 20$ m, and $\tau_p = \pi$	50
3.3	Planar Periodic Solution Potential Histories: $A_x = 20$ m, and $\tau_p = \pi$	50
3.4	Floquet Multipliers in Complex Plane versus τ_p , for $A_x = 25$ m	51
3.5	Floquet Multipliers in Complex Plane versus A_x , for $\tau_p = 0.3$	51
3.6	Orbit-Normal Periodic Solution: $z_0 = 15$ m, $A_z = 5$ m, and $\tau_p = \pi$	52
3.7	Full State Periodic Solution: $A_x = 20$ m, $A_z = 10$ m, and $B_z = 2$	53
3.8	Full State Periodic Solution Trajectories: $A_x = 20$ m and $A_z = 10$ m	54
4.1	Radial Two-Craft Coulomb Formation Equilibrium	60
4.2	Orbit-Normal Two-Craft Coulomb Formation Equilibrium	61
4.3	Radial S/C 1 and 2 Stable Manifolds W^s , Propagated 1 T_p	63
4.4	Radial S/C 1 and 2 Unstable Manifolds W^u , Propagated 1 T_p	63
4.5	Orbit-Normal S/C 1 and 2 Stable Manifolds W^s , Propagated 2 T_p	64
4.6	Orbit-Normal S/C 1 and 2 Unstable Manifolds W^u , Propagated 2 T_p	64
4.7	PSO Optimal Radial→Radial Expansion, $r = 12.5 \rightarrow 25$ m	73
4.8	PSO Optimal Radial→Radial Contraction, $r = 20 \rightarrow 10$ m	73
4.9	PSO Optimal Control for Radial→Radial Reconfigurations	74
4.10	SQP Impulsive Optimal Control for Radial→Radial, $r = 20 \rightarrow 10$ m	75
4.11	SQP Linear Optimal Control for Radial→Radial, $r = 20 \rightarrow 10$ m	75
4.12	SQP Optimal Radial→Radial Contraction, $r = 20 \rightarrow 10$ m	76

4.13	PSO Nominal Radial→Radial IG, $r = 12.5 \rightarrow 15$ m	77
4.14	Alternate IG for Radial→Radial Expansion, $r = 12.5 \rightarrow 25$ m	78
4.15	Alternate IG for Radial→Radial Contraction, $r = 20 \rightarrow 10$ m	79
4.16	SQP Optimal Orbit-Normal→Orbit-Normal, $r = 15 \rightarrow 20$ m	81
4.17	SQP Optimal Orbit-Normal→Orbit-Normal, with Craft 1→Craft 2, $r = 15 \rightarrow 20$ m	81
4.18	SQP Impulsive Optimal Control for Orbit-Normal→Orbit-Normal Ex- pansions, $r = 15 \rightarrow 20$ m	82
4.19	SQP Optimal Orbit-Normal→Orbit-Normal, $r = 25 \rightarrow 12.5$ m	82
4.20	Orbit-Normal→Radial Realignment and Expansion IG	84
4.21	SQP Optimal Orbit-Normal→Radial Realignment and Expansion, $r =$ $7.5 \rightarrow 17.5$ m	84
4.22	SQP Optimal Orbit-Normal→Radial Realignment, $r = 15$ m	85
5.1	Three-Craft Collinear Equilibrium Geometry and Notation	94
5.2	Controlled Radial Case A: Planar Position Perturbations after Initial S/C 1,3 $\Delta\mathbf{v}$ Disturbance	109
5.3	Controlled Radial Case A: Planar Position Perturbations after Initial S/C 1-3 $\Delta\mathbf{r}$ Disturbance	110
5.4	Controlled Along-Track: Planar Position Perturbations after Initial S/C 1,3 $\Delta\mathbf{v}$ Disturbance	110
5.5	Charge Histories after Initial S/C 1,3 $\Delta\mathbf{v}$ Disturbance	111
5.6	Controlled Along-Track: Planar Position Perturbations after Initial S/C 1-3 $\Delta\mathbf{r}$ Disturbances	111
5.7	Out-of-Plane Position Perturbations after Initial S/C 1-3 $\Delta\mathbf{r}$ Distur- bances	112
5.8	Three-Craft Radial Configuration Force Diagrams	115
5.9	Three-Craft Orbit-Normal Configuration Force Diagrams	116
5.10	Three-Craft Radial Case A Unstable Manifolds Propagated $1.0 T_p$, with $d_1 = 30$ m, $d_3 = 25$ m, and $\tilde{Q}_{13}^* = 1.0e^4$	117
5.11	Three-Craft Radial Case B Unstable Manifolds Propagated $0.5 T_p$, with $d_1 = 30$ m, $d_3 = 18$ m, and $\tilde{Q}_{13}^* = -2.56e^7$	118
5.12	Three-Craft Along-Track Stable Manifolds Propagated $1.0 T_p$, with $d_1 = 30$ m, $d_3 = 25$ m, and $\tilde{Q}_{13}^* = 1.0e^4$	119
5.13	Three-Craft Along-Track Unstable Manifolds Propagated $1.0 T_p$, with $d_1 = 30$ m, $d_3 = 25$ m, and $\tilde{Q}_{13}^* = 1.0e^4$	119
5.14	Three-Craft Orbit-Normal Case A Unstable Manifolds Propagated $1.0 T_p$, with $d_1 = 30$ m, and $d_3 = 25$ m, and $\tilde{Q}_{13}^* = 5.9e^6$	120

5.15	Three-Craft Orbit-Normal Case B Unstable Manifolds Propagated $1.0 T_p$, with $d_1 = 30$ m, and $d_3 = 25$ m, and $\tilde{Q}_{13}^* = 1.43e^7$	120
5.16	Along-Track Discontinuous Expansion along Manifolds Propagated $1 T_p$, with $d_1 = 30 \rightarrow 36$ m, and $d_3 = 25 \rightarrow 34$ m	121
5.17	Orbit-Normal Discontinuous Expansion along Manifolds Propagated $0.7 T_p$, with $d_1 = 20 \rightarrow 30$ m, and $d_3 = 15 \rightarrow 25$ m	122
6.1	Interpolated Debye Length at GEO versus Anomaly and K_p	128
6.2	Position Deviations for SRP Perturbed Planar Periodic Solution: Case B, $A_x = 20$ m, and $t_p = 2.4$ hrs.	132
6.3	Position Deviations for Variable Debye Length Perturbed Planar Peri- odic Solution: Case B, $A_x = 20$ m, and $t_p = 2.4$ hrs.	132
6.4	Perturbed Planar Periodic Solution Trajectory for 10 Revolutions: Case A, $A_x = 20$ m, and $t_p = 2.4$ hrs.	133
6.5	Perturbed Planar Periodic Solution Trajectory for 40 Revolutions: Case B, $A_x = 20$ m, and $t_p = 2.4$ hrs.	134
6.6	Perturbed Full State Periodic Solution Trajectory: Case B, $A_x = 10$ m, $A_z = 45$ m, $B_z = 2$, and $t_f = 296.1$ hrs.	136
6.7	Perturbed Full State Periodic Solution Trajectory: Case A, $A_x = 20$ m, $A_z = 10$ m, $B_z = 2$, and $t_f = 17.6$ hrs.	137
6.8	Perturbed Radial Equilibria S/C 1 Unstable Manifolds, for $1 T_p$	138
6.9	Perturbed Orbit-Normal Equilibria S/C 1 Unstable Manifolds, for $2 T_p$	139

Nomenclature

\mathcal{H}	Rotating Hill frame
\mathcal{N}	Earth centered inertial frame
$\hat{e}_R, \hat{e}_T, \hat{e}_N$	Radial, transverse, and normal Hill frame axes
$\hat{i}, \hat{j}, \hat{k}$	Inertial frame axes
\mathbf{A}	Linear system state propagation (Jacobian) matrix
$\mathbf{A}_c, \mathbf{A}_{uc}$	Controllable, uncontrollable state Jacobian matrices
a_d	Term denoting gravity coefficient for each axis of alignment
\mathbf{A}_F	Frobenius companion matrix of \mathbf{A}
A_x, A_y, A_z	Harmonic oscillator amplitudes
\mathbf{B}, \mathbf{B}_c	Linear system full, controllable input matrices
B_z	Integer multiplier of the orbit-normal component frequency
\mathbf{C}	Equality constraint vector
c	Speed of light
c_{ij}	Three-craft linearized dynamics coefficients
C_R	Solar radiation pressure coefficient of reflectivity
\mathbf{D}	Inequality constraint vector
d_i	Reference craft distance along Hill axis
\bar{d}_i	Distance ratios for three-craft formations
d_{ij}	Reference three-craft separation distances
E^u, E^s, E^c	Unstable, stable, and center eigenspaces
\mathbf{F}	State vector derivative

\mathbf{f}_{srp}	Solar radiation pressure acceleration
\mathbf{G}, \mathbf{H}	Quadrant matrices of the full Jacobian matrix
\mathbf{H}_0	Total inertial angular momentum vector
$\mathbf{H}_{\text{cm}}, \mathbf{H}_G$	Center of mass, relative motion components of \mathbf{H}_0
\mathbf{h}_G	Hill frame relative motion angular momentum vector
h_x, h_y, h_z	Components of the angular momentum vector \mathbf{h}_G
$I_{\text{en}}, I_{\text{out}}$	Electrical current of the environment, charge control device
J	Performance (cost) index
\mathbf{J}	Skew-symmetric matrix
$\bar{J}, \bar{J}_{\text{min}}$	Augmented performance index, overall augmented optima
\mathbf{K}	Feedback gain matrix
k_c	Coulomb constant
K_p	Weighted average index of geomagnetic activity
M, m_i	Total formation mass, individual craft mass
M_{r1}, M_{r2}, M_{r3}	Mass ratios
N	Number of discretized segments on each manifold branch
\mathbf{n}	True angular velocity vector of the formation center of mass
N_{pop}	PSO method population size
N_u, N_s, N_c	Unstable, stable, and center eigenspace dimensions
P_{out}	Power of the charge control device
\mathbf{Q}_c	Linear system controllability matrix
q_i	Net charge on a craft
Q_{ij}	Charge product between craft i and j
$\Delta Q, \dot{Q}$	Two-craft optimal charge control parameters
\mathbf{r}	Two-craft formation reference position vector

\mathbf{R}_{cm}	Inertial center of mass position vector
\mathbf{R}_i	Inertial craft position vector
$\mathbf{r}_i, \delta\mathbf{r}_i$	Hill frame craft position vector, and its variation
r_{ij}	Separation distance between crafts i and j
R_{sc}	Spherical spacecraft radius
\mathbf{T}	Rotation matrix from ECI to Hill frame
T_p	Center of mass orbit period
t_p	Dimensional time period of Coulomb formation periodic solution
Δt_q	Transition time to change a craft's net charge
$\mathbf{u}, \delta\mathbf{u}$	Formation feed-forward control vector, and its variation
\mathbf{v}_i	Position vector derivative with respect to the Hill frame (scaled)
$\Delta\mathbf{v}$	Impulsive thrust maneuver
ΔV	Sum of all impulsive maneuver magnitudes
W^u, W^s	Unstable, stable invariant manifold subspaces
\mathbf{X}	Formation state vector
$\mathbf{X}^u, \mathbf{X}^s$	Unstable, stable manifold state trajectories
$\delta\mathbf{X}$	Linear system state perturbation vector
$\delta\mathbf{X}_c, \delta\mathbf{X}_{uc}$	Controllable, uncontrollable state perturbation vectors
X_{err}	Error measure of perturbed state vector trajectory
x, y, z	Components of the reference position vector \mathbf{r}
x_i, y_i, z_i	Components of a craft position vector \mathbf{r}_i
$\mathbf{X}_p, \Delta\mathbf{X}_p$	Optimization parameter vector, parameter vector update
\mathbf{Y}	Augmented state vector
$\mathbf{Z}_p, \mathbf{Z}_{\text{min}}$	PSO method individual, global optimizers
$\boldsymbol{\alpha}, \alpha$	Penalty function weight vector, dummy variable

$\beta_I, \beta_C, \beta_S$	PSO method inertial, cognitive, and social heuristic terms
ϵ	Small impulsive maneuver magnitude to initiate manifolds
ϵ_c	PSO method convergence tolerance
$\epsilon_{\mathbf{r}}, \epsilon_{\mathbf{v}}, \epsilon_{\tilde{q}}$	Constraint tolerances for position, velocity, and charge
η	Singular value of the controllability matrix \mathbf{Q}_c
Γ	A solution curve to the nonlinear ODE system
λ_d	Debye length
μ	Gravitational constant for Earth
$\boldsymbol{\omega}, \omega$	Nominal center of mass angular velocity vector, angular rate
Φ	Linear system state transition matrix
ϕ	Spacecraft electric potential (voltage)
$\Psi(r_{ij})$	Coulomb acceleration coefficient
ρ_i	PSO method uniform random variables
Σ	Distance measure to an uncontrollable state space
σ	Floquet multiplier of Coulomb formation periodic solution
τ	Non dimensional time-like variable
$\tau_f, \tau_{\text{tot}}$	Patch point, total transfer time for optimal reconfigurations
τ_f^u, τ_f^s	Propagation time along unstable, stable manifolds
$\tau_{\text{max}}^u, \tau_{\text{max}}^s$	Maximum propagation time for unstable, stable manifolds
$\tau_{\text{min}}^u, \tau_{\text{min}}^s$	Minimum propagation time for unstable, stable manifolds
τ_p	Time period of Coulomb formation periodic solution
$\theta, \theta_x, \theta_y$	Oscillation frequencies of Coulomb formation periodic solutions
Θ	Solar flux constant for radiation pressure
Υ	Scalar weighted norm function of the manifold state discontinuity
ζ	Dummy variable

- * *Superscript* indicating a reference (nominal) solution
- ~ *Overbar* indicating a scaled quantity
- j* *Subscript* indicating a segment number and/or craft number
- k* *Subscript* indicating a state vector index along manifold

Chapter 1

Introduction

1.1 Background

Using electric and magnetic forces to control the motion of spacecraft is an emerging research area, and introduces innumerable advantages and applications, albeit with many technical challenges. The nearly propellantless electrostatic (Coulomb) and electromagnetic (Lorentz) forces are being investigated, and both rely on active charge control. Spacecraft charge control was considered as early as 1966 by Cover, Knauer, and Maurer,⁵ who propose using electrostatic forces to inflate and maintain the shape of a large reflecting mesh. Spacecraft surfaces naturally accumulate charge (and a net electric potential) due to interactions with plasma particles in space, and the net charge can be varied artificially by emitting electrons or ions into the surrounding plasma, using an electron-gun type device. The controlled and natural transfer of charge between a spherical spacecraft and the plasma is shown pictorially in Figure 1.1.

The control mechanism is based on existing technology,⁶ with charge alteration (15 – 20 kilovolt changes in potential) being successfully executed during the SCATHA⁷ and ATS⁸ missions, and currently on the CLUSTER⁹ mission. Charge can be distributed on a compact craft in a variety of ways, but for initial analyses a spherical spacecraft, with an outer conductive surface, is frequently adopted. This design provides simplicity, but is also sensible since the potential field of even non

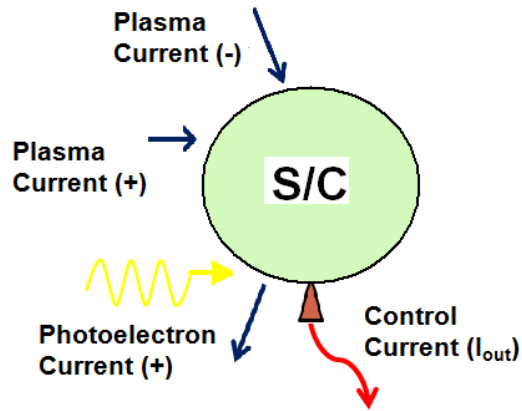


Figure 1.1: Abstract Spacecraft (s/c) Charge Control Diagram

spherical craft will approach that of a sphere at sufficiently large radial distance.^{1,4,10} With some modification an encompassing sphere may still be used in practice, since it beneficially prevents charge concentrations and acts as a Faraday cage. The conducting sphere might possibly help electrically shield interior components and prevent effects of arcing and discharge.¹¹ The outer shell could even be inflatable and use a transparent conductive film, such that sunlight could still power solar panels inside.¹⁰ Figure 1.2 diagrams this flexible and conducting outer shell concept. In which a high-

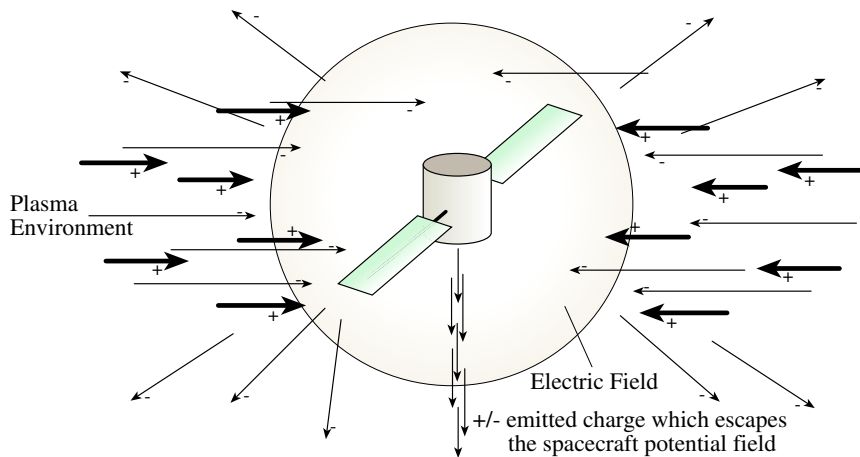


Figure 1.2: Outer Sphere Spacecraft Charging in a Plasma Environment¹

energy electron (or ion) beam is used to alter the system's potential, with respect to the environment, and where charged plasma particles can accumulate on the sphere.

The ideal Coulomb force between charged bodies is proportional to their potentials, and inversely with the square of the distance between them. In contrast, the Lorentz force acts between a charged spacecraft and a planetary magnetic field in proportion to the product of charge and magnetic field magnitude, and the speed of the moving charge relative to the magnetic field vector.¹⁰ This can provide an inertial force on a compact charged craft, capable of performing work (unlike Coulomb), due to the relative speed of the craft and the magnetic field, a concept known as Lorentz-force propulsion. The idea is similar, but not the same as, the electrodynamic tether concept in which current running along a cable interacts with the magnetic field to convert electrical energy to orbital energy (or vice versa).^{10,12} Another related proposal, but one that does not rely on natural magnetic fields, involves creating electromagnetic dipoles on spacecraft to establish and control close proximity rotating formations, in concert with reaction wheels.¹³

1.1.1 Applications

For Earth orbiting craft, the Lorentz force magnitude is significant at lower altitudes (LEO) where large orbital speeds and magnetic field strengths occur, whereas Coulomb force magnitudes tend to dominate near geostationary (GEO) altitude and beyond.^{6,10} Therefore, most Lorentz force applications occur at low altitude, and vice versa for the use of Coulomb forces. One Coulomb force (electrostatic thrusting) application of primary investigation, and the central subject of this dissertation, involves sustaining and maneuvering close proximity spacecraft formations. Tightly spaced free-flying craft have many advantages over a single large vehicle, including

overall mass reduction, shape changing ability, and multiple launches for deployment, assembly, and repair.¹

Applications for free-flying formations include Earth imaging, surveillance, telescope-occluder pairs, and separated space-borne interferometry.^{4,14} A more comprehensive literature review on this subject is presented in Section 1.1.2 and Section 1.3. Physically tethered structures with Coulomb forces acting between the nodes are studied in Ref. 15. Moorer and Schaub¹⁶ consider how an electron/ion beam from one craft could be directed at another, in order to alter its electric potential. Further electrostatic thrusting applications for free-flying craft include advanced docking and rendezvous, autonomous inspection, contactless removal of space debris,¹⁶ and the deployment/retrieval of instruments.¹⁷ The last of these applications is depicted in Figure 1.3.

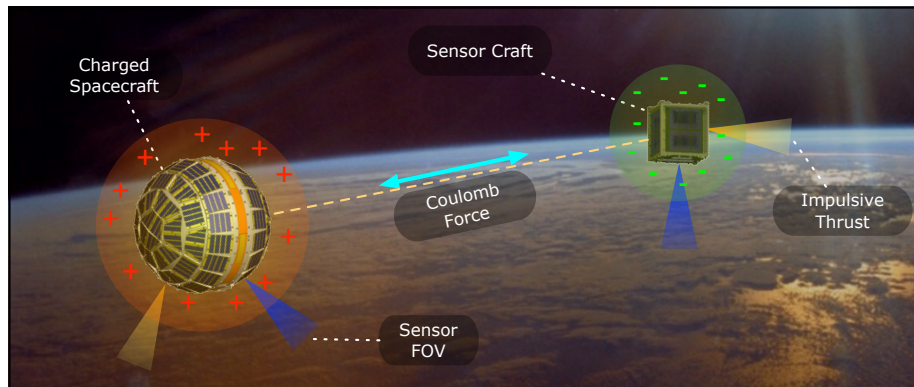


Figure 1.3: Touchless Instrument Deployment with Coulomb Force²

The Lorentz-Augmented orbit (LAO) concept introduced by Peck¹⁰ entails various potential uses including planetary escape/capture, drag and nodal precession compensation, inclination change, and synchronous orbits. LAO formation flying is also being studied, and Lorentz-force thrusting is shown capable of providing much

of the required station-keeping control effort, including partially mitigating the J_2 perturbation effect.^{10,18} All such uses are intriguing, although some would require technology advancements, for achieving higher charge per mass ratios, to be practical at Earth.

1.1.2 Coulomb Formation Flying Concept

Electric propulsion (EP) systems were initially proposed for controlling the relative motions of formation flying spacecraft. However, EP suffers from limited throttle-ability and introduces the problem of thruster plume impingement, where thruster ejecta may damage or impede neighboring craft.* The Coulomb formation concept first introduced by King et al.,^{4,19} proposes to use Coulomb forces as an alternative or supplement to EP, in sustaining and controlling the free-flying craft. Figure 1.4 shows an example two-craft Coulomb formation, illustrating its conceptual ability to address interferometry related mission objectives.

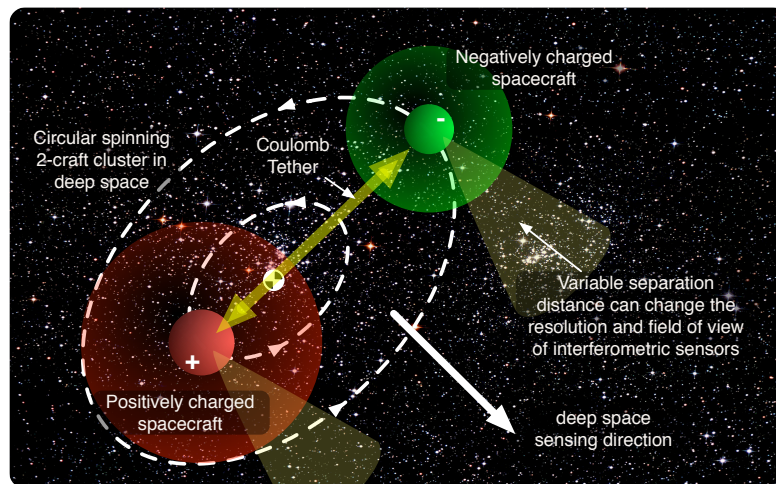


Figure 1.4: Example Two-Craft Coulomb Formation Concept³

*Thruster plume impingement is an appreciable concern only for close flying (< 500 m).

By artificially varying the electric potential (or net charge) on each vehicle, desired intercraft forces are generated with specific impulse (ISP) values as high as 10^{13} s. Moreover, electrostatic thrusting avoids thruster plumes, has fast throttling (millisecond transitions), and can sustain a given force using less power and fuel than EP.^{4,5} Of particular interest in Coulomb formation research are constant charge ‘virtual structures’, referred to as static Coulomb formations, in which craft separation distances are in equilibrium. Coulomb forces are demonstrated to be capable of establishing these invariant shapes over 10-100 meters with μN - mN force magnitudes, and using only Watt levels of power.^{1,4,17}

Unfortunately, there are certainly drawbacks to this propulsion system. First, the true (non ideal) electric field of a charged spacecraft exponentially decays due to interactions with free plasma particles, effectively shielding the Coulomb force, at distances greater than the Debye length. This may render the concept infeasible for particular orbit regimes and mission applications. A finite Debye length λ_d can approximate this shielding, such that beyond λ_d , the potential has effectively decayed to zero. Figure 1.5 depicts this simplified model, where the negatively charged sphere is encompassed by a finite sheath (yellow region) of radial distance λ_d , outside of which positive ions are no longer attracted. The highest fidelity λ_d value is dependent on the spacecraft potential as well as time varying local plasma temperature and density, but interpolated experimental data are also available in various regimes. Furthermore, the effective Debye length increases if the spacecraft potential is on the order of the ambient plasma energy, and this effect is modeled in Refs. 2, 15. Experimentally, nominal λ_d are on the order of 0.01 m at LEO, 200 m at GEO, and 10 m at Interplanetary;^{2,15} however, at GEO λ_d can be hundreds of meters larger than nominal for substantial periods of time.²⁰

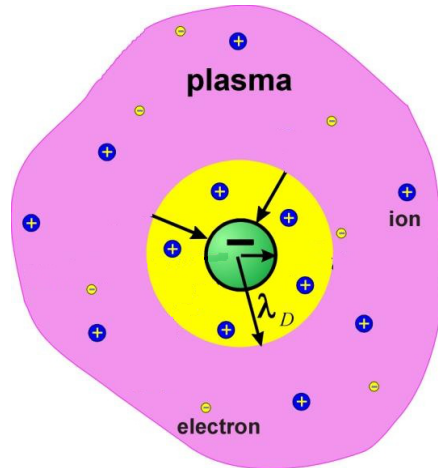


Figure 1.5: Basic Plasma Shielding Model

Another Coulomb thrusting downside, is that alone these forces are incapable of providing full controllability, and for example cannot alter the overall formation angular momentum.²¹ Therefore, it is often supplemented with inertial thrust (e.g. EP or chemical) to enable full controllability, leading to the adoption of hybrid controllers.^{22,23} Further challenges arise in accurately modeling the environment dependent Coulomb forces, which can become somewhat intractable for realistic shapes, interacting with the plasma and with other charged vehicles. Nevertheless, much data is available regarding plasma variation at GEO,²⁰ and potentials for realistic shapes have a known mathematical model in the Vlasov-Poisson partial differential equations.² High-fidelity numerical computations of controlled spacecraft charge distribution and resulting potential fields, using finite element analysis techniques and/or experimental data, are available.^{2,19,24}

Most importantly, analytical approximations and truncations have been developed and shown to be highly accurate under certain assumptions.^{2,15,25} One such truncation of the Vlasov-Poisson equations, known as the Debye-Hückel model, is

adopted in the current work, and provides an analytical force law with conservative accounting of plasma shielding.²⁶ Lastly, the near zero fuel mass for Coulomb thrusting comes at the expense of added complexity in the relative motion dynamics, since it effectively couples all spacecraft in a highly nonlinear manner.

1.2 Motivation

The primary aim of this research is to apply dynamical systems theory and optimization to Coulomb formations. Specifically in deriving natural periodic motions, reconfigurations, and stabilizing controllers. Some challenges currently plaguing Coulomb formation control are addressed, including methods for handling the added dynamical complexity, and more efficiently exploiting the ability of these free-flying forms to maneuver and change shape. Another central goal of this work is the demonstration of periodic Coulomb formation motions, which serve as natural and desired extensions of the more substantially studied static equilibria formations. These are produced by open-loop time varying potential functions, and represent the first examples of such solutions.

The beneficial asset of free-flying spacecraft formations to shape change enhances the overall system's ability to perform certain tasks and/or to assume differing 'virtual structure' geometries. Coulomb thrusting is fast throttling and nearly propellantless, and provides an advantageous means of achieving a formation geometry and for controlling relative motions. However, system controllability is limited using these internal forces, and they introduce a variety of dynamical complexities. Methods for maintaining and maneuvering the inherently unstable Coulomb formations remains a challenging and active area of research. This dissertation addresses some of these

challenges, with an umbrella objective being the preservation of certain static formation shapes, and maneuvering between those shapes, using as little inertial thrust as possible.

Dynamical systems theory aids in this endeavor by divulging modal stability properties, used to intelligently guide the design of formation-keeping and targeting control designs. It is also useful for illustrating non intuitive ways in which natural invariant system flows can be beneficially exploited. Finally, formal optimization is utilized with the goal of minimizing any necessary inertial control effort, in favor of efficient electrostatic thrusting.

All formation motions and methodologies are developed in a simplified and reduced dynamical model; however, many trajectories are simulated with higher fidelity to further validate aspects of the model. But it is left to future work to interpret these formation flying strategies in specific applications, as well as their ability to be adequately navigated in a realistic environment, with higher fidelity spacecraft potential modeling, and where certain assumptions made become unsuitable.

1.3 Previous Coulomb Formation Flying Research

A wide variety of static Coulomb formations are derived with respect to a circular reference orbit, analytically for < 5 craft (numerically otherwise), and thus far, all are dynamically unstable.^{1,4,17} Formations with motions referenced to the Hill frame, a rotating frame with origin at the formation center of mass, are considered in the most detail, generally using the linearized Clohessy-Wiltshire-Hill relative motion model.²⁷ Other known equilibrium include 3-craft forms in the absence of gravitational forces,²⁸ 2-craft forms in Newtonian and circular restricted three-body

(CRTBP) gravitational models,²³ and 2- and 3-craft spinning configurations.^{3,29} Conditions for equilibrium are not always unique, and there may be imaginary charge value solutions. For example, explicit existence criteria are defined for deep space spinning 3-craft collinear equilibria,^{28,30} but Wang and Schaub³¹ refine the solution space to be sufficiently real-valued. Berryman and Schaub,^{17,32} among others, devote much attention to Hill frame model equilibria (up to N -craft), and conclude their work, by stating that future investigations should be directed towards the derivation of dynamic, and periodic Coulomb formations. Of the many static solutions, it is the 2- and 3-craft formations admitted in Hill frame model (with gravity) which are considered in this dissertation.

Much work is devoted to analyzing the stability of these equilibria, and to developing continuous feedback controllers for maintaining them. Stability analyses are carried out for 2- and 3-craft spinning configurations,^{3,29} and stable 2-craft scenarios are identified when plasma shielding is included.³ A recent study by Hogan and Schaub demonstrate marginal in-plane stability of particular collinear spinning equilibria, if proper separation distance and speed conditions are met.²⁹ Limited Coulomb force controllability necessitates a thorough investigation of the system stability properties, in order to best utilize charge control for feedback stabilization. For example, marginal axis stability is realized during hybrid controller design for 2-craft configurations²² and 3-craft spinning equilibria.^{30,31,33,34} Natarajan and Schaub³⁵ demonstrate that radially aligned 2-craft equilibria have marginal out-of-plane stability, and that charge control alone can asymptotically stabilize in-plane perturbations. Lee, Kumar, and Bang³⁶ go further, developing a Lyapunov stable charge feedback law to maintain the separation distance and rate, for this particular equilibrium. Moreover, feedback controllers are considered for maintaining 3-craft spinning equilibria,^{30,33,34}

and CRTBP equilibrium configurations near Earth-Moon libration points.²³

Investigations into realizing the shape changing ability of Coulomb formations are few, and doing so optimally is mostly unexplored. Natarajan²⁴ presents a hybrid (Coulomb and inertial) continuous feedback law to transfer between 2-craft Hill frame configurations, and in Ref. 37 a charge feedback controller is derived to reposition N craft using $N + 3$ Coulomb spacecraft. Inampudi considers hybrid control optimal shape changes, by applying a pseudo-spectral discretization method to minimize time, fuel, and total power usage.²³ In this dissertation optimal Coulomb formation reconfigurations are formulated as explicit parameter optimization problems, in contrast to non optimal feedback controlled transfers in Ref. 24 and the implicit method of Ref. 23. The optimization problems are solved numerically with the combination of a gradient method, and a novel stochastic method, and the two types of solvers are compared. The stochastic based Particle Swarm Optimization (PSO) method, introduced by Kennedy and Eberhart,³⁸ is inspired by the motion of bird flocks searching for food. Pontani and Conway (among others) successfully apply PSO to optimal spacecraft trajectory problems including impulsive and finite-burn transfers, low-thrust maneuvers, and targeting of Lyapunov orbits in the CRTBP.³⁹

Invariant manifold theory is used in targeting the optimal reconfigurations, in a similar way to how manifolds are used to design low cost transfers, in multi-body gravity fields. For example, delicate trajectories which traverse points or orbits in the CRTBP, using little or no propellant, are well documented and are invaluable to future space missions.^{40,41} The application and use of this theory represents a paradigm shift in the way spacecraft orbits are designed, and this investigation extends the theory to relative motions of charged vehicles.

1.4 Dissertation Contributions and Outline

This dissertation is primarily composed of three independent but related papers, each considering aspects of enabling, maintaining, and maneuvering Coulomb formations. Two of the articles were presented at *AIAA/AAS* conferences,^{42,43} and versions of all three have completed peer review and are either published, or are awaiting publication, in journals.⁴⁴⁻⁴⁶ The research in Refs. 44-46 is the original work of the primary author. In addition, a fourth paper will be submitted for publication in the near future, primarily composed of the Chapter 6 work and extensions to Ref. 46, but also aspects covered in Chapters 2-5. Each of the sub-studies apply elements of dynamical systems theory and optimization to their respective investigations of Coulomb formation flying. Prior to presenting the bulk of these new contributions, Chapter 2 outlines the rotating Hill frame dynamical framework, and model assumptions adopted throughout. Some background into dynamical systems theory is covered and general linearized dynamical systems about nominal 2- and 3-craft solutions are also presented. Lastly, the type of parameter optimization problem considered here is summarized, along with methods of solution including the specific PSO method that is utilized.

In Chapter 3 the first demonstrable examples of 2-craft periodic relative orbits subject to differential gravity and electrostatic thrusting are presented.⁴⁶ Limitations or restrictions on the types of relative orbits admitted in this system are also considered, and in fact, the results apply to the more general case of spacecraft formations subject to differential gravity and conservative internal forces. Stability of the derived, open-loop, periodic Coulomb formations are considered analytically and numerically via Floquet theory,^{47,48} with asymptotic stability proven to be impossible.

Chapter 4 refers to the work in Refs. 42,44, in which a methodology is developed for formulating and solving minimum inertial control effort reconfigurations between 2-craft static Coulomb equilibria. Invariant manifolds are propagated to target discontinuous initial guess trajectories for the desired shape changes. These are then differentially corrected, with an overall objective being to more efficiently mitigate the limited Coulomb force controllability, when completing such transfers. A variety of numerically generated optimal solutions are presented, and Appendices A-B contain some detail about formulating the nonlinear parameter optimization.

Chapter 5 pertains to Refs. 43,45 and addresses the existence, stability, maintenance, and maneuvering of 3-craft static and collinear formation shapes. Necessary and sufficient existence criteria, with plasma shielding included, are derived, and a stability analysis is performed for each of the resulting equilibrium cases. Based on this analysis charge feedback stabilization laws are developed and tested for applicable cases, and possibilities for extending the optimal reconfiguration method of Chapter 4 are considered.

In Chapter 6 some simplified Hill frame model trajectories from Chapters 3-5, are repropagated using Newtonian gravity, and with the inclusion of solar radiation pressure and time variations in the Debye length parameter. This effort validates various stability claims made earlier in the dissertation, and also illustrates how solutions may translate to a higher fidelity model. Lastly, some general conclusions and a host of ideas and suggestions for continued research are given in Chapter 7.

Chapter 2

Dynamical Model and Theoretical Background

2.1 Chapter Summary

The primary purpose of this chapter is to establish a dynamical model, used throughout the dissertation, and to define the rotating Hill reference frame, in which all formation motions are presented. This framework and its inherent assumptions are described in Sections 2.2-2.3, with differential gravity and approximated (but nonlinear and partially shielded) electrostatic forces being the only modeled spacecraft accelerations. All other perturbing forces, including the Lorentz force, are reasonably neglected, with the partial exception of solar radiation pressure, a primary (but lower order) perturbation added for consideration in Chapter 6. In Section 2.3.3, a scalar integral of motion is shown to exist in the Hill frame model. This is acquired using the fact that for internally actuated formations (e.g. Coulomb formations), the total inertial angular momentum vector is conserved.²¹ This constant of motion is applied especially in Chapter 3, but also holds for N craft formations with general internal conservative forcing.

Explicit equations of motion for 2- and 3-craft Coulomb formations are given in Sections 2.4-2.5, and corresponding zero-input linearized dynamical systems about nominal solutions in Sections 2.6.1.1-2.6.1.2. Linearized systems are outlined in state space form, and the 2-craft linearization is shown to share analytical properties with the analogous linearized dynamics about libration points in the CRTBP.⁴⁹ Addition-

ally, key concepts from dynamical systems theory, which are applied in this research, are reviewed in Section 2.6. These topics include eigendecomposition analysis, invariant manifold theory, and heteroclinic orbits. Lastly, background regarding nonlinear parameter optimization, specific to this research, is covered in Section 2.7 along with nonlinear programming methods.

2.2 Physics of Spacecraft Charging

A conductive craft surface naturally exchanges ions and electrons with the plasma of space, and as a result assumes a non zero electric potential ϕ , measured in Volts relative to the ambient. The SCATHA satellite,⁷ launched in 1979, exhibited kilovolt magnitude natural potential at GEO, and therefore modern GEO spacecraft are built to accommodate such large potentials, to avoid the negative effects of differential discharge.^{1,4} Furthermore, the naturally occurring potential can be altered artificially, and this has been demonstrated on multiple missions.⁷⁻⁹ In the Coulomb formation concept, an identical control process is proposed but with the purpose of uniformly altering the absolute charge (relative to ambient) of multiple close proximity vehicles.^{1,4} First order calculations for GEO indicate that starting from $\phi = 0$, a 6 kilovolt change in spacecraft potential can be achieved in 8 msec using a mere 200 mW of power.⁴

The fundamentals of how charge naturally accumulates on a spacecraft is considered here. The net environmental current I_{en} (to the craft) consists of terms corresponding to electron and proton species (assumed as single Maxwellian distributions), as well as a photoelectric emission current. Expressions for I_{en} as a function of the temperature and density of the particles, the magnitude of ϕ , the spacecraft surface

area, and whether the vehicle is in sunlight or shadow may be found in Refs. 4,15,25. Figure 2.1 depicts the qualitative and characteristic functional dependence of envi-

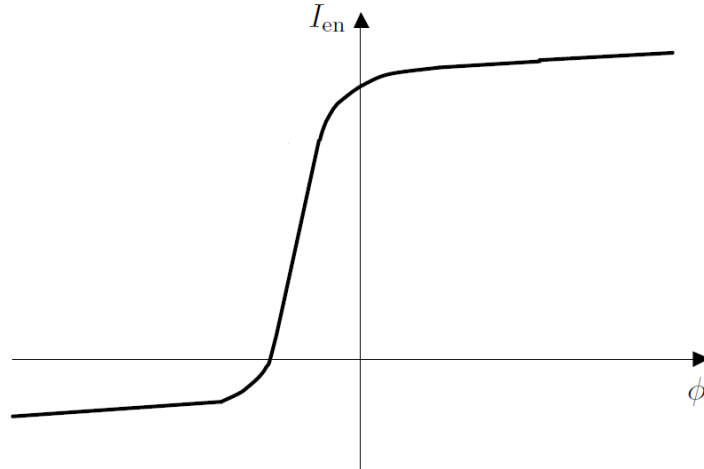


Figure 2.1: Net Environmental Current versus Spacecraft Potential⁴

ronmental current on ϕ , in stylized form. The fundamental attribute of I_{en} reaching asymptotic (saturation) limits for large $|\phi|$, may be inferred from Figure 2.1. Based on experimental and numerical data, and for a 1 m radius sphere, the worst case (maximum magnitude) environmental current is assumed to be $|I_{\text{en}}| = 80 \mu\text{A}$. This quantity is utilized throughout the investigation, and is reasonable at GEO for up to 100 kilovolt magnitude ϕ .^{4,15,25} The natural (floating) potential occurs when $I_{\text{en}} = 0$, or equivalently the crossing of the horizontal axis in Figure 2.1. This represents an equilibrium, since above this potential the natural charging tends to decrease ϕ , and below this potential the natural charge tends to increase ϕ .

2.2.1 Idealized Charging Model

When immersed in a plasma, the ideal vacuum potential of a charged body is limited (or shielded) due to interactions with free particles and photons. This results

in a sheath of surrounding (oppositely charged particles) and the Debye length λ_d parameterizes the extent of this sheath, and equivalently the strength of the shielding effect. The Debye length is approximately independent of the spacecraft ϕ for $|\phi| \ll$ the ambient plasma energy.^{2,6} Regardless, a large $|\phi|$ effectively increases λ_d , and therefore assuming λ_d to be a pure measure of environmental plasma temperature and density simply yields a conservative accounting of the plasma shielding effect.^{2,15} Further consideration of this dependence and a numerical means for modeling $\lambda_d(\phi)$ can be found in Ref. 2. Throughout this work, a nominal λ_d (independent of ϕ) is assumed and formations near GEO are also assumed such that λ_d is reasonably large (on the order of 100 m).^{2,15,20}

All spacecraft are idealized here as being spherical with equal radius R_{sc} , and having perfectly conductive outer surfaces, of uniform charge density. This spherical outer shell design is something of an abstraction, adopted in part for simplicity and for first order calculations. Computing the potentials for realistic shapes with varying charge distributions requires numerical solution of the Vlasov-Poisson partial differential equations (possibly with finite element analysis techniques), however some of these higher order considerations, including attitude dynamics, are treated in Refs. 1,4,6,15. Moreover, the capacitance of each spherical craft is assumed to be independent of its neighbors, which is reasonably accurate if the separation distances between vehicles is sufficiently large (relative to R_{sc}). The decoupled capacitance approximation is demonstrated numerically in Ref. 2 to be highly accurate for distances greater than $10R_{sc}$. Modeling the effects of coupled spacecraft potentials and capacitances, which also depend on time varying λ_d , are far beyond the scope of this research; however, such aspects can be found in Refs. 1,2,6.

These simplifications, and using the combined capacitance of the craft surface and its surrounding plasma sheath, allows for the net surface charge q to be analytically related to the potential ϕ via Eq. (2.1), where k_c is the Coulomb constant.⁶

$$q = \phi \frac{R_{sc}(R_{sc} + 3\lambda_d)}{3k_c \lambda_d} 0.05in] \quad (2.1)$$

Since formations are considered in the GEO regime, it is reasonable to assume $R_{sc} \ll \lambda_d$, and therefore plasma shielding may be considered negligible over R_{sc} . Imposing this assumption on Eq. (2.1) and rearranging yields the Eq. (2.2) expression, which relates the net surface charge q_i , on craft i , to the potential ϕ_i .^{2,24}

$$\phi_i = k_c \frac{q_i}{R_{sc}} \quad (2.2)$$

In Ref. 2, the accuracy of Eq. (2.2) is investigated numerically. Throughout this investigation, the assumptions put forth here (Section 2.2.1) are enforced to maintain a high accuracy in Eq. (2.2). But also such that the simplified electrostatic force model, described in Section 2.3.1, can be adopted, and so that reasonable spacecraft potentials are effective over larger distances.

2.2.2 Spacecraft Charge Control

To achieve and maintain an arbitrary potential, the control device must have sufficient power P_{out} to supply the desired voltage ϕ , while continuously emitting particles at a rate I_{out} , as stated in Eq. (2.3).

$$P_{out} = |\phi I_{out}(\phi)| \quad , \quad |I_{out}(\phi)| = |I_{en}(\phi)| \quad (2.3)$$

Where I_{en} is possibly time varying and complex in nature. Nevertheless, to ensure control authority the device current I_{out} must be greater or equal in magnitude than

the environmental current I_{en} (which tends to drive ϕ to natural equilibrium).^{4,6} Therefore throughout this work, power is computed using Eq. (2.4) with a constant operating current of $|I_{\text{out}}| = 80 \mu\text{A}$ (based on the worst case experimental I_{en} value for GEO).²⁵

$$P_{\text{out}} = |\phi I_{\text{out}}| , \quad |I_{\text{out}}| > |I_{\text{en}}(\phi)| \quad (2.4)$$

As such, this assumption yields conservative upper bounds on the power requirements for all Coulomb thrusting maneuvers considered. The transient response for a change in potential is governed by the Eq.(2.5) differential equation, where the approximate spacecraft capacitance from Eq. (2.1) is used.

$$\frac{d\phi}{dt} = I_{\text{out}} \frac{3k_c \lambda_d}{R_{sc}(R_{sc} + 3\lambda_d)} \quad (2.5)$$

Enforcing the $R_{sc} \ll \lambda_d$ assumption on Eq. (2.5) and assuming the constant I_{out} used in Eq. (2.4), allows the differential equation to be integrated exactly. Doing so and also substituting the Eq. (2.2) relation, yields Eq. (2.6). This therefore estimates the transition time Δt_q required to change potential by the quantity $|\Delta\phi_i|$, at an operating current of I_{out} .

$$\Delta t_q = \frac{R_{sc}|\Delta\phi_i|}{k_c |I_{\text{out}}|} = \frac{|\Delta q_i|}{|I_{\text{out}}|} \quad (2.6)$$

Throughout this dissertation, Eq. (2.4) and Eq. (2.6) are thereby used to quantify the power required and transition time needed, within the stated assumptions of this model. These therefore yield consistent high P_{out} but low Δt_q estimates. Initial low-fidelity calculations show that a GEO spacecraft ϕ can be transitioned between $\pm 36 \text{ kV}$, in less than 100 milliseconds at worst case I_{en} .²⁵ Because such transitions can occur so quickly, it is reasonable to allow discontinuous potential changes (of this order or less) when considering trajectories with durations on the order of hours (since

the craft dynamics would be negligibly affected). Such an allowance is permitted, particularly in Chapter 4.

Additionally, the q_i are considered as controls in this research, in substitution for the ϕ_i via Eq. (2.2). This despite the ϕ_i being, in practice, the more likely measurable and controllable quantities. Charge products $Q_{ij} = q_i q_j$, are also utilized as controllable parameters, and this is useful since Coulomb forces between craft are proportional to charge products, as shown in Section 2.3.2.

2.3 General Dynamical Model

With the exception of Chapter 6, interspacecraft Coulomb forces and the classical gravity force are all that are considered to be acting on the spacecraft. Coulomb force magnitudes considered here are of at least μN order, and therefore at GEO all perturbing forces are many magnitudes less, and therefore reasonably neglected.⁵⁰ For example, the geomagnetic Lorentz force is many orders of magnitude smaller at

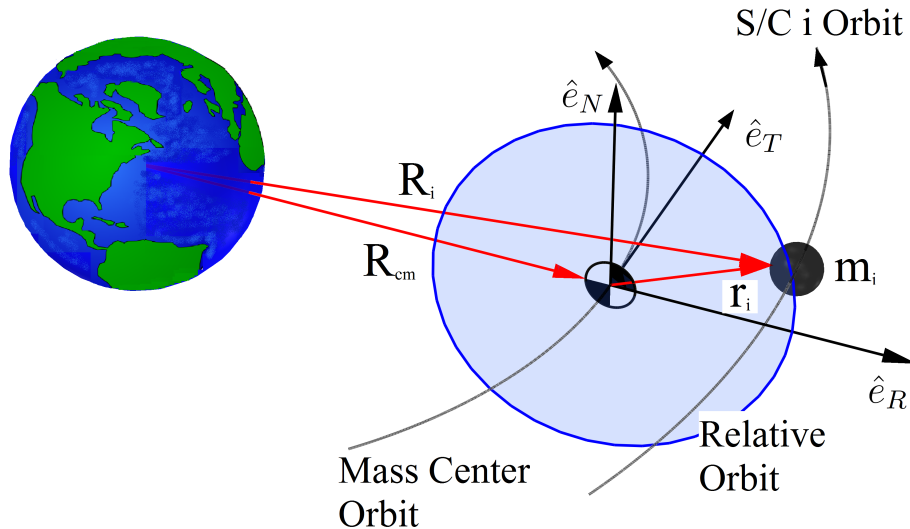


Figure 2.2: Relative Motion in the Rotating Hill Frame

GEO, than the Coulomb forces being considered.⁶ Formation dynamics are considered in the Hill frame as depicted by Figure 2.2. An Earth centered inertial frame is denoted $\mathcal{N} : \{\hat{i}, \hat{j}, \hat{k}\}$, and $\mathcal{H} : \{\hat{e}_R, \hat{e}_T, \hat{e}_N\}$ denotes the rotating Hill frame, which is centered at and rotates with a nominal center of mass (CM) orbit (assumed circular with radius R_{cm} and period T_p). The axes correspond to \hat{e}_R for radial, \hat{e}_T for transverse (along-track), and \hat{e}_N for normal (orbit-normal).

Position vectors for craft i and the formation CM, relative to the \mathcal{N} frame, are denoted \mathbf{R}_i and \mathbf{R}_{cm} , respectively. And \mathbf{r}_i denotes a craft position vector relative to \mathbf{R}_{cm} (also the origin of the \mathcal{H} frame).

$$\mathbf{R}_i = \mathbf{R}_{\text{cm}} + \mathbf{r}_i \quad (2.7)$$

$$\sum_i m_i \mathbf{r}_i = 0 \quad \mathbf{r}_i = [x_i \ y_i \ z_i]^T \quad (2.8)$$

Equation (2.7) relates the position vectors, and the Eq. (2.8) CM constraint on the \mathbf{r}_i vectors is a consequence of the \mathcal{H} frame definition. Here m_i is a craft mass, and x_i , y_i , and z_i are position vector components along the axes \hat{e}_R , \hat{e}_T , and \hat{e}_N .

2.3.1 Approximate Electrostatic Model

The electric flux of a closed surface, governed by Gauss's Law, readily shows that the potential field at any point outside the uniformly charged spherical craft, is the same as if the net charge were concentrated at the center of the sphere.⁵¹ Therefore, Coulomb forces between finite spacecraft may be modeled equivalently as forces between point charges located at the center of each sphere, and shielded by the plasma environment. Some computational consideration for more complex, albeit realistic shapes, can be found in Refs. 1, 4, 6, 15; however, in this research an

analytical force law is sought in order to achieve first order quantitative results for Coulomb formation motions.

The well established and frequently adopted Debye-Hückel approximation provides this analytical solution, and it also reflects a conservative estimate of the plasma shielding effect.²⁶ By combining this approximation with Eq. (2.2), one can obtain the Eq. (2.9) expression for the potential of charged spherical craft i , versus the the separation distance $r_{ij} = \|\mathbf{r}_i - \mathbf{r}_j\|$ between crafts i and j .

$$\phi_i(r_{ij}) = k_c \frac{q_i}{r_{ij}} \exp[-(r_{ij} - R_{sc})/\lambda_d] \quad (2.9)$$

The Coulomb force exerted by craft i on craft j is then defined as q_j times the gradient of the Eq. (2.9) potential.¹⁵ The magnitude of this force is given explicitly by Eq. (2.10), with the added assumption that $R_{sc} \ll r_{ij}$ (equivalent point charge at a distance).

$$f_{ij} = k_c \frac{q_i q_j \left(1 + \frac{r_{ij}}{\lambda_d}\right)}{r_{ij}^2 \exp[r_{ij}/\lambda_d]} \quad (2.10)$$

This approximation is demonstrated to be highly accurate under nominal GEO conditions, both experimentally and numerically, so long as the Section 2.2.1 assumptions are maintained.^{2,24} Specifically, that spacecraft capacitances' remain decoupled ($r_{ij} > 10R_{sc}$), $|\phi_i|$ be less than ambient plasma energy, and that $R_{sc} \ll \lambda_d$. Therefore to maintain model accuracy, formations are assumed in a nominal GEO regime, with r_{ij} bounded from below, and with all $|\phi_i|$ of maximum kilovolt order.

2.3.2 Hill Frame Formation Dynamics

This model assumes the linearized Clohessy-Wiltshire-Hill equations of relative motion,²⁷ with the addition of a net Coulomb acceleration defined by the Debye-

Hückel approximation.²⁶ The acceleration of craft i , with respect to the rotating Hill frame, is then given by Eq. (2.11).

$$\ddot{\mathbf{r}}_i = \frac{\kappa_d^2}{dt^2} \mathbf{r}_i = \begin{bmatrix} 2\omega\dot{y}_i + 3\omega^2 x_i \\ -2\omega\dot{x}_i \\ -\omega^2 z_i \end{bmatrix} + \frac{k_c q_i}{m_i} \sum_{\substack{j \\ j \neq i}} \frac{q_j \left(1 + \frac{r_{ij}}{\lambda_d}\right) \mathbf{r}_{ij}}{r_{ij}^3 \exp[r_{ij}/\lambda_d]} \quad (2.11)$$

Where the q_i may be related to ϕ_i via Eq. (2.2), and ω denotes the rotational rate of the reference CM orbit (and the \mathcal{H} frame rotational rate). Note that the Eq. (2.8) constraint means that one craft's motion is explicitly dependent on the others, and also that limited Coulomb force controllability is implied by Eq. (2.11), since the forces are restricted to act along line of sight vectors.

2.3.3 Hill Frame Constant of Motion

It is demonstrated here that an N -craft Coulomb formation, using the Figure 2.2 notation, and Eq. (2.11) dynamics, admits a scalar constant of motion.⁴⁶ Norman and Peck⁵² demonstrate that mechanical energy and total angular momentum are conserved, in systems acted on by central body gravity and conservative internal forces. Coulomb forces are not generally conservative, but those considered in this work are, because they are specified to depend only on generalized coordinates (i.e. the \mathbf{r}_i). Nevertheless, in general Coulomb forces cannot alter a system's inertial angular momentum vector,^{3,21,30} denoted \mathbf{H}_0 , and defined by Eq. (2.12).

$$\mathbf{H}_0 = \sum_i m_i \left(\mathbf{R}_i \times \frac{\kappa_d}{dt} \mathbf{R}_i \right) \quad (2.12)$$

The \mathbf{H}_0 vector can alternatively be written as the sum of two angular momentum terms, as in Eqs. (2.13a)-(2.13b). The terms being the momentum \mathbf{H}_{cm} associated with a total mass $M = \sum_i m_i$ on the CM orbit, and the angular momentum \mathbf{H}_G of the

particles moving with respect to the CM. It is important to note that no dynamical simplifications have been made, thus far.

$$\mathbf{H}_0 = M \left(\mathbf{R}_{\text{cm}} \times \frac{\mathcal{N}_d}{dt} \mathbf{R}_{\text{cm}} \right) + \sum_i m_i \left(\mathbf{r}_i \times \frac{\mathcal{N}_d}{dt} \mathbf{r}_i \right) \quad (2.13a)$$

$$\mathbf{H}_0 = \mathbf{H}_{\text{cm}} + \mathbf{H}_G \quad (2.13b)$$

Inherent to the Hill frame definition is the assumption that \mathbf{H}_{cm} is constant. With this assumption, Eqs. (2.13a)-(2.13b) imply that \mathbf{H}_G is constant. Also, the reference orbit plane $\hat{e}_R\text{-}\hat{e}_T$ is assumed coplanar to the $\hat{i}\text{-}\hat{j}$ plane (an arbitrary choice). Therefore, \mathcal{H} is obtained by rotating \mathcal{N} , about $\hat{k} = \hat{e}_N$, at the constant rate ω (also inherent to the Hill frame definition). The angular velocity vector of the \mathcal{H} frame is then $\boldsymbol{\omega} = \omega \hat{k} = \omega \hat{e}_N$. The vector \mathbf{H}_G transformed to the rotating Hill frame, is denoted \mathbf{h}_G . The time derivative of \mathbf{h}_G taken with respect to the \mathcal{H} frame, is computed in Eq. (2.14a), via the transport theorem. Also, \mathbf{h}_G is defined component wise (in the \mathcal{H} basis) by Eq. (2.14b).

$$\frac{\mathcal{H}_d}{dt} \mathbf{h}_G = \frac{\mathcal{N}_d}{dt} \mathbf{H}_G - (\boldsymbol{\omega} \times \mathbf{h}_G) = \begin{bmatrix} 0 \\ 0 \\ 0 \end{bmatrix} - \begin{bmatrix} -\omega h_y \\ \omega h_x \\ 0 \end{bmatrix} \quad (2.14a)$$

$${}^{\mathcal{H}}\mathbf{h}_G = [h_x \ h_y \ h_z]^T \quad (2.14b)$$

Therefore, since \mathbf{H}_G is a constant vector, h_z is a scalar constant of motion for Hill frame formations involving internal forces (e.g. Coulomb forces). This result is summarized in Eqs. (2.15a)-(2.15b), with h_z written in terms of spacecraft coordinates, and its time derivative taken with respect to the \mathcal{H} frame.

$$h_z = \sum_i m_i (x_i \dot{y}_i - y_i \dot{x}_i) \quad (2.15a)$$

$$\dot{h}_z = \frac{\mathcal{H}}{dt} h_z = \sum_i m_i (x_i \ddot{y}_i - y_i \ddot{x}_i) = 0 \quad (2.15b)$$

Position vector time derivatives $\dot{\mathbf{r}}_i$, taken with respect to the \mathcal{H} frame, are related to the inertial time derivatives, via the transport theorem, as in Eq. (2.16).

$$\dot{\mathbf{r}}_i = \frac{\mathcal{H}}{dt} \mathbf{r}_i = \frac{\mathcal{N}}{dt} \mathbf{r}_i - (\boldsymbol{\omega} \times \mathbf{r}_i) = \begin{bmatrix} \dot{x}_i \\ \dot{y}_i \\ \dot{z}_i \end{bmatrix} \quad (2.16)$$

Interestingly, conservation of only the out-of-plane component of angular momentum is a well known result in the case of spacecraft formations in a spherical gravity model, with the inclusion of J_2 .⁵³ However, in that problem it is an inertial angular momentum quantity, as opposed to the Hill frame quantity derived here.

2.3.4 Two-Craft Hill Frame Constant of Motion

For the special case of two vehicles, the Eq. (2.8) constraint can be used to eliminate one craft's state variables from Eqs. (2.15a)-(2.15b). In Eq. (2.17), the craft 2 state is written in terms of craft 1.

$$\mathbf{r}_2 = \frac{-m_1}{m_2} \mathbf{r}_1 = \frac{-m_1}{m_2} \begin{bmatrix} x_1 \\ y_1 \\ z_1 \end{bmatrix} \quad \dot{\mathbf{r}}_2 = \frac{-m_1}{m_2} \begin{bmatrix} \dot{x}_1 \\ \dot{y}_1 \\ \dot{z}_1 \end{bmatrix} \quad (2.17)$$

Upon substitution, the 2-craft integral of motion (and its \mathcal{H} frame derivative) is given by Eqs. (2.18a)-(2.18b).

$$h_z = \frac{m_1^2 + m_1 m_2}{m_2} (x_1 \dot{y}_1 - y_1 \dot{x}_1) \quad (2.18a)$$

$$0 = x_1 \ddot{y}_1 - y_1 \ddot{x}_1 \quad (2.18b)$$

2.4 Two-Craft Reduced and Normalized Dynamics

The following reduced and scaled equations of motion, simplify subsequent analyses and help reduce numerical integration error. A scaled charge product \tilde{Q}_{12} , given by Eq. (2.19), is substituted into the Eq. (2.11) expression.

$$\tilde{Q}_{12} = \frac{k_c Q_{12}}{\omega^2} \quad (2.19)$$

$$d\tau = \omega dt \quad (\zeta)' = \frac{d\zeta}{d\tau} = \frac{1}{\omega} \frac{d\zeta}{dt} \quad (2.20)$$

The scaling introduces a time transformation into the motion equations, to the non dimensional time-like variable τ . This transform is defined by Eq. (2.20), for a dummy variable ζ .

Equation (2.17) is used to explicitly remove \mathbf{r}_2 terms from the resulting craft 1 acceleration. This yields the Eq. (2.21a) reduced and normalized equations of motion for the system, with the auxiliary terms Ψ and M_{r1} defined in Eq. (2.21b).

$$\mathbf{r}_1'' = \frac{\ddot{\mathbf{r}}_1}{\omega^2} = \begin{bmatrix} 2y_1' + 3x_1 \\ -2x_1' \\ -z_1 \end{bmatrix} + \tilde{Q}_{12} \Psi(r_1) \begin{bmatrix} x_1 \\ y_1 \\ z_1 \end{bmatrix} \quad (2.21a)$$

$$\Psi(r_1) = \frac{M_{r1}^2 \left(1 + \frac{r_1}{M_{r1}\lambda_d}\right)}{m_1 r_1^3 \exp\left[\frac{r_1}{M_{r1}\lambda_d}\right]} \quad M_{r1} = \frac{m_2}{m_1 + m_2} \quad (2.21b)$$

The Eq. (2.21a) expression therefore defines the craft 1 acceleration (in the variable τ), as a function of its own position vector \mathbf{r}_1 , its own scaled velocity vector $\mathbf{v}_1 = \mathbf{r}_1' = \dot{\mathbf{r}}_1/\omega$, and \tilde{Q}_{12} . These are used throughout this dissertation when considering 2-craft Coulomb formations; however, it is often informative to consider the dimensional potential ϕ_1 (in Volts), rather than \tilde{Q}_{12} . Therefore, transformations from \tilde{Q}_{12} to the net charge q_1 (and potential ϕ_1) are given by Eq. (2.22).

$$q_1 = \omega \sqrt{\frac{|\tilde{Q}_{12}|}{k_c}} \quad \phi_1 = \frac{\omega \sqrt{k_c |\tilde{Q}_{12}|}}{R_{sc}} \quad (2.22)$$

Where positive q_1 , and equal charge magnitude ($|q_1| = |q_2|$), conventions are adopted, and Eq. (2.2) was substituted to relate q_1 to ϕ_1 .

2.5 Three-Craft Reduced and Normalized Dynamics

Again scaled charge products \tilde{Q}_{ij} , as in Eq. (2.19), are substituted into the Eq. (2.11) dynamical model, resulting in the Eq. (2.20) time transformation. Equation (2.8) is then applied to the resulting expressions, in order to explicitly remove \mathbf{r}_2 terms from craft 1 and craft 3 acceleration vectors. Those steps yield the Eqs. (2.23a)-(2.23b) acceleration vectors (in the variable τ), as a function of \mathbf{r}_1 , \mathbf{r}_3 , $\mathbf{v}_1 = \mathbf{r}'_1 = \dot{\mathbf{r}}_1/\omega$, $\mathbf{v}_3 = \mathbf{r}'_3 = \dot{\mathbf{r}}_3/\omega$, and three scaled charge products \tilde{Q}_{ij} . The auxiliary terms $\Psi(r_{ij})$, M_{r_2} , and M_{r_3} are defined by Eq. (2.23c).

$$\mathbf{r}''_1 = \begin{bmatrix} 2y'_1 + 3x_1 \\ -2x'_1 \\ -z_1 \end{bmatrix} + \frac{\tilde{Q}_{13} \Psi(r_{13})}{m_1} \begin{bmatrix} x_1 - x_3 \\ y_1 - y_3 \\ z_1 - z_3 \end{bmatrix} + \frac{\tilde{Q}_{12} \Psi(r_{12})}{m_1} \begin{bmatrix} M_{r_2} x_1 - \frac{m_3}{m_2} x_3 \\ M_{r_2} y_1 - \frac{m_3}{m_2} y_3 \\ M_{r_2} z_1 - \frac{m_3}{m_2} z_3 \end{bmatrix} \quad (2.23a)$$

$$\mathbf{r}''_3 = \begin{bmatrix} 2y'_3 + 3x_3 \\ -2x'_3 \\ -z_3 \end{bmatrix} + \frac{\tilde{Q}_{13} \Psi(r_{13})}{m_3} \begin{bmatrix} x_3 - x_1 \\ y_3 - y_1 \\ z_3 - z_1 \end{bmatrix} + \frac{\tilde{Q}_{23} \Psi(r_{23})}{m_3} \begin{bmatrix} M_{r_3} x_3 - \frac{m_1}{m_2} x_1 \\ M_{r_3} y_3 - \frac{m_1}{m_2} y_1 \\ M_{r_3} z_3 - \frac{m_1}{m_2} z_1 \end{bmatrix} \quad (2.23b)$$

$$\Psi(r_{ij}) = \frac{(1 + r_{ij}/\lambda_d)}{r_{ij}^3 \exp[r_{ij}/\lambda_d]} \quad M_{r_2} = \frac{m_1 + m_2}{m_2} \quad M_{r_3} = \frac{m_2 + m_3}{m_2} \quad (2.23c)$$

The distances r_{12} and r_{23} are left in Eqs. (2.23a)-(2.23b) to simplify the notation; however, those may be written in terms of: \mathbf{r}_1 , \mathbf{r}_3 , and the mass ratios M_{r_2} and M_{r_3} . Throughout this dissertation, scaled individual craft charges \tilde{q}_i , associated with 3-craft Coulomb formations, are computed according to the Eq. (2.24) convention,

with unscaled q_i given by Eq. (2.25).

$$\tilde{q}_1 = \sqrt{\frac{\tilde{Q}_{12}\tilde{Q}_{13}}{\tilde{Q}_{23}}} \quad \tilde{q}_2 = \frac{\tilde{Q}_{12}}{\tilde{q}_1} \quad \tilde{q}_3 = \frac{\tilde{Q}_{13}}{\tilde{q}_1} \quad (2.24)$$

$$q_i = \frac{\omega}{\sqrt{k_c}} \tilde{q}_i \quad (2.25)$$

It is inherently assumed that $\tilde{Q}_{12} \cdot \tilde{Q}_{13} \cdot \tilde{Q}_{23} > 0$, so that non imaginary individual charges result from Eq. (2.24). Detailed conditions for ensuring this to be true are derived in Chapter 5. Also, the positive \tilde{q}_1 convention is not unique, and the signs of charges in Eq. (2.24) could be reversed if desired.

2.6 Dynamical Systems Theory

Equations (2.21a)-(2.21b) and Eqs. (2.23a)-(2.23b), which describe the motion of 2- and 3-craft Coulomb formations, may both be written as 1st order ODE systems, in the form of Eq. (2.26). Here τ is the independent variable of integration, and \mathbf{u} is a vector of scaled charge control variables.

$$\mathbf{X}' = \mathbf{F}(\mathbf{X}, \mathbf{u}, \tau) \quad (2.26)$$

The state vector \mathbf{X} consists of the craft positions \mathbf{r}_i and scaled velocities \mathbf{v}_i , required to define all craft trajectories, and its derivative taken with respect to the rotating Hill frame is denoted $\mathbf{F} = \mathbf{X}'(\tau)$. Closed solution curves that satisfy Eq. (2.26), are denoted by a reference state vector trajectory $\mathbf{X}^*(\tau)$, and a reference feed-forward control vector $\mathbf{u}^*(\tau)$. The following two closed solution curve categories are considered in this dissertation.

1. **Equilibrium points** of Eq. (2.26):

Constant \mathbf{X}^* and \mathbf{u}^* such that $\mathbf{F}(\mathbf{X}^*, \mathbf{u}^*, \tau) = 0$ for all τ .

2. **Periodic orbits or cycles** of Eq. (2.26):

Variable $\mathbf{X}^*(\tau)$ and $\mathbf{u}^*(\tau)$ such that $\mathbf{X}^*(\tau + \tau_p) = \mathbf{X}^*(\tau)$, where the minimum τ_p for $\mathbf{X}^*(\tau)$ to repeat is called the orbit period.⁵⁴ The vector $\mathbf{u}^*(\tau)$ is also cyclic, but may have shorter repeat period than τ_p .

The terminology “static Coulomb formation” is used to refer to an equilibrium point solution, whereas “periodic Coulomb formation” refers to a periodic solution. Constant charge static Coulomb formations yield ‘virtual structures’, in which craft separation distances and the formation geometry appears frozen, with respect to the rotating frame. The periodic Coulomb formations, on the other hand, represent all closed solution curves of Eq. (2.26), which are not equilibrium points.⁵⁴ These do not necessarily provide constant geometry nor separation distances, but rather yield relative motion orbits of all craft about the CM.

2.6.1 Linearized State Space Systems

The zero-input response of the Eq. (2.26) system, in the vicinity of a reference trajectory, is approximated by Eq. (2.27). A linear ODE system in which the state propagation matrix $\mathbf{A}(\tau)$ governs the dynamics of small state perturbations $\delta\mathbf{X}(\tau)$, from $\mathbf{X}^*(\tau)$.⁵⁵

$$\delta\mathbf{X}'(\tau) = \left(\frac{\partial \mathbf{F}}{\partial \mathbf{X}} \right) \Big|_{(\mathbf{X}^*, \mathbf{u}^*)} \delta\mathbf{X}(\tau) = \mathbf{A}(\tau) \delta\mathbf{X}(\tau) \quad (2.27)$$

The linearization about an equilibrium point makes Eq. (2.27) an autonomous system, but a periodic orbit solution necessitates a non autonomous linear system, with an $\mathbf{A}(\tau)$ that is τ_p periodic.^{48,54} Moreover, there exists a state transition matrix $\Phi(\tau, 0)$, that maps $\delta\mathbf{X}$ from $0 \rightarrow \tau$, in accordance with Eq. (2.28), and where for simplicity

the initial τ has been set to zero. The state transition matrix (STM) satisfies the same ODE as $\delta\mathbf{X}$, and thereby has the same state propagation matrix.⁵⁶

$$\delta\mathbf{X}(\tau) = \Phi(\tau, 0) \delta\mathbf{X}(0) \quad \Phi'(\tau, 0) = \mathbf{A}(\tau) \Phi(\tau, 0) \quad (2.28)$$

The controlled evolution of $\delta\mathbf{X}$ is defined by Eqs. (2.29a)-(2.29b), where $\delta\mathbf{u}$ denotes variations from \mathbf{u}^* .

$$\delta\mathbf{X}'(\tau) = \mathbf{A}(\tau) \delta\mathbf{X}(\tau) + \mathbf{B}(\tau) \delta\mathbf{u}(\tau) \quad (2.29a)$$

$$\mathbf{B}(\tau) = \left(\frac{\partial \mathbf{F}}{\partial \mathbf{u}} \right) \Big|_{(\mathbf{x}^*, \mathbf{u}^*)} \quad (2.29b)$$

This state space representation assumes a zero feed-forward matrix and full state observability (with negligible measurement error), such that output and state vectors are considered interchangeable.

2.6.1.1 Two-Craft Zero-Input Linearized Dynamics

Two-craft Coulomb formations governed by the Eq. (2.21a) dynamics, have an $\mathbf{A}(\tau)$ matrix derived in Eqs. (2.30a)-(2.30b). Where $\tilde{Q}(\tau) = \tilde{Q}_{12}^*(\tau)$ is used to denote a reference feed-forward charge product history, and $\mathbf{0}$ and \mathbf{I} denote 3×3 zero and identity matrices, respectively.

$$\mathbf{A}(\tau) = \left[\begin{array}{c|c} \mathbf{0} & \mathbf{I} \\ \hline \frac{\partial \mathbf{r}''}{\partial \mathbf{r}} & \frac{\partial \mathbf{r}''}{\partial \mathbf{v}} \end{array} \right] \Big|_{(\mathbf{x}^*, \mathbf{u}^*)} = \left[\begin{array}{c|c} \mathbf{0} & \mathbf{I} \\ \hline \mathbf{H} & \mathbf{G} \end{array} \right] \quad \mathbf{G} = \begin{bmatrix} 0 & 2 & 0 \\ -2 & 0 & 0 \\ 0 & 0 & 0 \end{bmatrix} \quad (2.30a)$$

$$\mathbf{H}(\tau) = \begin{bmatrix} 3 & 0 & 0 \\ 0 & 0 & 0 \\ 0 & 0 & -1 \end{bmatrix} + \tilde{Q}(\tau) \Psi(r) \left[\left(\mathbf{I} - \frac{3\mathbf{r}\mathbf{r}^T}{r^2} \right) - \frac{\mathbf{r}\mathbf{r}^T}{M_{r1}\lambda_d(r + M_{r1}\lambda_d)} \right] \quad (2.30b)$$

Where $\Psi(r)$ is as defined in Eq. (2.21b), and $\mathbf{r} = \mathbf{r}_1^*$ denotes a craft 1 reference position vector (possibly τ dependent), given component wise by Eq. (2.31).

$$\mathbf{r}(\tau) = \mathbf{r}_1^*(\tau) = \begin{bmatrix} x_1^* \\ y_1^* \\ z_1^* \end{bmatrix} = \begin{bmatrix} x \\ y \\ z \end{bmatrix} \quad (2.31)$$

The $\mathbf{A}(\tau)$ matrix has the same form as associated with periodic orbits about libration points in the CRTBP.⁴⁹ And consequently, Φ is a similarly symplectic matrix according to Eq. (2.32), where \mathbf{J} is the defined skew-symmetric matrix.

$$\mathbf{J}\mathbf{A}^T = -\mathbf{A}\mathbf{J} \quad \Phi\mathbf{J}\Phi^T = \mathbf{J} \quad \mathbf{J} = \left[\begin{array}{c|c} \mathbf{0} & \mathbf{I} \\ \hline -\mathbf{I} & \mathbf{G} \end{array} \right] \quad (2.32)$$

Hence for 2-craft Coulomb formations, small motions about $\mathbf{X}^*(\tau)$ have this analytical property (and the consequences for stability it entails) in common with libration points in the CRTBP.⁴⁹

2.6.1.2 Three-Craft Zero-Input Linearized Dynamics

To concisely write the linearized dynamics, the Eq. (2.33) c_{ij} terms are introduced. These are products of $\Psi(d_{ij})$ and \tilde{Q}_{ij}^* , with Ψ as defined in Eq. (2.23c), and $d_{ij} = r_{ij}^*$ denoting reference separation distances.

$$c_{ij} = \tilde{Q}_{ij}^* \Psi(d_{ij}) = \frac{\tilde{Q}_{ij}^* (1 + d_{ij}/\lambda_d)}{d_{ij}^3 \exp[d_{ij}/\lambda_d]} 0.05in \quad (2.33)$$

A state perturbation vector $\delta\mathbf{X}(\tau)$ for three-craft Coulomb formations is defined in Eq. (2.34a), along with the state propagation matrix $\mathbf{A}(\tau)$ written in block format. All sub-matrices are 6×6 , with \mathbf{G} and \mathbf{H} given by Eq. (2.34b).

$$\delta \mathbf{X} = \begin{bmatrix} \delta \mathbf{r}_1 & \delta \mathbf{r}_3 & \delta \mathbf{v}_1 & \delta \mathbf{v}_3 \end{bmatrix}^T \quad \mathbf{A} = \left[\begin{array}{c|c} \mathbf{0} & \mathbf{I} \\ \mathbf{H} & \mathbf{G} \end{array} \right] \quad (2.34a)$$

$$\mathbf{G} = \begin{bmatrix} 0 & 2 & 0 & 0 & 0 & 0 \\ -2 & 0 & 0 & 0 & 0 & 0 \\ 0 & 0 & 0 & 0 & 0 & 0 \\ 0 & 0 & 0 & 0 & 2 & 0 \\ 0 & 0 & 0 & -2 & 0 & 0 \\ 0 & 0 & 0 & 0 & 0 & 0 \end{bmatrix} \quad \mathbf{H} = \left[\begin{array}{c|c} \frac{\partial \mathbf{r}_1''}{\partial \mathbf{r}_1} & \frac{\partial \mathbf{r}_1''}{\partial \mathbf{r}_3} \\ \frac{\partial \mathbf{r}_3''}{\partial \mathbf{r}_1} & \frac{\partial \mathbf{r}_3''}{\partial \mathbf{r}_3} \end{array} \right] \Bigg|_{(\mathbf{X}^*, \mathbf{u}^*)} \quad (2.34b)$$

Utilizing the new c_{ij} notation, the partial derivative terms that form \mathbf{H} are derived in Eqs. (2.35a)-(2.35d).

$$\mathbf{h}_{11} = \begin{bmatrix} 3 & 0 & 0 \\ 0 & 0 & 0 \\ 0 & 0 & -1 \end{bmatrix} \quad \mathbf{h}_{12} = \left[\left(\mathbf{I}_{3 \times 3} - \frac{\mathbf{r}_{12} \mathbf{r}_{12}^T}{r_{12}^2} \right) - \frac{\mathbf{r}_{12} \mathbf{r}_{12}^T}{\lambda_d^2 + r_{12} \lambda_d} \right] \quad (2.35a)$$

$$\mathbf{h}_{13} = \left[\left(\mathbf{I}_{3 \times 3} - \frac{\mathbf{r}_{13} \mathbf{r}_{13}^T}{r_{13}^2} \right) - \frac{\mathbf{r}_{13} \mathbf{r}_{13}^T}{\lambda_d^2 + r_{13} \lambda_d} \right] \quad \mathbf{h}_{23} = \left[\left(\mathbf{I}_{3 \times 3} - \frac{\mathbf{r}_{23} \mathbf{r}_{23}^T}{r_{23}^2} \right) - \frac{\mathbf{r}_{23} \mathbf{r}_{23}^T}{\lambda_d^2 + r_{23} \lambda_d} \right] \quad (2.35b)$$

$$\frac{\partial \mathbf{r}_1''}{\partial \mathbf{r}_1} = \mathbf{h}_{11} + \left(\frac{M_{r1}}{m_1} \right) c_{12} \mathbf{h}_{12} + \left(\frac{1}{m_1} \right) c_{13} \mathbf{h}_{13} \quad \frac{\partial \mathbf{r}_1''}{\partial \mathbf{r}_3} = - \left(\frac{m_3}{m_1 m_2} \right) c_{12} \mathbf{h}_{12} - \left(\frac{1}{m_1} \right) c_{13} \mathbf{h}_{13} \quad (2.35c)$$

$$\frac{\partial \mathbf{r}_3''}{\partial \mathbf{r}_3} = \mathbf{h}_{11} - \left(\frac{M_{r3}}{m_3} \right) c_{23} \mathbf{h}_{23} - \left(\frac{1}{m_3} \right) c_{13} \mathbf{h}_{13} \quad \frac{\partial \mathbf{r}_3''}{\partial \mathbf{r}_1} = \left(\frac{m_1}{m_2 m_3} \right) c_{23} \mathbf{h}_{23} - \left(\frac{1}{m_3} \right) c_{13} \mathbf{h}_{13} \quad (2.35d)$$

Where each of the \mathbf{r}_{ij} are evaluated at equilibrium, when substituted into \mathbf{H} .

2.6.2 Eigenspaces and Invariant Manifolds of Equilibria

The general state space system of Eq. (2.27), linearized about an equilibrium point \mathbf{X}^* , results in an autonomous matrix \mathbf{A} . This can then be transformed to Jordan canonical form and decomposed into unstable, stable, and center eigenspaces (E^u , E^s , E^c with dimensions N_u , N_s , and N_c , respectively), where perturbations along the E^u basis vectors will grow, and those along E^s will dissipate.⁵⁵ Moreover, $N_u > 0$ indicates an unstable zero-input linear system, and also that the complete

nonlinear system is unstable.⁵⁷ Global stable and unstable manifolds (if they exist) are defined as subspaces containing all trajectories (the flow), which are solutions to the complete Eq. (2.26) nonlinear dynamics, and have the following properties.⁵⁵

1. Unstable manifold (W^u) is the set of all trajectories which approach \mathbf{X}^* exponentially as $\tau \rightarrow -\infty$, for $\tau < 0$.
2. Stable manifold (W^s) is the set of all trajectories which approach \mathbf{X}^* exponentially as $\tau \rightarrow \infty$, for $\tau > 0$.
3. The manifolds are invariant, meaning a trajectory starting in W^u or W^s remains in that subspace for all time.
4. W^u is tangent to $\pm E^u$ (W^s is tangent to $\pm E^s$) at \mathbf{X}^* , with $+E^u$ ($+E^s$) yielding a half manifold of W^u (W^s), and $-E^u$ ($-E^s$) the other half.
5. The manifold subspaces have dimensionality one greater than their corresponding eigenspaces (i.e. W^u has dimension $N_u + 1$).

The manifolds are approximated numerically by initiating small maneuvers $\Delta \mathbf{v}^{u/s} = \pm \epsilon E_{\mathbf{v}}^{u/s}$. Where, $E_{\mathbf{v}}^{u/s}$ indicates velocity components of the normalized eigenvectors which span either E^u or E^s , and ϵ is a small number. An unstable manifold trajectory $\mathbf{X}^u(\tau) \subset W^u$ starting from a perturbed state $\mathbf{X}^u = \mathbf{X}^* \pm \epsilon E_{\mathbf{v}}^u$, is propagated forward in time using $\mathbf{F}(\mathbf{X}^u, \mathbf{u}^*, \tau)$, for $\tau = 0 \rightarrow \tau_{\max}^u$. Whereas, a stable manifold trajectory $\mathbf{X}^s(\tau) \subset W^s$ with initial condition $\mathbf{X}^s = \mathbf{X}^* \pm \epsilon E_{\mathbf{v}}^s$, is propagated backward in time for $\tau = 0 \rightarrow -\tau_{\max}^s$.

One aspect of invariant manifold theory, of interest to Coulomb formation flying, is the potential existence of intersecting unstable and stable manifolds. Such

theoretical solutions ‘hop’ between unstable and stable branches (with little or no control effort), enabling spacecraft to disperse and return to equilibrium naturally, or enable a system to transfer (reconfigure) between different equilibrium. In the language of dynamical systems theory, such intersections are referred to as homoclinic and heteroclinic orbits.⁵⁴ These are defined as follows.

- **Homoclinic orbit:**

A solution curve Γ , such that $\Gamma \subset W^u(\mathbf{X}^*) \cap W^s(\mathbf{X}^*)$.

- **Heteroclinic orbit:**

A solution curve Γ , such that $\Gamma \subset W^u(\mathbf{X}_1^*) \cap W^s(\mathbf{X}_2^*)$, $\mathbf{X}_1^* \neq \mathbf{X}_2^*$.

Therefore a heteroclinic orbit represents a, zero cost, natural flow resulting in a re-configuration of the system, from one equilibrium to another. In reality it is near-heteroclinic trajectories which are sought. These only partially achieve the transfer, but can be differentially corrected with very little cost.

2.7 The Nonlinear Parameter Optimization Problem

Constrained parameter optimization and optimal control problems, both derived from the nonlinear Eq. (2.26) ODE model, are considered in Section 5.2.2 and Section 4.5, respectively. The parameter problem consists of algebraic constraints resulting from setting $\mathbf{X}' = 0$, and time independent \mathbf{X}^* and \mathbf{u}^* parameters being sought to minimize a cost function, or performance index J . This type of problem is defined generally in Eq. (2.36), and the numerical solution procedure for Eq. (2.36) is known as nonlinear programming (NLP).⁵⁸

$$\begin{aligned}
& \text{minimize} && J(\mathbf{X}_p) \\
& \text{subject to} && \mathbf{C}(\mathbf{X}_p) = 0 \quad \mathbf{D}(\mathbf{X}_p) \leq 0
\end{aligned} \tag{2.36}$$

Here the parameter vector \mathbf{X}_p consists of all independent decision variables, and the constraint vectors \mathbf{C} and \mathbf{D} may or may not be present, and also may be nonlinear. An optimal control problem can be approximated as a parameter optimization problem, in the form of Eq. (2.36), by requiring the control history $\mathbf{u}(\tau)$ to be defined using a finite set of time independent \mathbf{X}_p variables. This conversion technique, to solve as a NLP, is known as the direct method.⁵⁸ The specific conversion used in Section 4.5 is direct shooting, where the trajectory is segmented, and parameterized controls (and segment start times) are guessed. The Eq. (2.26) state vector differential equation is then integrated explicitly to evaluate the cost and constraints.⁵⁹

There exist many NLP algorithms, with two solution method categories being deterministic and stochastic. Deterministic or gradient methods generally require derivatives of J , \mathbf{C} , and \mathbf{D} with respect to \mathbf{X}_p , and an initial guess (IG) for \mathbf{X}_p within some unknown convergence tolerance.⁶⁰ Stochastic methods generally require neither, but rather are zeroth order methods relying on heuristics to update \mathbf{X}_p . Drawbacks to this class of method include difficulty handling constraints, non intuitive tuning of heuristics, and an increase in computational complexity (relative to gradient).³⁹

2.7.1 Stochastic Method: Particle Swarm Optimization

Particle Swarm Optimization (PSO) is selected for use in this study, in part because it is very simple to implement compared with other stochastic methods, and it has found use in optimal spacecraft trajectory problems.³⁹ Moreover, PSO is often able to avoid local minima (unlike gradient methods), but specified bounds on the

elements of \mathbf{X}_p are required. The adopted PSO implementation, closely follows that of Pontani and Conway,³⁹ and its pseudo code proceeds as follows.

1. Generate an initial random population

N_{pop} individuals are created, each with a corresponding parameter vector \mathbf{X}_p and an update (direction) vector $\Delta\mathbf{X}_p$. Components of each \mathbf{X}_p and $\Delta\mathbf{X}_p$ are uniformly and randomly generated within specified upper and lower bounds.

2. Begin iteration

3. An augmented cost \bar{J} is computed for each individual

The cost function J is augmented with a penalty function to account for the equality constraints \mathbf{C} , in accordance with Eq. (2.37), where $\boldsymbol{\alpha}$ is a user supplied vector of constraint weights.

$$\bar{J} = J + \sum_k \alpha_k |\mathbf{C}_k| \quad (2.37)$$

In contrast, inequality constraints are handled according to Eq. (2.38), where a very large cost \bar{J} is assigned to an individual if any element of \mathbf{D} is violated. This approach effectively enforces feasibility in the population.

$$\exists k : \mathbf{D}_k(\mathbf{X}_p) \longrightarrow \bar{J} = \infty, \Delta\mathbf{X}_p = \mathbf{0} \quad (2.38)$$

4. Save the individual and overall optimizers

Each individual's optimizer (\mathbf{X}_p yielding the lowest \bar{J}) over all iterations is saved and denoted \mathbf{Z}_p . The overall populations optimizer, over all iterations, is also saved and denoted \mathbf{Z}_{min} . This corresponds to the minimum augmented cost ever reached by any individual, denoted \bar{J}_{min} .

5. Update \mathbf{X}_p and $\Delta\mathbf{X}_p$ and enforce bounds

Each individual's direction and parameter vectors are updated according to Eqs. (2.39a)-(2.39c).

$$\Delta\mathbf{X}_p = \beta_I \Delta\mathbf{X}_p + \beta_C (\mathbf{Z}_p - \mathbf{X}_p) + \beta_S (\mathbf{Z}_{\min} - \mathbf{X}_p) \quad (2.39a)$$

$$\beta_I = \frac{1 + \rho_1}{2} \quad \beta_C = 1.49445 \rho_2 \quad \beta_S = 1.49445 \rho_3 \quad (2.39b)$$

$$\mathbf{X}_p = \mathbf{X}_p + \Delta\mathbf{X}_p \quad (2.39c)$$

The ρ_i terms are independent uniform random numbers, generated at each iteration, in the interval $(0, 1)$, and β_I , β_C , and β_S represent inertial, cognitive, and social heuristics, respectively. The Eq. (2.39b) heuristics, also employed by Pontani and Conway, were developed and optimized for various problems during early PSO performance research.³⁹ After the update, any component of $\Delta\mathbf{X}_p$ outside a limit is set to be on boundary. Furthermore, any component of \mathbf{X}_p found to be violating a bound is also set to be on boundary, and its corresponding $\Delta\mathbf{X}_p$ component is set to zero.

Iteration ends and convergence is said to occur when some stopping criteria is reached. Pontani and Conway use a maximum iteration count,³⁹ but an alternative criteria is presented and applied in Section 4.5.1.

2.7.2 Gradient Based Method

A gradient based sequential quadratic programming method (SQP), which handles constraints using the active set approach, is adopted in Section 4.5. In contrast to PSO, this method provides quadratic convergence and descent properties,

such that achieving an optima is guaranteed for certain functions.⁶⁰ First order gradients of J , \mathbf{C} , and \mathbf{D} are required and derived analytically in Section 4.5.2, for the particular problem of interest. This method’s convergence is highly dependent on both the quality of the IG and these derivatives, the latter of which depend on numerically propagated STM matrices, which can carry substantial numerical integration error. Nevertheless, descent towards a feasible local minima can be readily ascertained (unlike PSO), although consistent convergence can require substantial effort in practical aspects of scaling, integrator error reduction, and step size limits. The specific SQP algorithm used is called *VF13*, and it is part of a commercially developed software library in the *FORTRAN* language.⁶¹

2.8 Numerical Simulation Constants

All numerical results presented in Chapters 3-6, unless specifically noted otherwise, are generated using the Table 2.1 constant values. All craft are assumed to

Table 2.1: Numerical Simulation Constant Parameters

Parameter	Value	Units
R_{cm}	$4.227e^7$	m
R_{sc}	1	m
λ_d	180	m
m_i	150	kg
ω	$7.2593e^{-5}$	rad/s
k_c	$8.99e^9$	Nm^2 / C^2

be of equal mass and radius, and a mean value for λ_d at GEO is adopted.²³ The physical spacecraft parameters and nominal CM orbit selected are reasonable (albeit somewhat arbitrary), and closely follow those of Natarajan and Schaub²² in their work targeting 2-craft Coulomb formation reconfigurations.

Chapter 3

Periodic Two-Craft Coulomb Formation Motions

3.1 Chapter Summary

In this chapter, relative motions of two-craft Coulomb formations are considered in the rotating Hill frame dynamical model, previously described. Specifically, relative motion periodic orbits are sought, which result from open-loop time varying potential functions $\mathbf{u}^*(\tau)$, and linearized gravity. The state vector along a cyclic trajectory is denoted $\mathbf{X}^*(\tau)$, and the state variables of both craft repeat at each τ_p time interval. These solutions, which occur without inertial thrust or feedback control, will be referred to as periodic (or dynamic) Coulomb formations.

Static Coulomb formation equilibria, in which constant potentials enable shapes that appear fixed with respect to their center of mass, are considered in Chapters 4-5, and are also derived and analyzed extensively in the literature.^{3,4,23,24,28-31,35,43} Various researchers, including Berryman and Schaub, state that future investigations should be directed towards the derivation of dynamic, and periodic Coulomb formations.^{17,32} The first examples of such periodic Coulomb formation solutions are presented here, and these serve as natural and desired extensions of the static equilibria. The solutions are defined for two vehicles, with time dependent charge histories that produce the assumed periodic craft trajectories. The periodic state functions cannot be assumed arbitrarily; however, because the set of admissible periodic flows is restricted by the underlying dynamics, including the Hill frame integral of motion

derived in Section 2.3.4.

Lyapunov stability of the periodic solutions is studied using Floquet theory,^{47,48} and linear asymptotic stability is demonstrated to be impossible using properties of the associated state transition matrices. Moreover, the degree of instability is assessed via the maximum modulus Floquet multiplier (Monodromy matrix eigenvalue), for the parameterized orbit families. The Monodromy matrix is shown to share many analytical properties with those corresponding to periodic orbits about libration points, in the CRTBP.⁴⁹ The numerical stability analyses of periodic Coulomb motions established here, should prove useful in the eventual design of controllers, to maintain and maneuver these open-loop orbits.

3.2 Properties of Periodic Coulomb Formations

The linear dynamics defined in Eqs. (2.27)-(2.28) and Eqs. (2.30a)-(2.30b), describe the motion about an arbitrary two-craft periodic solution, $\mathbf{X}^*(\tau)$ and $\mathbf{u}^*(\tau)$ with period τ_p . There exists an associated state transition matrix (STM), which propagated for τ_p is referred to as the full cycle Monodromy matrix. Floquet multipliers σ , correspond to the Monodromy matrix eigenvalues, and may be used to assess orbit stability. Specifically, the Eq. (2.27) linear system is unstable if any $|\sigma_i| > 1$ (and/or if any repeated $|\sigma_i| = 1$ is not semisimple).^{47,48} Stability here refers only to zero-input Lyapunov stability. That is, the response to initial state perturbations $\delta\mathbf{X}$, as opposed to structural stability involving perturbations to $\mathbf{u}^*(\tau)$, or errors in system parameters. Recall from Section 2.6.1.1, that the two-craft Coulomb formation STM satisfies the Eq.(2.32) symplectic property. A Monodromy matrix $\Phi(\tau_p, 0)$ for $\mathbf{X}^*(\tau)$ therefore has the following properties.⁴⁸

1. $\det(\Phi) = |\Phi| = 1$
2. At least one Floquet multiplier has modulus of unity: $|\sigma_i| = 1$
3. The σ_i appear in reciprocal pairs (i.e. if σ_i is eigenvalue, then so is $\sigma_j = 1/\sigma_i$)

These are the same properties as associated with periodic orbits about libration points in the CRTBP,⁴⁹ and the latter property entails that a stable σ_i (inside the unit circle) has a corresponding unstable σ_j (outside the unit circle). The maximum modulus Floquet multiplier, denoted $|\sigma|_{\max}$, is used as a measure for how strongly unstable a particular $\mathbf{X}^*(\tau)$ solution is. Based on Floquet theory,^{47,62} stability categories for the Eq. (2.27) linear system, about a 2-craft periodic solution, are summarized in Table 3.1. These categories imply that asymptotic stability is impossible for all 2-

Table 3.1: Floquet Stability of Periodic Coulomb Formations

Category	Lyapunov Stability
$ \sigma _{\max} = 1$	
All repeated $ \sigma_i = 1$ are semi-simple	Uniform Stable
Any repeated $ \sigma_i = 1$ is not semi-simple	Unstable
$ \sigma _{\max} > 1$	Unstable

craft periodic Coulomb formations, and at best such solutions will exhibit linearized uniform stability (boundedness). Furthermore, stability of $\mathbf{X}^*(\tau)$ in the Eq. (2.26) nonlinear system may be determined from the linearized system stability, via the *Principle of Stability in the First Approximation*.^{48,62}

Theorem 3.2.1. *If the linearized system $\mathbf{A}(\tau)$ matrix has all characteristic roots with negative real parts, or at least one root with positive real part, then $\mathbf{A}(\tau)$ is said to possess significant behavior. And if $\mathbf{A}(\tau)$ has significant behavior, the periodic orbit has identical stability in the nonlinear system as in the linearized system.*

The $|\sigma|_{\max} > 1$ is the only Table 3.1 category in which the linearized system possesses significant behavior. And by Theorem 3.2.1 the complete system is also unstable in that case. The other cases do not provide nonlinear stability information.

In addition, the 2-craft integral of motion h_z derived in Section 2.3.4 and defined by Eqs. (2.18a)-(2.18b) must also hold along $\mathbf{X}^*(\tau)$. Admissible periodic solutions must therefore satisfy Eq. (3.1), the derivative of h_z , taken with respect to the non dimensional time variable τ .

$$x(\tau)y''(\tau) - y(\tau)x''(\tau) = 0 \tag{3.1}$$

This effectively restricts what periodic orbits can occur, since it constrains the spacecraft 1 position vector, projected onto the reference orbit plane. Furthermore, coupling in the governing Eqs. (2.21a)-(2.21b) of motion, insist that a periodic solution has both x and y components, otherwise it has only a z component. Therefore, three possible periodic orbit types are permitted: \hat{e}_R - \hat{e}_T planar motions (in-plane), \hat{e}_N axis only (out-of-plane), and full state motions.

3.3 Periodic Coulomb Formations via Assumed Solutions

The reference spacecraft position components (x , y , and z) are assumed to take the form of simple harmonic oscillators. Therefore, the presented analyses are specific to these solutions, which happen to conserve total mechanical energy. Other periodic motions, having assumed functions described by different finite Fourier series, may exist, but are outside the scope of this work. However, the assumed periodic functions are not arbitrary, because the set of allowed motions is restricted, and some example candidate functions are shown in Section 3.3.4 to be inadmissible. Coulomb forces

are not generally conservative since active charge control, at the expense of power consumption, can provide arbitrary potential modulation. The open-loop potential functions considered here are explicitly dependent on spacecraft coordinates, and therefore nonconservative Coulomb forcing is also outside of the current scope.

3.3.1 In-Plane Periodic Motions

Dynamic Coulomb formations are derived here using the \hat{e}_R - \hat{e}_T components of the Eqs. (2.21a)-(2.21b) dynamics, since the \hat{e}_N component decouples to 1st order. It is assumed that $z(\tau) = 0$, and that $x(\tau)$ and $y(\tau)$ are simple harmonic oscillators (both with period τ_p), defined by Eq. (3.2), where A_x and A_y denote amplitudes of oscillation.

$$x(\tau) = A_x \cos(\theta\tau) \quad y(\tau) = A_y \sin(\theta\tau) \quad (3.2)$$

Therefore, oscillations occur about $x = y = 0$, with the initial condition $x(0) = A_x$, $y(0) = 0$. The oscillation frequency θ is related to the relative orbit period t_p (and non dimensional period τ_p) via Eq. (3.3).

$$\theta = \left(\frac{2\pi}{\tau_p} \right) = \left(\frac{2\pi}{\omega t_p} \right) \quad (3.3)$$

Time derivatives of x and y are also periodic and given explicitly by Eqs. (3.4a)-(3.4b).

$$x'(\tau) = -\theta A_x \sin(\theta\tau) \quad x''(\tau) = -\theta^2 x(\tau) \quad (3.4a)$$

$$y'(\tau) = \theta A_y \cos(\theta\tau) \quad y''(\tau) = -\theta^2 y(\tau) \quad (3.4b)$$

Equation (3.2) and Eqs. (3.4a)-(3.4b) are then substituted into Eq. (2.21a), and the resulting \hat{e}_R and \hat{e}_T acceleration terms are divided by $x(\tau)$ and $y(\tau)$, respectively. Rearranging such that the Coulomb acceleration terms are on the left hand side,

results in Eqs. (3.5a)-(3.5b), with $\Psi(r)$ as defined in Eq. (2.21b), and where $\tilde{Q} = \tilde{Q}_{12}^*$ and $r = r_1^*$ denote reference charge product and craft 1 distance, respectively.

$$\tilde{Q}(\tau) \Psi(r) = -\theta^2 - 3 - 2\theta \left(\frac{A_y}{A_x} \right) \quad (3.5a)$$

$$\tilde{Q}(\tau) \Psi(r) = -\theta^2 - 2\theta \left(\frac{A_x}{A_y} \right) \quad (3.5b)$$

Note that the right hand sides of Eqs. (3.5a)-(3.5b), must be equal, independent of $\tilde{Q}(\tau)$. Equating these leads to the quadratic equation.

$$\left(\frac{A_y}{A_x} \right) = \frac{-3 \pm \sqrt{9 + 16\theta^2}}{4\theta} \quad (3.6)$$

Equation (3.6) has two real solutions for all $\tau_p > 0$, since $\sqrt{9 + 16\theta^2}$ is always real. It also insists that $A_x \neq A_y$, meaning that the resulting relative motion orbit is an ellipse about the CM. Choosing the initial condition $A_x > 0$, the two roots of the quadratic lead to the following two solution cases.

- **Case A (The + root):** Ellipse semi-major axis is A_x , and semi-minor axis is A_y ($A_x > A_y$).
- **Case B (The - root):** Ellipse semi-major axis is $-A_y$, and semi-minor axis is A_x ($A_x < |A_y|$).

The necessary feed-forward charge history is derived from either Eq. (3.5a) or Eq. (3.5b), with the substitution of Eq. (3.6). This yields Eq. (3.7), with $\tilde{Q}(\tau)$ as an explicit function of $x(\tau)$ and $y(\tau)$, since $r^2(\tau) = x^2(\tau) + y^2(\tau)$.

$$\tilde{Q}(r(\tau)) = \frac{-1}{\Psi(r)} \left[\theta^2 + 3 + \left(\frac{-3 \pm \sqrt{9 + 16\theta^2}}{2} \right) \right] \quad (3.7)$$

The $\tilde{Q}(\tau)$ function produces the assumed periodic trajectory, and is itself a simple oscillator. However, its oscillations are offset from zero, and with period of $\tau_p/2$. Additionally, when $\tau_p = 2\pi$, t_p is equal to the CM orbital period (≈ 1 day), and the relative orbit has semi-major axis twice that of semi-minor axis. However for case B with $\tau_p = 2\pi$, a trivial solution of $\tilde{Q}(\tau) = 0$ results. The entire family of these periodic relative orbits, in the $\hat{e}_R\text{-}\hat{e}_T$ plane, can be generated as follows:

1. Choose A_x , and either Case A or Case B of Eq. (3.6)
2. Solve A_y via Eq. (3.6)
3. Propagate the open-loop system with $\tilde{Q}(\tau)$ defined by Eq. (3.7)

3.3.2 Orbit-Normal Periodic Motions

Oscillations along only the \hat{e}_N axis are considered here ($\hat{e}_R\text{-}\hat{e}_T$ dynamics ignored). The $z(\tau)$ motion of craft 1 is assumed to oscillate with amplitude A_z about a non zero offset z_0 , as defined by Eq. (3.8). It is also assumed that $r(\tau) = z(\tau)$, and that $z_0 > A_z$ to avoid collisions of the two vehicles.

$$z(\tau) = z_0 + A_z \sin(\theta\tau) \quad (3.8)$$

Unlike in-plane motions, the position magnitudes A_z and z_0 are unrestricted, with the exception that $z_0 > A_z$. The necessary charge history to enable this motion, derived similarly to what was done in Section 3.3.1, is given by Eq. (3.9).

$$\tilde{Q}(z(\tau)) = \frac{1}{\Psi(r)} \left[1 - \theta^2 + \theta^2 \frac{z_0}{z(\tau)} \right] \quad (3.9)$$

3.3.3 Full State Periodic Motions

If x , y , and z are all assumed to be, τ_p periodic, simple oscillators the only solution is a trivial non Coulomb solution: $\tilde{Q}(\tau) = 0$, $\theta = 1$, and $A_y/A_x = -2$. However, if $x(\tau)$ and $y(\tau)$ are defined as in Eq. (3.2), and $z(\tau)$ is defined as in Eq. (3.10), non trivial full state periodic motions are admitted.

$$z(\tau) = A_z \sin(B_z \theta \tau) \quad B_z = \dots \frac{1}{8}, \frac{1}{4}, \frac{1}{2}, 2, 4, 8 \dots \quad (3.10)$$

For fractional B_z , the relative orbits are τ_p/B_z periodic (with $1/B_z$ planar oscillations in a full cycle). Whereas for integer B_z , the relative orbits are τ_p periodic (with B_z orbit-normal oscillations in a cycle). Substituting the assumed solutions (and their derivatives) into Eqs. (2.21a)-(2.21b), and rearranging, leads to Eq. (3.11). This provides constraints on the assumed solution parameters, and Eq. (3.12) follows from Eq. (3.11), upon the substitution of Eq. (3.6) for the ratio A_x/A_y .

$$\tilde{Q}(\tau)\Psi(r) = (1 - B_z^2\theta^2) = -\theta^2 - 3 - 2\theta \left(\frac{A_y}{A_x} \right) \quad (3.11)$$

$$(1 - B_z^2\theta^2) = -\theta^2 - 2\theta \left(\frac{4\theta}{-3 \pm \sqrt{9 + 16\theta^2}} \right) \quad (3.12)$$

In these solutions, τ_p is no longer free, but rather is related to B_z via Eq. (3.12). Furthermore, Eq. (3.12) can be rewritten in the form of Eq. (3.13), a nonlinear root-finding function, in the variable θ . For integer B_z , there is a unique real-valued θ which satisfies Eq. (3.13), for both cases of Eq. (3.6). For fractional B_z , Eq. (3.13) admits no real-valued θ solutions.

$$8\theta^2 + \left(-3 \pm \sqrt{9 + 16\theta^2} \right) [\theta^2(1 - B_z^2) + 1] = 0 \quad (3.13)$$

In Figure 3.1(a), this function is plotted versus θ and integer B_z values, using the

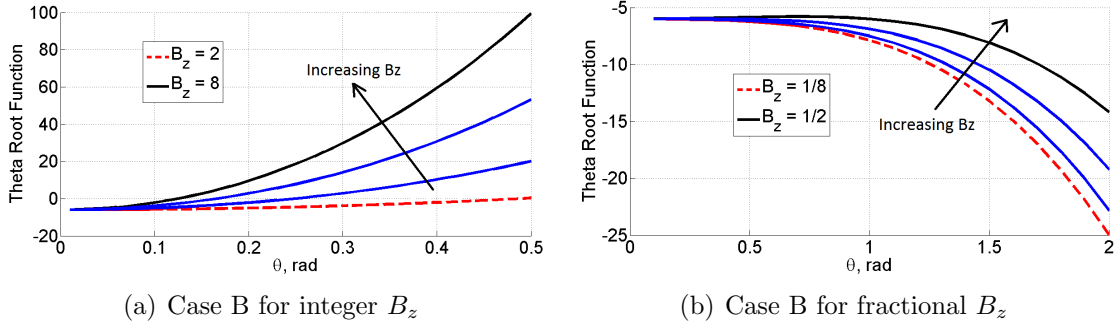


Figure 3.1: Full State Periodic Solutions: Eq. (3.13) vs. B_z and θ

case B (– root) of Eq. (3.6). Unique θ solutions are clearly illustrated, and this result is also valid for case A. In contrast, Figure 3.1(b) indicates real θ solutions do not exist for fractional B_z values, a result again also valid for case A. Therefore, full state periodic Coulomb formations with $z(\tau)$ of longer period than an in-plane cycle, are not permitted. Solutions are limited to the subset of even integer B_z , having \hat{e}_N axis oscillations that occur B_z times in τ_p . The amplitudes A_x and A_z are free, and so is B_z (in the subset of even integers). This leads to multiple families of three dimensional (in position), dynamic and periodic orbits. Orbits within the families can be generated as follows:

1. Choose A_x , A_z , and B_z (even integer)
2. Choose either Case A or Case B of Eq. (3.6)
3. Solve θ (and τ_p) numerically from Eq. (3.13)
4. With θ known, solve A_y via Eq. (3.6)
5. Propagate the open-loop system with $\tilde{Q}(\tau)$ defined by Eq. (3.7)

3.3.4 Inadmissible Periodic Trajectories

The Eq. (3.1) constant of motion means that $x(\tau)$ and $y(\tau)$ periodic functions cannot be assumed arbitrarily. The following are demonstrable examples of simple periodic functions, which cannot satisfy this constraint, and therefore such motions cannot occur.

- **Simple planar harmonic oscillators about the origin:**

$$x(\tau) = A_x \cos(\theta_x \tau) \quad y(\tau) = A_y \sin(\theta_y \tau) \quad (3.14)$$

Substituting into Eq. (3.1) yields $\theta_y^2 = \theta_x^2$, then since $\theta > 0$, we find that $\theta_x = \theta_y$. Therefore, Eq. (3.14) periodic flows having $\theta_x \neq \theta_y$ cannot exist. Hence $\theta_x = \theta_y = \theta$ is used in the previous examples.

- **General rotary motion (periodic polar curve):**

$$r(\tau) = A_x + A_y \sin(n\theta\tau) \quad (3.15a)$$

$$x(\tau) = r(\tau) \cos(n\theta\tau) \quad (3.15b)$$

$$y(\tau) = r(\tau) \sin(n\theta\tau) \quad (3.15c)$$

Where n is a positive integer and $A_y \neq 0$. Subbing Eqs. (3.15a)-(3.15c) into Eq. (3.1), yields Eq. (3.16).

$$2nA_y \cos(n\theta\tau) [A_y \sin(n\theta\tau) + A_x] = 0 \quad (3.16)$$

Equation (3.16) is not true for all τ , and by contradiction, the motion is invalid.

- **Simple planar harmonic oscillators, offset from origin:**

$$x(\tau) = x_0 + A_x \cos(\theta_x \tau) \quad (3.17a)$$

$$y(\tau) = y_0 + A_y \sin(\theta_y \tau) \quad (3.17b)$$

If x_0 or y_0 are zero, then Eq. (3.1) insists that $y(\tau)$ or $x(\tau)$ of Eqs. (3.17a)-(3.17b) are constant, both of which are contradictions. For $x_0 \neq 0$, $y_0 \neq 0$, and $\theta_x = \theta_y$ the Eq. (3.1) momenta condition is satisfied. However, it can be readily shown from the governing dynamics, that no real $\tilde{Q}(\tau)$ history can enable the motion. This demonstrates that Eq. (3.1) is a necessary (but not sufficient) condition for Coulomb formation periodic orbits, since an assumed trajectory can satisfy Eq. (3.1), but not be a real solution to Eqs. (2.21a)-(2.21b).

3.4 Numerically Simulated Periodic Coulomb Formations

The following results are generated by propagating Eqs. (2.21a)-(2.21b) numerically using the Table 2.1 parameter values.

3.4.1 In-Plane Periodic Motions

Example craft 1 position histories for $A_x = 20$ m and $\tau_p = \pi$ are presented in Figures 3.2(a)-3.2(b), along with corresponding potential histories in Figures 3.3(a)-3.3(b). These contrast $r(\tau)$ and $\phi_1(\tau)$ histories, associated with cases A and B.* Note that the ϕ_1 amplitude of oscillation is greater in case A, despite the case B example representing a larger area ellipse. For either case, the ϕ_1 amplitude increases in proportion to A_x , and inversely with τ_p .

3.4.2 In-Plane Periodic Motion Stability

Perturbations normal to the orbit plane decouple from the in-plane dynamics (to 1st order), and the two Floquet multipliers associated with orbit-normal perturba-

*In Figures 3.3(a)-3.3(b) and subsequent figures, S/C is used as a shorthand for spacecraft.

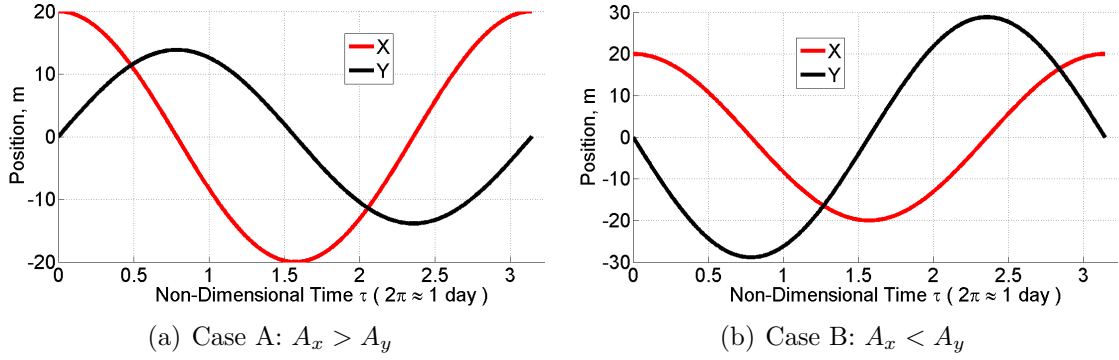


Figure 3.2: Planar Periodic Solution Position Histories: $A_x = 20$ m, and $\tau_p = \pi$

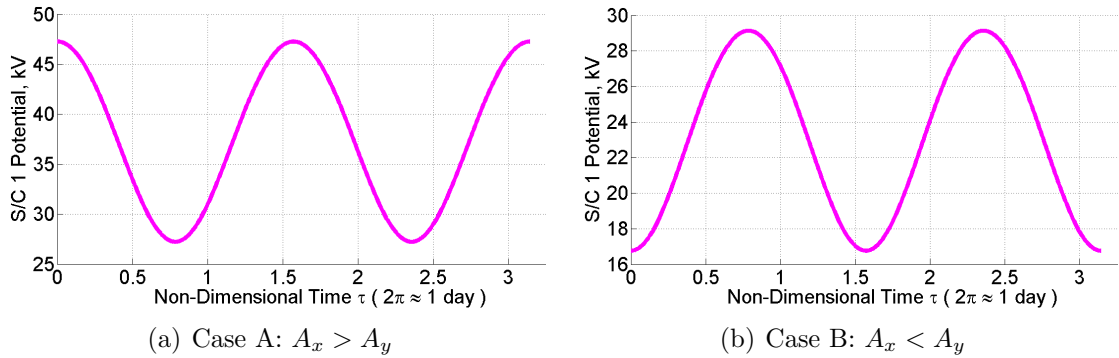


Figure 3.3: Planar Periodic Solution Potential Histories: $A_x = 20$ m, and $\tau_p = \pi$

tions, have modulus of unity. Values of the remaining four multipliers, or Monodromy matrix eigenvalues, are functions of A_x , τ_p , and case A/B selection. Numerical trends in the magnitude of $|\sigma|_{\max}$, and the real or complex nature of the eigenvalues, are summarized as follows.

1. $|\sigma|_{\max} \uparrow$ as $\tau_p \uparrow$ and as $A_x \uparrow$ (weakly for Case A)
2. Case A planar σ_i have 1 purely real pair and 1 complex pair for $\tau_p < 2\pi$ (2 purely real pairs otherwise)
3. Case B planar σ_i have 2 complex pairs for $\tau_p < 2\pi$ (1 purely real pair and 1 complex pair otherwise)

In both cases, $|\sigma|_{\max} \approx 1$ for $\tau_p \ll 2\pi$, and therefore quickly oscillating formations are weakly unstable. In Figures 3.4-3.5, Monodromy matrix eigenvalues associated with a case B formation are shown in the complex plane, for varying A_x and τ_p .

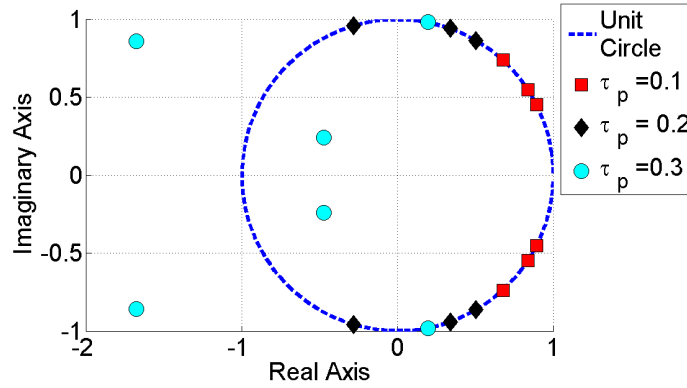


Figure 3.4: Floquet Multipliers in Complex Plane versus τ_p , for $A_x = 25$ m

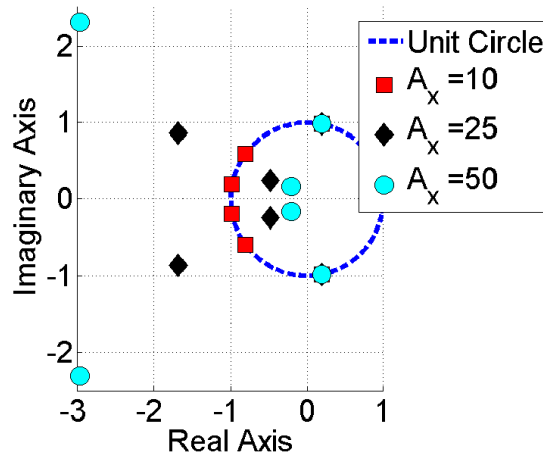


Figure 3.5: Floquet Multipliers in Complex Plane versus A_x , for $\tau_p = 0.3$

The parameter dependent stability is clear, and it is evident that two of the σ_i (those associated with \hat{e}_N modes) remain on the unit circle, and move around it with τ_p . It can be inferred from the plots that case B formations, with $\tau_p < 1$ hr and separation distance on the order of 10 meters, exhibit very near marginal stability.

3.4.3 Orbit-Normal Periodic Motions

An example orbit-normal oscillatory solution is shown in Figures 3.6(a)-3.6(b), propagated for two periods, with $z_0 = 15$ m, $A_z = 5$ m, and $\tau_p = \pi$. Unlike in the planar solutions, $\phi_1(\tau)$ is not a simple harmonic oscillator. At the maximum separa-

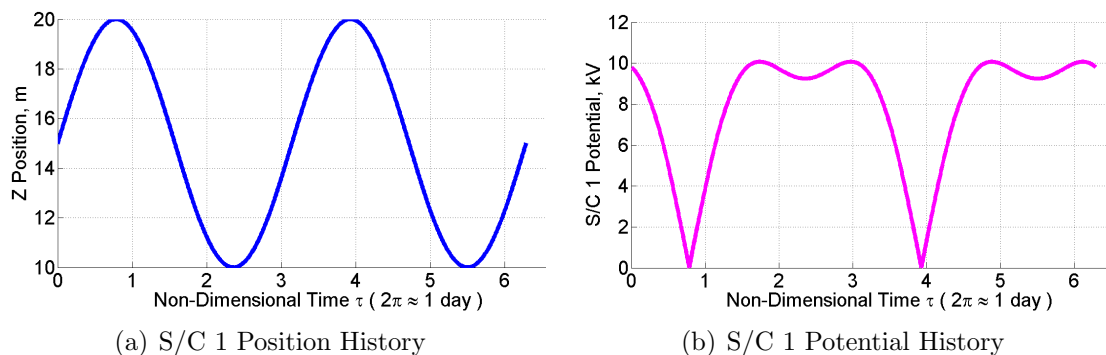


Figure 3.6: Orbit-Normal Periodic Solution: $z_0 = 15$ m, $A_z = 5$ m, and $\tau_p = \pi$

tion distance (40 m) the potential approaches zero, and at the minimum separation distance there is a dip in the potential. This dip is due to the increased Coulomb interaction there, and as the ratio z_0/A_z increases this dip becomes more smooth.

3.4.4 Orbit-Normal Periodic Motion Stability

Perturbations along the \hat{e}_N axis are marginally stable, but perturbations in the reference orbit plane, exhibit unstable and stable modes. The maximum modulus Floquet multiplier, is a function of z_0 , τ_p , and the ratio A_z/z_0 (ratio is between 0 and 1). Some numerical trends are summarized as follows.

1. $|\sigma|_{\max} \uparrow$ as $A_z/z_0 \uparrow$ (and weakly as $z_0 \uparrow$)
2. $|\sigma|_{\max} \uparrow$ as $\tau_p \uparrow$ (for $0 < \tau_p < 1$ hr)
3. $|\sigma|_{\max} \downarrow$ as $\tau_p \uparrow$ (for $\tau_p \gg 1$ hr)

4. Depending on assumed solution parameters, σ_i may be all complex, all real, or a combination of both.

It is found that $|\sigma|_{\max} \leq 1.0007$, for t_p small (order of minutes) and $A_z/z_0 < 0.1$. Meaning that very fast, small amplitude, oscillatory motions along the \hat{e}_N axis are weakly unstable.

3.4.5 Full State Periodic Motions

Figures 3.7(a)-3.7(b) illustrate example full state periodic Coulomb formations, for $A_x > A_y$ (case A), $A_x = 20$ m, $A_z = 10$ m, and $B_z = 2$. The required oscillation period (computed numerically) is around 0.73 days. Similar to the orbit-

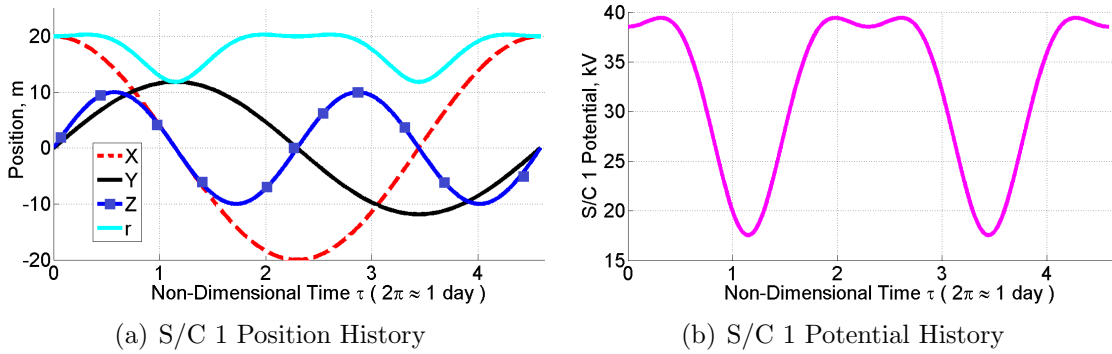


Figure 3.7: Full State Periodic Solution: $A_x = 20$ m, $A_z = 10$ m, and $B_z = 2$

normal solution (and unlike the in-plane solutions), $\phi_1(\tau)$ is not a simple harmonic oscillator. This trajectory (craft 1) is plotted in Figure 3.8(a), and the geometry resembles that of a saddle. Additionally, a different example trajectory is shown in Figure 3.8(a), demonstrating some of the rich geometry in these orbit families. This latter orbit is of the case B family, generated with the same A_x and A_z (as case A example), but with $B_z = 4$ and resulting in a longer period (≈ 4.4 days). Some

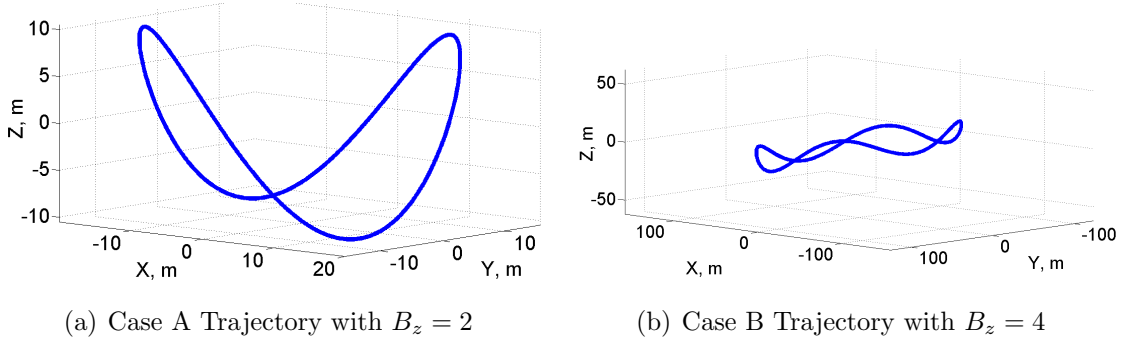


Figure 3.8: Full State Periodic Solution Trajectories: $A_x = 20$ m and $A_z = 10$ m

qualitative differences in case B orbits (relative to case A) include a longer τ_p for the same $|A_x \cdot A_y|$ magnitude, and simple harmonic oscillation for $\phi_1(\tau)$.

3.4.6 Full State Periodic Motion Stability

For these orbit families, $|\sigma|_{\max}$ is a function of all parameters: B_z , A_x , A_z , and case A/B selection. The following numerical trends (for both cases) are identified when varying, $2 \leq B_z \leq 8$, $10 \leq A_x \leq 100$ m, and $5 \leq A_z \leq 80$ m.

1. $|\sigma|_{\max} \uparrow$ as $B_z \uparrow$
2. $|\sigma|_{\max} \uparrow$ as $A_x \uparrow$ (although often weakly)

All are Lyapunov unstable, with the significant driver of relative instability being B_z , and the case A orbits tend to be more unstable, exhibiting $|\sigma|_{\max}$ of much larger magnitude than those associated with case B. The smallest value found for case A orbits is $|\sigma|_{\max} = 3511$, corresponding to $B_z = 2$, $A_x = 50$, and $A_z = 80$. Whereas the case B solutions rendered $1.8 \leq |\sigma|_{\max} \leq 1500$, with $|\sigma|_{\max} = 1.8$ occurring at $B_z = 2$, $A_x = 10$, and $A_z = 45$.

3.5 Chapter Conclusions

The existence of dynamic and periodic Coulomb formations are demonstrated for two spacecraft in the Hill frame with differential gravity. These are the first demonstrated examples of repeating relative orbit motions, in which the charge is dynamically varied in open-loop to produce the forcing. Furthermore, the required variations are slow transitions of kilovolt order, and are therefore readily achievable charge changes at moderate power levels (order of Watts). The results provide a valuable extension to the many works concerning static Coulomb formations (fixed distances and constant potentials).

Some possible applications for these near propellantless relative orbits include interferometry with variable separation distance (and optionally an inertially fixed line-of-sight vector), Earth/Sun imaging, and autonomous inspection of a cooperating or non cooperating vehicle. Detailed examinations into utilizing these electrostatic forced periodic solutions, should be considered in future research. The open-loop orbits would, of course, require feedback stabilization. Hence, the varied relative instability demonstrated here would be crucial in selecting particular solutions, and in the development of station-keeping control.

This investigation restricts attention to 2-craft formations with approximate dynamics, and so future research should attempt to derive analogous oscillatory flows for 3-craft (or even N-craft) Coulomb formations, within this dynamical model or otherwise (e.g. higher order gravity or CRTBP). Quasi-periodic solutions should also be considered, and these could include numerically targeted solutions or simply those orbits which result from integrating exact periodic solutions using higher order perturbed dynamics. The examples presented here represent assumed solutions, rather

than an exhaustive presentation of all possible periodic motions. However, admissible assumed craft position functions are non arbitrary, and the full set of solutions will exist as a subset of some finite Fourier series representation. Future research should determine the existence of these hypothesized solutions, and the Hill frame integral of motion should facilitate such efforts. Lastly, the sensitivity of all motions to primary perturbations (and uncertain environmental conditions) is analyzed in Chapter 6. This is done to substantiate the stability results of this Chapter, and also to anticipate the challenges of executing these trajectories in higher fidelity.

Chapter 4

Optimal Two-Craft Reconfigurations along Manifolds

4.1 Chapter Summary

In this chapter, two-craft static Coulomb formations are considered, where a constant feed-forward control \mathbf{u}^* (the charge product \tilde{Q}_{12}^*) and a constant state vector \mathbf{X}^* define the equilibrium solution. These solutions, enabled without inertial thrust or feedback control, result in ‘virtual structures’ that appear fixed with respect to the rotating Hill frame. There exist three unique configuration solutions (aligned along each Hill axis), and the equilibrium conditions for these are well known and extensively studied.^{4,17,35} All three are dynamically unstable.

A stability analysis of these solutions was first undertaken by Natarajan and Schaub,^{22,35} with the purpose of developing continuous feedback controllers to maintain the formations. In this research, a stability decomposition is performed, motivated by the more efficient realization of formation shape changes. Also in contrast to Refs. 22, 35, this stability analysis applies dynamical systems theory techniques, as described in Section 2.6.2. The eigendecomposition for each configuration are examined in Section 4.3, and only two of the three solutions are found to admit unstable/stable manifolds. Moreover, there exist no parameter dependent bifurcations in any configuration.

In Section 4.4, invariant manifolds are numerically generated for the two con-

figurations that admit them, and their structures are scrutinized for the first time. Scenarios in which near-heteroclinic transfer orbits arise are identified. In Section 4.5, a methodology is outlined for targeting such manifold trajectories, and for formulating their differential correction as nonlinear programming problems. To do this, the manifold branches are divided into segments each having parameterized charge control and inertial thrusting introduced. Parameter values which match continuity, with minimum total inertial control effort, are then determined numerically. Example optimized reconfigurations are presented in Section 4.6. The resulting optimization problems are numerically difficult to solve, and two different methods (gradient and stochastic) are utilized as solvers, and their performance compared. The gradient based SQP method is found to provide more consistent convergence and with higher quality optima; however, solutions obtained do not always meet bounding criteria enforced on the PSO method.

Finally, some consideration is given to alternate problem formulations, and what effect this has on the resulting optima, as well as how the method might be extended in formulation, and to include transfers involving other static and/or periodic Coulomb formations. Nevertheless, in general, and even with relatively coarse control parameterization, the method is shown capable of delivering ΔV cost reduction versus a baseline measure.

4.2 Motivation

Coulomb formations theoretically impart two advantageous properties. First is the ability of the free-flying formations to change shape or reconfigure. And second is the near propellantless means for achieving, sustaining, and maneuvering the

spacecraft formations (albeit with limited system controllability). The research of this Chapter primarily aspires to marry these two favorable properties, by applying dynamical systems theory and optimization in targeting transfers between 2-craft static Coulomb formations. Also, very few works consider reconfiguring of Coulomb formations,^{23,24} and only one with formal optimization.²³ Therefore, efficiently maneuvering these interesting formations is a current technical void, in this novel research area.

Ideally the shape changes would be accomplished using only charge control, but in general limited Coulomb force controllability necessitates some inertial thrusting. Therefore, near-heteroclinic orbits are sought, representing partial reconfigurations where only constant charge control is active. Optimization is then applied to converge upon a continuous transfer trajectory, achieved using as little inertial thrust as possible, in exchange for added electrostatic control effort.

This is analogous to how manifold theory has successfully been used to design low-thrust transfers between regions of space, in multi-body gravity fields.⁴¹ The work here, therefore constitutes an extension of low-energy spacecraft trajectories to relative motion problems. Specifically for Coulomb formations, in which the highly nonlinear electrostatic force gives rise to chaotic dynamics, akin to what emerges from the third body perturbation in the CRTBP. More generally, it is expected that non intuitive trajectories and dynamical motions will become more tractable upon applying invariant manifold theory, which will prove useful in Coulomb formation design, control, and navigation.

4.3 Two-Craft Static Coulomb Formation Solutions

In addition to periodic solutions derived in Chapter 3, the two-craft dynamical model of Eqs. (2.21a)-(2.21b) admits three, and only three, static equilibrium solutions.^{4,17,24,35} The three configurations correspond to the vehicles being along each of the Hill axes. Radial and Orbit-Normal aligned cases are depicted in Figures 4.1-4.2, and the third (not shown) is denoted Along-Track (having the two craft along the \hat{e}_T axis). An attractive force is required for the Radial configuration, a repulsive force for

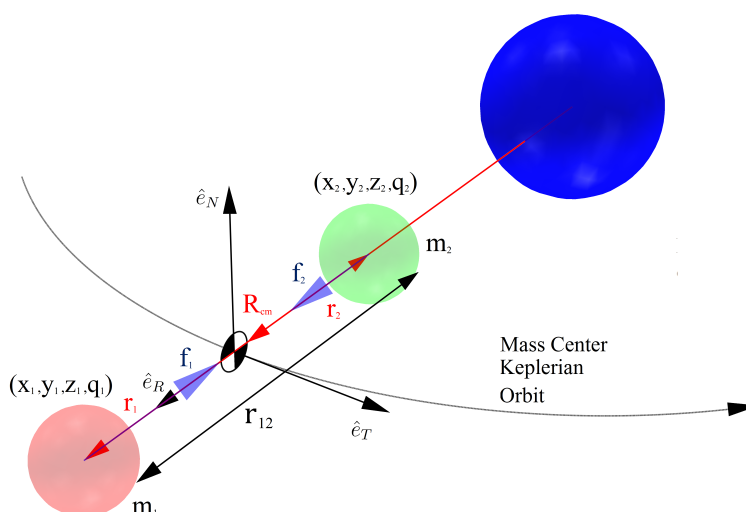


Figure 4.1: Radial Two-Craft Coulomb Formation Equilibrium

the Orbit-Normal configuration, and the Along-Track results in $\tilde{Q} = 0$ (a somewhat degenerate case since it does not involve electrostatic forces). Previously derived¹⁷ conditions for equilibrium, resulting from all derivatives in Eqs. (2.21a)-(2.21b) being set to zero, are summarized in Table 4.1. Where $\tilde{Q} = \tilde{Q}_{12}^*$ is the constant scaled charge product required to achieve equilibrium, at a reference craft 1 distance of $r = r_1^*$ (from the CM). Formation equations of relative motion are linearized about each of these equilibrium, per Section 2.6.1, resulting in linear ODE systems of the Eq. (2.27) form.

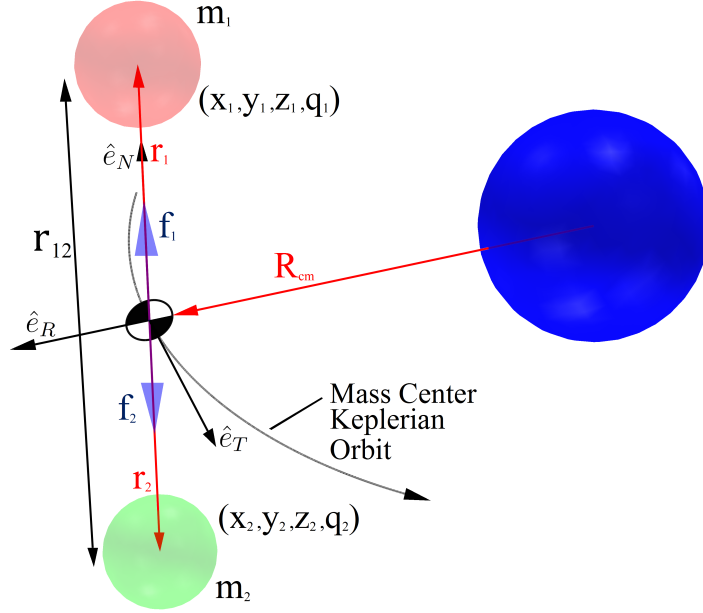


Figure 4.2: Orbit-Normal Two-Craft Coulomb Formation Equilibrium

Table 4.1: Two-Craft Coulomb Formation Equilibrium Conditions

Axis	Craft 1 Position, \mathbf{r}	Scaled Charge Product, \tilde{Q}
Radial	$x = x_1^* = M_{r1} r_{12}^*$ $y = z = 0$	$-3 \Psi(x)$
Orbit-Normal	$z = z_1^* = M_{r1} r_{12}^*$ $x = y = 0$	$\Psi(z)$
Along-Track	$y = y_1^* = M_{r1} r_{12}^*$ $x = z = 0$	0

Linear stability is governed by the eigenstructure of the corresponding autonomous \mathbf{A} matrices, described generally in Section 2.6.2. Important properties specific to these static equilibria cases, are summarized as follows.

1. All three equilibrium configurations are internally unstable, and the stability properties remain constant (i.e. no bifurcations occur over varied parameter

values: λ_d , m_1 , m_2 , and ω).

2. **Radial:** All eigenvalues are distinct. One unstable mode and one stable mode ($N_u = N_s = 1$), both purely real and contained in the \hat{e}_R - \hat{e}_T plane. The center subspace ($N_c = 4$) has one complex conjugate pair in the \hat{e}_R - \hat{e}_T plane, and the other along the \hat{e}_N axis.
3. **Orbit-Normal:** All eigenvalues are distinct. One unstable and one stable complex conjugate pair ($N_u = N_s = 2$), resulting in oscillatory modes. A center mode complex conjugate pair is along the \hat{e}_N axis ($N_c = 2$).
4. **Along-Track:** This system possesses critical behavior, since all eigenvalues have zero real part ($N_c = 6$). However, an eigenvalue at zero is repeated and not semi-simple, and therefore the linear system is Lyapunov unstable (although not generally true, this nonlinear system is in fact also unbounded).⁶³

The application of invariant manifold theory, stated generally in Section 2.6.2, to these two-craft static Coulomb formations is central to the new contributions of the current investigation. Global unstable and stable manifolds exist only for the Radial and Orbit-Normal configurations ($N_u > 0$ and $N_s > 0$), and these are generated using the procedure outlined in Section 2.6.2, with eigenspaces computed numerically from the Jacobian defined in Eqs. (2.30a)-(2.30b). Manifolds are propagated using Eqs. (2.21a)-(2.21b), with charges held at equilibrium values.

4.4 Radial and Orbit-Normal Case Invariant Manifolds

The following invariant manifold examples, and subsequent numerical results in Section 4.6, are generated with $\epsilon = 0.01$ mm/s, and assuming the two craft are of

equal mass and radius R_{sc} using the Table 2.1 values. Figures 4.3-4.4 (Radial) and Figures 4.5-4.6 (Orbit-Normal) depict stable and unstable manifolds of equilibria with $r_{12}^* = 25$ m, and propagated for integer values of the dimensional CM orbital period T_p . Although the system flow is dependent on λ_d , ω , m_1 , and m_2 , these manifolds

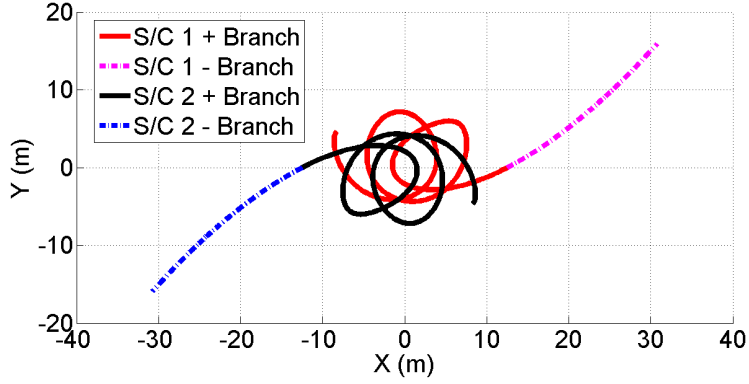


Figure 4.3: Radial S/C 1 and 2 Stable Manifolds W^s , Propagated $1 T_p$

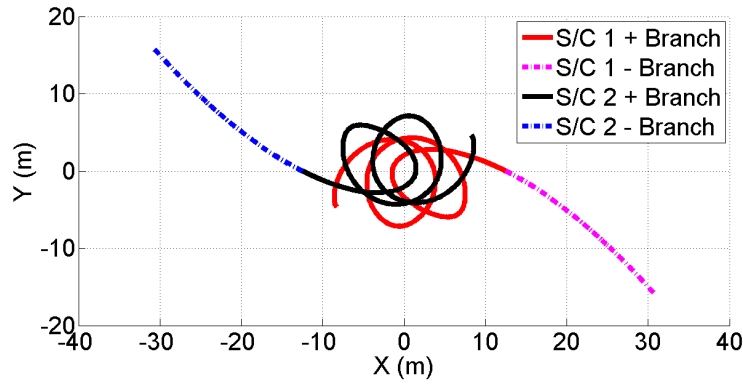


Figure 4.4: Radial S/C 1 and 2 Unstable Manifolds W^u , Propagated $1 T_p$

are representative of the general manifold structures, since no parameter bifurcations occur in the respective eigenspaces. This is true of the substantial symmetry between stable and unstable branches, and the two vehicles; however, the symmetry transformations between them would involve different scaling for unequal mass vehicles.

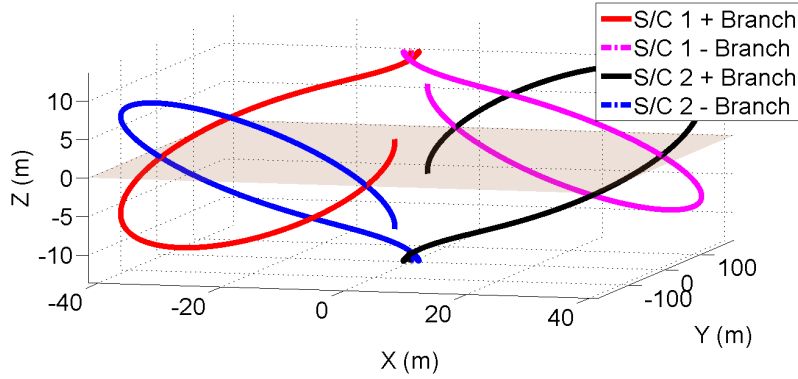


Figure 4.5: Orbit-Normal S/C 1 and 2 Stable Manifolds W^s , Propagated $2 T_p$

The Radial manifolds are planar with the + branches remaining near the origin under strong Coulomb interaction. The Orbit-Normal manifolds in Figures 4.5-4.6 exhibit two different oscillatory frequencies, and result in multiple piercings of the reference orbit plane at increasing distance from the origin. In addition to using in-

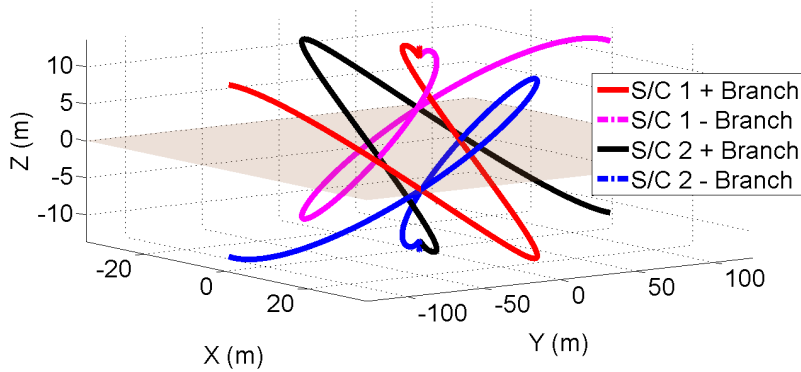


Figure 4.6: Orbit-Normal S/C 1 and 2 Unstable Manifolds W^u , Propagated $2 T_p$

variant manifolds to aid in optimal reconfigurations, some other possible applications of the theory, with respect to Coulomb formation navigation and control are discussed in Ref. 42.

4.5 Optimal Reconfiguration Methodology

The method presented in this section aims to more efficiently enable free-flying Coulomb formations to change shape, or reconfigure, through the application of invariant manifold theory and parameter optimization. First uncontrolled manifold trajectories, which complete as much of a transfer between two charged configurations as possible, are sought. This provides a near-heteroclinic, albeit discontinuous, initial guess (IG). A controlled variation of the charge product $\delta\tilde{Q}_{12}(\tau)$, and inertial thrusting are then introduced to a portion of the IG trajectory, to differentially correct the branches to match continuity, while minimizing a scalar cost function J . The optimization is solved using the direct method discussed in Section 2.7, by discretizing the craft 1 IG trajectory (craft 2 being explicitly dependent) into one uncontrolled and N controlled segments (per branch). The variation $\delta\tilde{Q}_{12}(\tau)$ is parameterized over each segment, and inertial thrusting is approximated by impulsive $\Delta\mathbf{v}$ maneuvers occurring at each segment node (total of $2N + 1$ maneuvers). The Eq. (4.1) cost function is adopted, so that total impulsive thrust ΔV is minimized.

$$J = \Delta V = \sum_{j=1}^{2N+1} \|\Delta\mathbf{v}_j\| \quad (4.1)$$

The general procedure for formulating and solving optimal Coulomb reconfigurations is outlined as follows.^{42,44}

1. Propagate a starting configuration unstable manifold $\mathbf{X}^u(\tau) \subset W^u$ from $0 \rightarrow \tau_{\max}^u$, and a target configuration stable manifold $\mathbf{X}^s(\tau) \subset W^s$ from $0 \rightarrow \tau_{\max}^s$, as described in Section 2.6.2. Let $\mathbf{X}_k^u \in W^u$ and $\mathbf{X}_k^s \in W^s$ denote discrete manifold state vectors at the propagation times τ_k^u and τ_k^s .

2. A state discontinuity between manifolds, $\mathbf{C}_k = (\mathbf{X}_k^s - \mathbf{X}_k^u)$, must be driven to zero for a continuous transfer to occur. Particular τ_k^u and τ_k^s values are found using a grid search, within the Eq. (4.2) user prescribed bounds, such that a scalar weighted norm function of \mathbf{C} (denoted Υ) is minimized.

$$\tau_{\min}^u \leq \tau_f^u \leq \tau_{\max}^u \quad \tau_{\min}^s \leq \tau_f^s \leq \tau_{\max}^s \quad (4.2)$$

From this initial brute force optimization, manifold propagation times τ_f^u and τ_f^s are obtained, such that a quality IG transfer is established. But with a state discontinuity \mathbf{C} at the patch point time $\tau_f = \tau_f^u$. The complete forward propagated IG trajectory is thus on W^u for $\tau = 0 \rightarrow \tau_f$, on W^s for $\tau = \tau_f \rightarrow (\tau_f^u + \tau_f^s) = \tau_{\text{tot}}$, and the total transfer duration τ_{tot} is bounded below by $(\tau_{\min}^u + \tau_{\min}^s)$ and above by $(\tau_{\max}^u + \tau_{\max}^s)$.

3. Equally spaced node times τ_j^u and τ_j^s are specified for the $2N$ control segments. If variable, these times are subject to the Eq. (4.3) inequality constraints.

$$0 < \tau_{j-1}^u < \tau_j^u < \tau_f \quad \tau_f < \tau_{j-1}^s < \tau_j^s < \tau_{\text{tot}} \quad \forall j \in 2 \dots N \quad (4.3)$$

4. The product $\tilde{Q}_{12}(\tau)$ is approximated, such that on the j th segment $\tilde{Q}_{12}(\tau) = \tilde{Q}_{12}(\tau_j) + \delta\tilde{Q}_{12}(\tau)$. The variation is parameterized as either piecewise constant $\delta\tilde{Q}_{12}(\tau) = \Delta Q_j$ or piecewise linear $\delta\tilde{Q}_{12}(\tau) = \dot{Q}_j(\tau - \tau_j)$. Also, the notation $\tilde{Q}_{12}^u(\tau)$ and $\tilde{Q}_{12}^s(\tau)$ is used to denote $\tilde{Q}_{12}(\tau)$ on each branch. Individual charge values are explicitly known, by assuming they adhere to the Eq. (2.22) convention of $|\tilde{q}_1(\tau)| = |\tilde{q}_2(\tau)|$ and $\tilde{q}_1(\tau) > 0$.

5. The parameter vector $\mathbf{X}_{\mathbf{p}}$ is defined as a subset of the following variables.

- Impulsive $\Delta \mathbf{v}$ maneuvers occurring at the $2N + 1$ control nodes.

- The $2N$ parameters ΔQ_j (or \dot{Q}_j) used to approximate the charge control variation piecewise, over each segment.
- $2N$ node times (τ_j^u and τ_j^s) and manifold propagation times (τ_f^u and τ_f^s).

Also each element of \mathbf{X}_p may have finite upper/lower limits defined, resulting in additional inequality constraints (e.g. Eq. (4.3) for free node times).

6. A nonlinear programming algorithm is used to find the optimizer \mathbf{X}_p , which minimizes the Eq. (4.1) performance index, subject to $\mathbf{C}(\tau_f) = 0$ (and any applicable inequality constraints \mathbf{D}).

This optimization formulation does not enforce charge continuity at the patch point, i.e. $\tilde{Q}_{12}(\tau_f) = \tilde{Q}_{12}^u(\tau_f) = \tilde{Q}_{12}^s(\tau_f)$. This is a reasonable relaxation of the problem so long as the jump between each individual charge $\tilde{q}_i^u(\tau_f)$ and $\tilde{q}_i^s(\tau_f)$ can occur in a relatively short time. Disregarding power limitations, this is valid since \tilde{q}_i can be throttled very quickly (kilovolt changes may be achieved on the order of milliseconds),⁴ especially relative to the trajectories being on the order of hours. However, big discontinuities at τ_f , and big ΔQ_j (or \dot{Q}_j) values may necessitate large power requirements (or a lowered I_{out} than used). Furthermore, increased validity of the impulsive charge control assumption equates to increased P_{out} , in accordance with Eqs. (2.4),(2.6). And enforcing the Eq. (2.22) convention on the individual charges can cause P_{out} to be higher than it need be otherwise. Although, these aspects, even for large discontinuities, are of minor concern, because of how fast the charge can be throttled relative to the spacecraft dynamical response.

Practical aspects of realizing and post processing the optimal control solutions, such as computing power required, are considered in Appendix A. Specifically, ex-

pressions are derived that relate charge control parameters to quantities like P_{out} , and the time required to ‘move’ a quantity of charge Δt_q . The Appendix A expressions can be used to analyze a solution’s feasibility, but also can lead to the establishment of parameter bounds, so that practical requirements (e.g. power limits) are satisfied. Such bounds are utilized, and in fact required when employing the Section 4.5.1 PSO method. And although not formally enforced here, the same expressions could be appended as inequality constraints \mathbf{D} , in the gradient based formulation, outlined in Section 4.5.2. Lastly, since some inertial maneuvers are necessary, the issue of thruster plume impingement becomes pertinent once again. This consideration is not formally handled here; however, an extension to this optimization methodology could treat this using inequality constraints, which enforce each thrust direction to be some angular distance away from the instantaneous \mathbf{r}_{12} vector.

4.5.1 Particle Swarm Optimization (PSO) Method

The Particle Swarm Optimization (PSO) method, outlined in Section 2.7.1, is used in solving the previously formulated optimal Coulomb reconfigurations. Numerical difficulties and overall problem sensitivity initially led to the adoption of this stochastic method, whose advantages include a simple implementation, independence from functional derivatives and their associated errors, and disregard for deceptive local behavior near the IG. Many PSO implementations employ a maximum iteration stopping criteria,³⁹ but in this work an alternate criteria is proposed and utilized. Specifically, convergence is said to occur when the current optimizer \mathbf{Z}_{min} results in satisfaction of the following two criteria.

1. Each element of \mathbf{C} is within a specified tolerance $\epsilon_{\mathbf{r}}$ (position), and $\epsilon_{\mathbf{v}}$ (velocity).

2. The mean \bar{J} for the entire population is within a user defined tolerance ϵ_c of the population's optimum augmented cost \bar{J}_{\min} .

The relatively few variables to be tuned when applying this method include $\boldsymbol{\alpha}$, N_{pop} , and the bounds on $\mathbf{X}_{\mathbf{p}}$ elements. The most problematic tend to involve $\boldsymbol{\alpha}$ values (penalty function weights), and the PSO method often will not converge upon a continuous transfer (i.e. not satisfy $\mathbf{C}(\tau_f) = 0$) when the order of magnitude of any of these weights are set improperly. Bounding the elements in $\mathbf{X}_{\mathbf{p}}$ is both beneficial and problematic. For the problem at hand, bounds on ΔQ_j (or \dot{Q}_j) are determined using Appendix A expressions, such that a reasonably small transition time Δt_q and a realistic maximum power limit are enforced.

In contrast, there is no analytical basis for bounding $\Delta \mathbf{v}$ component magnitudes, nor the times τ_j^u and τ_j^s , but theoretically deviations in these quantities should remain relatively small in order to remain in the vicinity of the quality IG. Bounds on $\Delta \mathbf{v}$ components, used in generating the example results of Section 4.6, were born out of trial-and-error, by what tended to facilitate convergence and higher quality optima. The relative magnitudes between charge control bounds and $\Delta \mathbf{v}$ bounds is found to have a significant impact on the quality of the optima achieved using the PSO method. This necessary constraining of the problem could be quite positive in a more applied scenario, but in general the limits (or bounds) are fairly arbitrary, and often difficult to define.

4.5.2 Sequential Quadratic Programming (SQP) Method

In contrast to PSO, gradient based methods (e.g. SQP) rely less heavily on non intuitive heuristics, and constraints are handled readily and without much

concern. But a substantial initial investment is necessary for such a method, and associated algorithm, to deliver consistent convergence in reasonable computational time. Much of this effort involves deriving variational equations for the multi-arc trajectory. That is, gradients of the cost function and constraints with respect to independent parameters, which are required when employing this method. To do so let Eq. (4.4) define a two-craft augmented state vector \mathbf{Y} , in which \tilde{Q}_{12} and its derivative with respect to τ , are appended to \mathbf{X} .

$$\mathbf{Y}(\tau) = \begin{bmatrix} \mathbf{r}_1 \\ \mathbf{v}_1 \\ \tilde{Q}_{12} \\ \tilde{Q}'_{12} \end{bmatrix}_{8 \times 1} \quad (4.4)$$

The augmented state differential at the τ_{j+1} node is then given by Eq. (4.5), where impulsive changes to \mathbf{Y} and time differentials at the previous and current node are considered.⁶⁴

$$d\mathbf{Y}_{j+1}^+ = \left(\frac{\partial \mathbf{Y}_{j+1}^-}{\partial \mathbf{Y}_j^+} \right) \left[d\mathbf{Y}_j^- + d\Delta \mathbf{Y}_j - \dot{\mathbf{Y}}_j^+ d\tau_j \right] + \dot{\mathbf{Y}}_{j+1}^- d\tau_{j+1} + d\Delta \mathbf{Y}_{j+1} \quad (4.5)$$

This provides the variation of \mathbf{Y}_{j+1}^+ , with respect to all terms on the right hand side of Eq. (4.5), through first order gradients. The effect of differentials at earlier sequential nodes, are also easily computed simply by expanding this implicit equation. Moreover, the term $\frac{\partial \mathbf{Y}_{j+1}^-}{\partial \mathbf{Y}_j^+}$ is simply the STM evaluated between τ_j and τ_{j+1} . Therefore, in the implementation of this solver method, the associated STM matrix is numerically integrated alongside \mathbf{Y} . The state propagation matrix for this augmented system, used to propagate the corresponding STM matrix, is derived in Appendix B. The Eq. (4.5) variational equation is then used to provide partial derivatives of $\mathbf{Y}(\tau_f)$, with respect to independent differentials at all previous nodes. From there it is relatively

easy, as shown in Appendix B, to obtain the first order partial derivatives of J and \mathbf{C} with respect to \mathbf{X}_p .

In addition to the analytical gradients, the adopted *VF13* algorithm can be sensitive to poorly scaled problems. Therefore scaling J , \mathbf{C} , \mathbf{X}_p , and all derivatives to be near unity is crucial to achieving consistent convergence. Therefore, scale factors for these terms are the primary variables that require some tuning when employing this method.

4.6 Numerical Examples of Optimal Reconfigurations

Only time-fixed solutions are presented in the following examples, which also maintain the numerical assumptions used in Section 4.4. PSO method results are obtained using the Table 4.2 convergence tolerances, parameter bounds, and population size (unless noted otherwise). Solutions obtained using the gradient based method

Table 4.2: PSO Method Numerical Result Input Parameters

Parameter	Value	Units
ϵ_r	$1.0e^{-3}$	meter
ϵ_v	$1.0e^{-6}$	meter/s
ϵ_c	$1.0e^{-7}$	-
$ \Delta v _{\max}$	1.0	cm/s
$(\Delta t_q)_{\max}$	1.0	ms
N_{pop}	30	-

also adhere to the Table 4.2 constraint tolerances, enforced using a simple alteration to the *VF13* algorithm. Equation (4.6) is used to define Υ , an L_1 weighted norm function of \mathbf{C} . Recalling that a grid search minimization of Υ yields quality manifold

propagation times τ_f^u and τ_f^s .

$$\Upsilon = \|\mathbf{r}^s(\tau_k^s) - \mathbf{r}^u(\tau_k^u)\|_1 + 1000 \omega \|\mathbf{v}^s(\tau_k^s) - \mathbf{v}^u(\tau_k^u)\|_1 \quad (4.6)$$

Where, $\mathbf{r}^u/\mathbf{r}^s$ and $\mathbf{v}^u/\mathbf{v}^s$ denote craft 1 position and (scaled) velocity vectors on the unstable/stable manifold branches at particular τ_k^u / τ_k^s propagation times. Results are presented in dimensional time t ($t = \tau/\omega$), and with charge control in terms of $\phi_1(t)$ (with its more intuitive Voltage units), using the Eq. (2.22) transformation. Optimal costs are for craft 1 only, and therefore the ΔV required would be twice that quantity, for the total formation. Lastly, the maximum P_{out} results are computed via Eq. (2.4), using worst case constant I_{out} , and therefore represent conservatively high power estimates.

Radial configuration manifolds are planar and a comparison of Figure 4.3 (stable) with Figure 4.4 (unstable) alludes to the possible existence of nearly tangential crossings of the respective manifold branches (near-heteroclinic orbits). Because of this observation, transfers between Radial configurations, which result in either an expansion (increase in r_{12}^*) or contraction (decrease in r_{12}^*), are considered first in Sections 4.6.1-4.6.3. In part, these serve to advance to the more complicated reconfiguration scenarios that follow.

4.6.1 PSO Method Radial Expansions and Contractions

Two PSO optimized Radial→Radial examples are illustrated in Figure 4.7 (an expansion) and in Figure 4.8 (a contraction). These transfers are generated using Table 4.2 values and with $\tau_{\text{max}}^u = \tau_{\text{max}}^s = 0.7\omega T_p$ and $\tau_{\text{min}}^u = \tau_{\text{min}}^s = 0.5\omega T_p$ (total transfer bounded between 1 and 1.4 days), 15 – 18% of the total transfer duration having control variation, and the piecewise linear $\delta\tilde{Q}_{12}(\tau)$ parameterization.

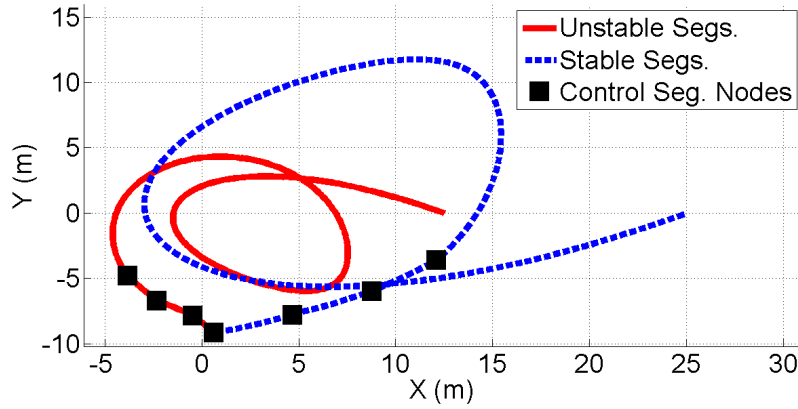


Figure 4.7: PSO Optimal Radial→Radial Expansion, $r = 12.5 \rightarrow 25$ m

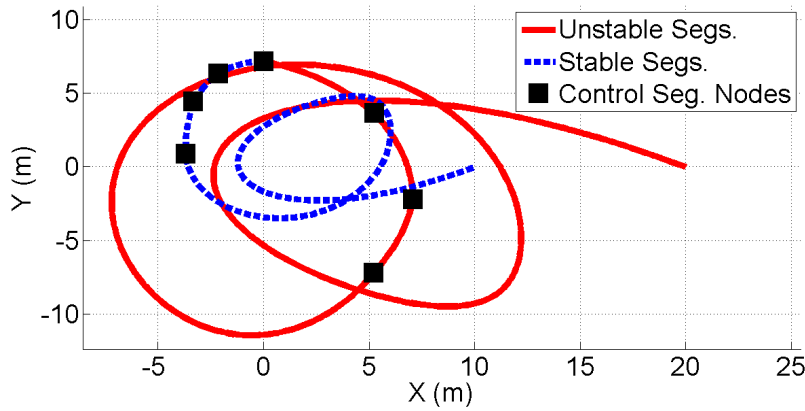


Figure 4.8: PSO Optimal Radial→Radial Contraction, $r = 20 \rightarrow 10$ m

The respective optimal control histories ($\phi_1(t)$ and $\Delta \mathbf{v}$ radial and transverse components) are presented in Figures 4.9(a)-4.9(b). These show a large maneuver at the patch point and smaller maneuvers elsewhere, which tends to be characteristic of solutions obtained using PSO. These example results, and others obtained using the PSO method are summarized in Table 4.3, with charge control parameter limits transformed to ϕ_1 units via Eq. (2.22).

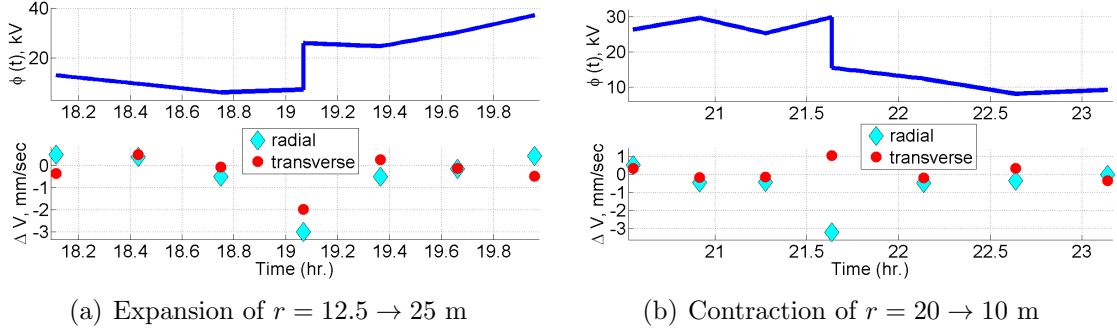


Figure 4.9: PSO Optimal Control for Radial→Radial Reconfigurations

Table 4.3: PSO Method Optimized Radial→Radial Transfers with $N = 3$

Shape Change, m	$\delta\tilde{Q}_{12}$ Model	$(\tau_1/\tau_f)^u$	$(\tau_N/\tau_f)^s$	$ \Delta\phi_1 _{\max}$, kV $(\dot{\phi}_1 _{\max}$, V/s)	Max. P_{out} , W	Transfer Time, days	Cost, mm/s
12.5 → 25	ΔQ	8%	7%	1.00	4.5	1.022	6.34
12.5 → 25	\dot{Q}	8%	7%	0.63	3.1	1.022	6.74
20 → 10	ΔQ	7%	11%	1.00	3.2	1.194	5.47
20 → 10	\dot{Q}	7%	11%	2.30	2.2	1.194	6.22
12.5 → 15	ΔQ	7%	8%	1.00	2.2	0.526	3.01
12.5 → 15	\dot{Q}	7%	8%	0.15	1.4	0.526	2.75

4.6.2 SQP Method Radial Expansions and Contractions

Identical IG trajectories used in obtaining the Table 4.3 PSO method results are repeated here, and reconverged by applying the gradient based SQP method. In Figures 4.10-4.11, optimal control histories for the $r = 20 \rightarrow 10$ m contraction are shown, for the impulsive and linear approximations, respectively. These depict the variation in $\delta\phi_1(t)$, in contrast to the $\phi_1(t)$ history used in Figures 4.9(a)-4.9(b). These solutions do not reflect the large maneuver at τ_f , as in the PSO solutions. Optimal results are summarized in Table 4.4, and in all cases SQP obtains lower cost than PSO, in part because the gradient based method achieves ‘deeper convergence.’

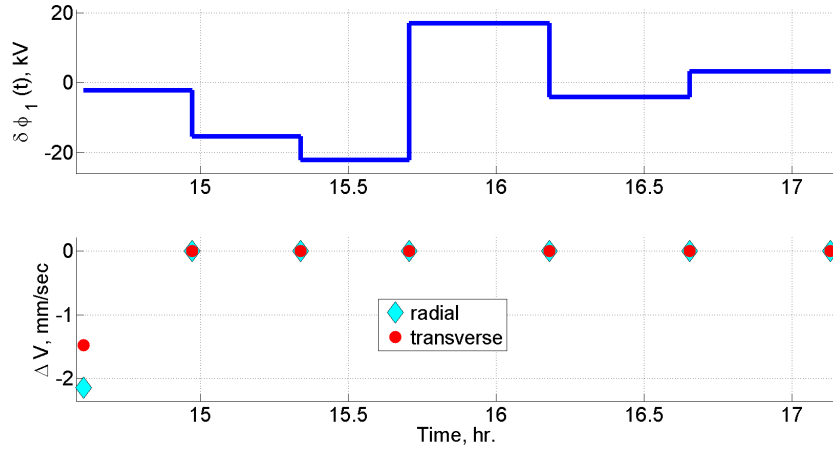


Figure 4.10: SQP Impulsive Optimal Control for Radial→Radial, $r = 20 \rightarrow 10$ m

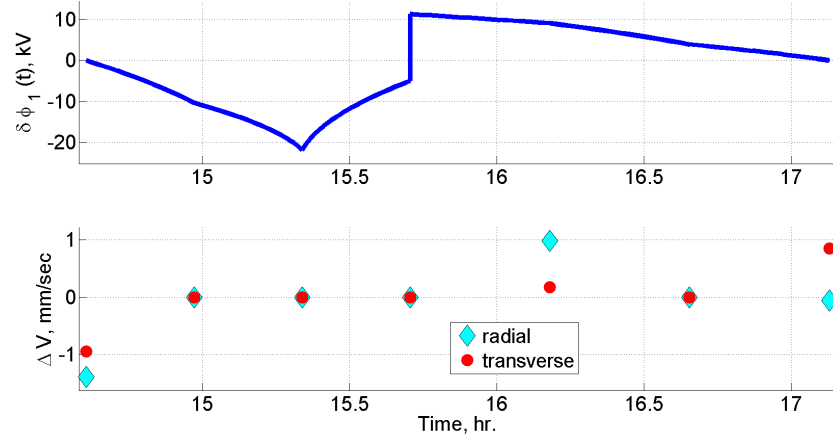


Figure 4.11: SQP Linear Optimal Control for Radial→Radial, $r = 20 \rightarrow 10$ m

However, the results do not perfectly compare because of the charge control parameter limits imposed in the PSO formulation. An example of how the SQP results and PSO results do not perfectly compare, is contained within Figure 4.10. At the same I_{out} value, the Figure 4.10 impulsive charge changes result in maximum transition time of $(\Delta t_q)_{max} = 25.2$ ms (compared with 1.0 ms for PSO), and maximum power of $P_{out} = 6.4$ W (compared with 3.2 W for PSO). On the other hand, the optimal linear solution does satisfy the bounds imposed on the corresponding PSO formulation.

Table 4.4: SQP Method Optimized Radial→Radial Transfers with $N = 3$

Shape Change, m	$\delta\tilde{Q}_{12}$ Model	$(\tau_1/\tau_f)^u$	$(\tau_N/\tau_f)^s$	Transfer Time, days	Cost, mm/s
12.5 → 25 m	ΔQ	8%	7%	1.022	3.77
12.5 → 25	\dot{Q}	8%	7%	1.022	4.41
20 → 10 m	ΔQ	7%	11%	1.194	2.60
20 → 10	\dot{Q}	7%	11%	1.194	3.52
12.5 → 15	ΔQ	7%	8%	0.526	0.59
12.5 → 15	\dot{Q}	7%	8%	0.526	0.72

Figure 4.12 depicts the resulting $r = 20 \rightarrow 10$ m trajectory for the linear approximated charge control solution. This plot exhibits additional curvature compared with Figure 4.8, as a result of increased electrostatic forcing.

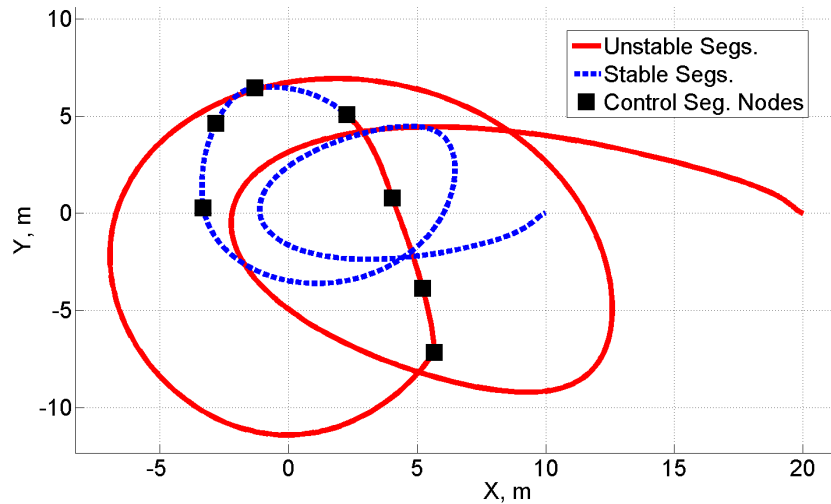


Figure 4.12: SQP Optimal Radial→Radial Contraction, $r = 20 \rightarrow 10$ m

4.6.3 Improved Optima with Alternate Problem Formulations

In this section it is demonstrated that optimal solutions are affected by the optimization problem formulation, and the values assigned to parameters in the methodology. To qualitatively understand these effects, problem formulation parameters are altered, one at a time, from a nominal set of parameters.

For the PSO method, the Section 4.6.1 $r = 12.5 \rightarrow 15$ m expansion formulation and optimal result are used as nominal, chosen partly because of the relative ease in obtaining converged solutions. The Figure 4.13 IG is used for all runs (0.526 day

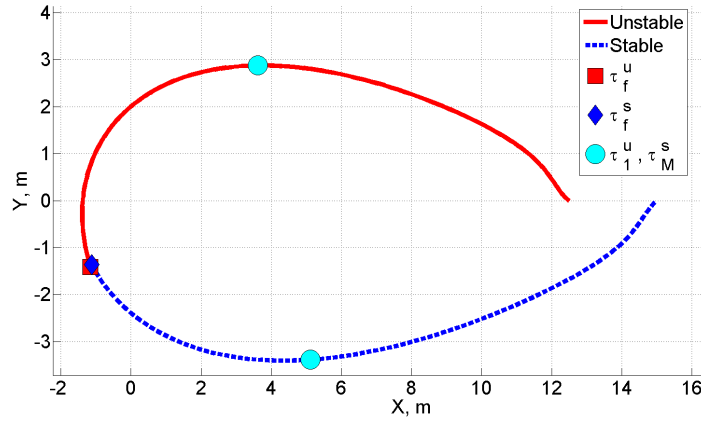


Figure 4.13: PSO Nominal Radial→Radial IG, $r = 12.5 \rightarrow 15$ m

transfer), and the parameters N_{pop} , τ_1^u , τ_N^s , and charge control bounds are varied from their Table 4.2 and Table 4.3 nominal values. Table 4.5 summarizes deviations in the optimal cost for different problem formulations, relative to the nominal. Overall the changes to the optima are fairly small, and there are few if any noticeable trends. The latter aspect demonstrates how difficult it can be to reasonably select and tune parameters, when employing the PSO method.

For the SQP method, the Table 4.4 results (and corresponding problem for-

Table 4.5: Permutations to PSO Method Optimal Radial→Radial Expansion

$\delta\tilde{Q}_{12}$ Model	N_{pop}	$(\tau_1/\tau_f)^u$	$(\tau_N/\tau_f)^s$	$ \Delta\phi_1 _{\text{max}}$, kV ($ \dot{\phi}_1 _{\text{max}}$, V/s)	Cost, mm/s	Nominal Cost, mm/s
ΔQ	30	10%	10%	1.00	2.45	3.01
ΔQ	30	20%	20%	1.00	2.08	3.01
ΔQ	30	7%	8%	2.00	3.12	3.01
ΔQ	30	7%	8%	0.90	2.74	3.01
\dot{Q}	20	7%	8%	0.15	2.50	2.75
\dot{Q}	60	7%	8%	0.15	2.97	2.75
\dot{Q}	30	10%	10%	0.15	3.00	2.75
\dot{Q}	30	20%	20%	0.15	3.11	2.75
\dot{Q}	30	7%	8%	0.3	3.07	2.75
\dot{Q}	30	7%	8%	0.1	2.98	2.75

mulations) are considered nominal.

Important permutations to the problem formulation include changes to N , $\tau_{\text{min}}^{u/s}$ and $\tau_{\text{max}}^{u/s}$ (for generating the IG), and τ_1^u and τ_N^s (for establishing the duration in which control variations occur). Improved IG trajectories (in terms of small Υ) for

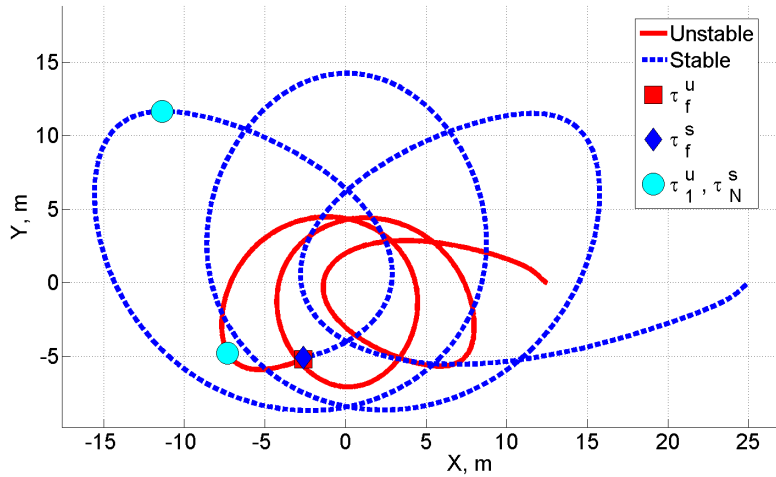


Figure 4.14: Alternate IG for Radial→Radial Expansion, $r = 12.5 \rightarrow 25$ m

the Radial expansion and contraction of Section 4.6.2 are shown in Figures 4.14-4.15.

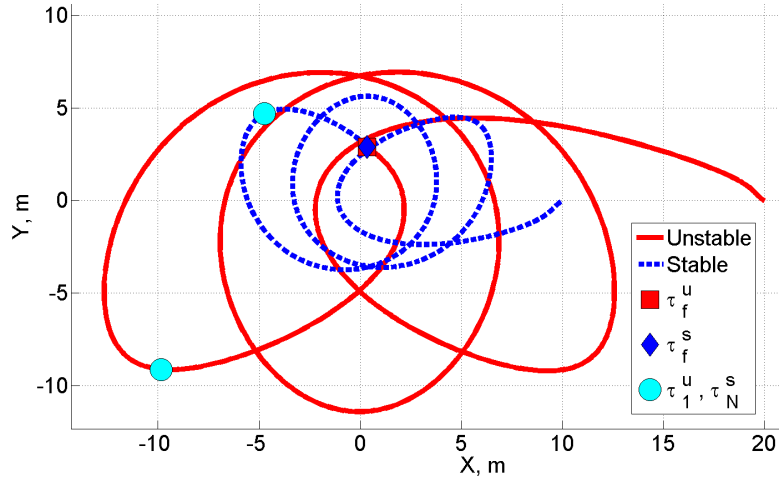


Figure 4.15: Alternate IG for Radial→Radial Contraction, $r = 20 \rightarrow 10$ m

These were determined by considering a larger transfer duration range of 1-2 days, which yields IG transfers of 1.680 days (expansion) and 1.637 days (contraction). The effect that the new IG trajectories have on the optimal cost, as well as the effect of the other important formulation permutations are summarized in Table 4.6. It is

Table 4.6: Permutations to SQP Method Optimal Radial→Radial Transfers

Shape Change, m	$\delta\tilde{Q}_{12}$ Model	N	$(\tau_1/\tau_f)^u$	$(\tau_N/\tau_f)^s$	Transfer Time, days	Cost, mm/s	Nominal Cost, mm/s
12.5 → 25	ΔQ	3	5%	5%	1.680	2.09	3.77
12.5 → 25	ΔQ	3	7%	7%	1.680	1.62	3.77
12.5 → 25	ΔQ	6	5%	5%	1.680	2.06	3.77
12.5 → 25 m	\dot{Q}	3	5%	5%	1.680	1.84	4.41
12.5 → 25	\dot{Q}	3	7%	7%	1.680	1.58	4.41
20 → 10 m	ΔQ	3	4%	6%	1.637	1.50	2.60
20 → 10	ΔQ	3	6%	10%	1.637	1.31	2.60
20 → 10	ΔQ	6	4%	6%	1.637	1.45	2.60

clear that the alternate IG result in lower optimal ΔV , but this comes at the expense of longer transfer times (although still within the specified, and presumably tolerable bounds). Furthermore, optimal ΔV improvements are witnessed upon altering the duration of the transfer having control variations (via τ_1^u and τ_N^s ratios), and also with the number of segments N . This is expected, since these represent improved approximations of the theoretical optimal controls.

Radial expansions and contractions are relatively easy to visualize and converge, and therefore serve as ideal verifiable demonstrations of the Section 4.5 methodology. However, these represent fairly impractical reconfigurations since the Radial equilibria case is known to exhibit full Coulomb force controllability in the $\hat{e}_R\text{-}\hat{e}_T$ plane,³⁵ and because the manifold branches tend to be near the origin, signaling potentially dangerous close encounters of the vehicles. The following sections hence consider the more complex but practical reconfiguration scenarios, albeit in less detail.

4.6.4 Orbit-Normal Expansions and Contractions

Manifolds associated with the Orbit-Normal configuration evolve more slowly, due to the oscillatory nature of those modes, and reconfigurations involving them require more time than those previously considered. An Orbit-Normal expansion from a separation distance of $r = 30$ m to $r = 40$ m, with IG bounded between 2 and 6 days, is considered as an example. An SQP optimized solution for this expansion is shown in Figure 4.16, corresponding to a total transfer duration of 4.8 days, and generated using $N = 3$ and impulsive $\delta\tilde{Q}_{12}(\tau)$. A different optimal solution for the equivalent shape change is provided by Figure 4.17. This solution has total transfer duration of 3.4 days, and also results from $N = 3$ and impulsive $\delta\tilde{Q}_{12}(\tau)$. Optimal control histories corresponding to Figures 4.16-4.17 are provided respectively

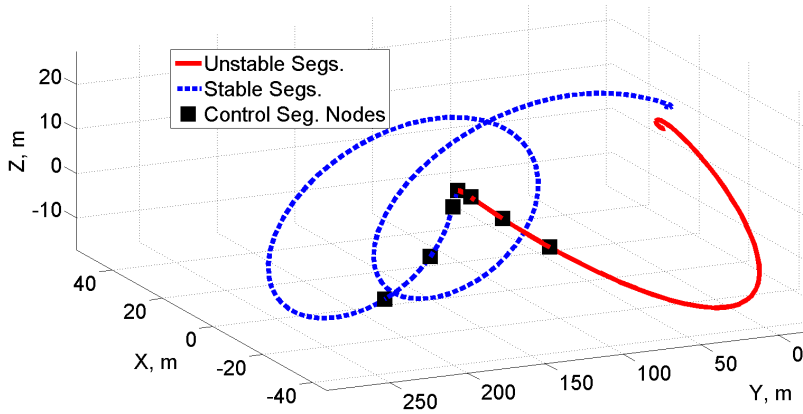


Figure 4.16: SQP Optimal Orbit-Normal→Orbit-Normal, $r = 15 \rightarrow 20$ m

by Figures 4.18(a)-4.18(b). In these optimal solutions, jumps in $\phi_1(\tau)$ of around 40 kV occur. This equates to a maximum transition time of $(\Delta t_q)_{\max} = 55$ ms and maximum power of $P_{\text{out}} = 10.4$ W.

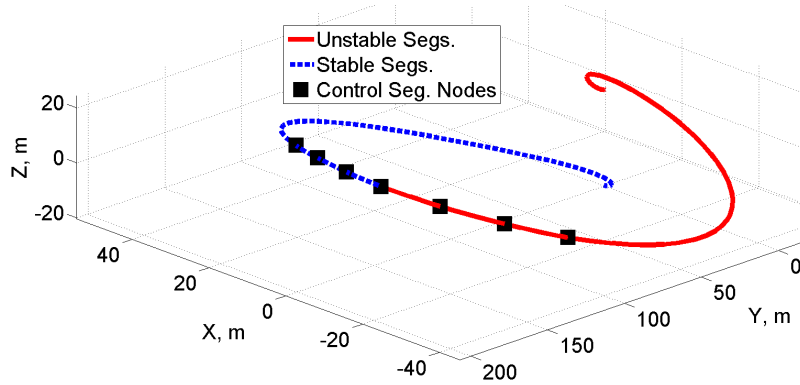


Figure 4.17: SQP Optimal Orbit-Normal→Orbit-Normal, with Craft 1→Craft 2, $r = 15 \rightarrow 20$ m

The primary difference between the Figure 4.16 and Figure 4.17 solutions, is that the latter reconfiguration takes craft 1 from $r = 15$ m to the craft 2 equilibrium position at $r = -20$ m, and therefore $\tilde{q}_1^* \rightarrow \tilde{q}_2^*$. This change in spacecraft numbering at the patch point, provides better exploitation of the antisymmetry in the manifold

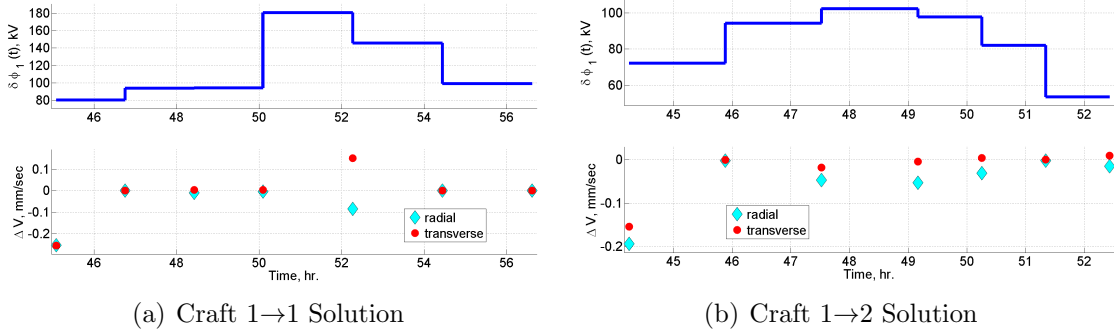


Figure 4.18: SQP Impulsive Optimal Control for Orbit-Normal \rightarrow Orbit-Normal Expansions, $r = 15 \rightarrow 20$ m

branches, and therefore tends to yield lower ΔV at shorter transfer durations. Moreover, doing so is permissible so long as $m_1 = m_2$ (assumed) and for $\tilde{q}_1(\tau) = \tilde{q}_2(\tau)$. The latter is true for Orbit-Normal equilibria, since individual charges at equilibrium have the same sign, and because equal charge magnitude is assumed by convention. Therefore within the assumed model and charge convention, crafts 1 and 2 are interchangeable, when considering Orbit-Normal expansions and contractions.

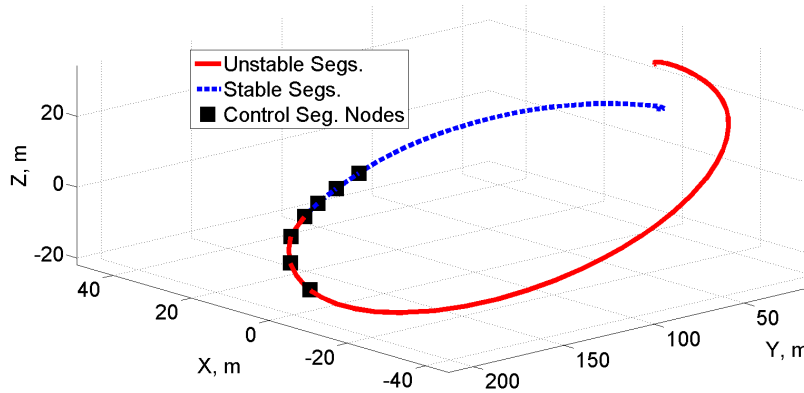


Figure 4.19: SQP Optimal Orbit-Normal \rightarrow Orbit-Normal, $r = 25 \rightarrow 12.5$ m

Orbit-Normal contractions are also easily obtained using this method, but do not benefit from craft numbering changes (in contrast to expansion transfers). An

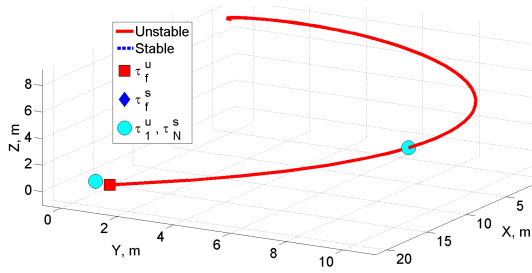
Table 4.7: SQP Method Optimized Orbit-Normal→Orbit-Normal Transfers

Shape Change, m	$\delta\tilde{Q}_{12}$ Model	N	$(\tau_1/\tau_f)^u$	$(\tau_N/\tau_f)^s$	Transfer Time, days	Cost, mm/s
15 → 20	ΔQ	3	10%	10%	4.805	0.969
15 → 20	\dot{Q}	3	10%	10%	4.805	1.095
15 → -20	ΔQ	3	10%	10%	3.410	0.641
15 → -20	ΔQ	6	10%	10%	3.410	0.621
15 → -20	\dot{Q}	3	10%	10%	3.410	0.665
25 → 12.5	ΔQ	3	10%	10%	2.855	1.700
25 → 12.5	\dot{Q}	3	10%	10%	2.855	1.743

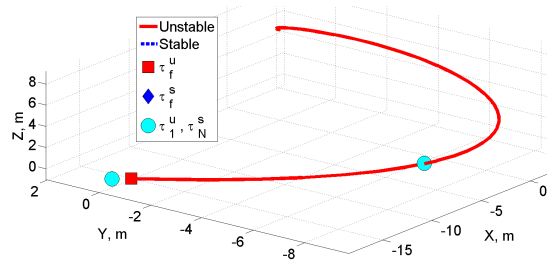
example, SQP optimized contraction trajectory is shown in Figure 4.19. This has a total transfer duration of 2.85 days, and is converged using $N = 3$ and impulsive $\delta\tilde{Q}_{12}(\tau)$. Example, SQP optimized, orbit-normal expansion and contraction results are summarized in Table 4.7. Linear parameterized charge control solutions tend to yield lower P_{out} than impulsive, but nevertheless, determining what is acceptable or not, remains highly subjective (and application specific).

4.6.5 Transfers between Radial and Orbit-Normal

Recall that Orbit-Normal manifolds repeatedly pierce the $\hat{e}_R\text{-}\hat{e}_T$ plane with increasingly large y component, but x and z components remain bounded. Whereas, Radial manifolds, confined to the $\hat{e}_R\text{-}\hat{e}_T$ plane, either remain near the origin or exponentially depart. Unfortunately, for transfers between these two configurations, initial piercings of the plane (smaller y) occur in directions nearly opposite that of nearby opposing (stable or unstable) Radial branches. Furthermore, there are no nearby Radial manifolds for large y magnitude crossings. Upon further analysis, it



(a) Craft 1→1, $r = 7.5 \rightarrow 17.5$ m



(b) Craft 1→2, $r = 7.5 \rightarrow 17.5$ m

Figure 4.20: Orbit-Normal→Radial Realignment and Expansion IG

is determined that the best use of invariant manifolds, in this scenario, is to consider only the Orbit-Normal branch, controlling it to target an unpropagated Radial state (equilibrium). The craft numbering can either change (as in Section 4.6.4), or not, and the highest quality IG tend to occur for small expansions in $r_{12}^* = r$. With these considerations, two example Orbit-Normal→Radial IG expansions are shown in Figures 4.20(a)-4.20(b). Figure 4.20(a) does not involve a craft number change, and

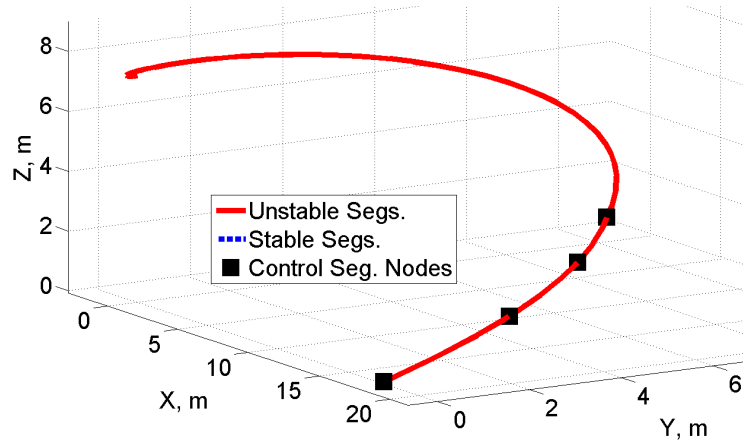


Figure 4.21: SQP Optimal Orbit-Normal→Radial Realignment and Expansion, $r = 7.5 \rightarrow 17.5$ m

utilizes the $-$ branch of W^u . Whereas the Figure 4.20(b) IG has vehicle 1 transferring along the $+$ branch of W^u , to the Radial configuration craft 2 slot, which is at static

equilibrium (unpropagated).

Figure 4.21 demonstrates an SQP method optimization of the Figure 4.20(a) IG, for $N = 3$ and an impulsive $\delta\tilde{Q}_{12}(\tau)$ parameterization. Although transfers like Figures 4.20(a)-4.20(b) are ideal, many other transfers are certainly achievable. As an example, an optimized transfer without changing r is presented in Figure 4.22(a), alongside its corresponding optimal control history in Figure 4.22(b). These example optimal results are summarized in Table 4.8.

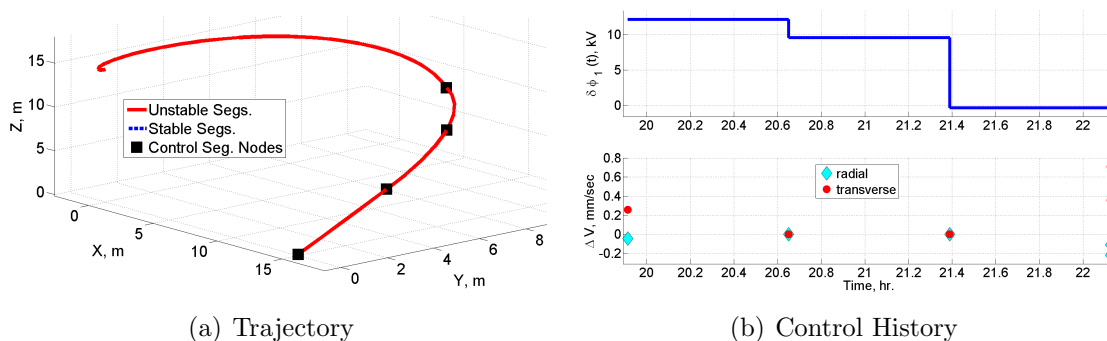


Figure 4.22: SQP Optimal Orbit-Normal \rightarrow Radial Realignment, $r = 15$ m

If considering Orbit-Normal to Radial transfers that involve a craft number change, as in the Figure 4.20(b) IG, $\tilde{q}_1(\tau) = \tilde{q}_2(\tau)$ between branches is no longer true by convention. However, interchangeability of craft 1 and 2 may still be reasonable if the patch point charge discontinuity (now involving a sign change) can be transitioned nearly impulsively. But doing so with reasonable P_{out} , while not enforcing $\tilde{Q}_{12}(\tau_f)$ continuity is likely invalid, since the $\tilde{Q}_{12}(\tau_f)$ discontinuity is necessarily large. However, the magnitude of the discontinuity may be decreased by relaxing the $|\tilde{q}_1(\tau)| = |\tilde{q}_2(\tau)|$ convention. Such aspects are considered further in Appendix A.

Table 4.8: SQP Method Optimized Orbit-Normal→Radial Transfers

Shape Change, m	$\delta\tilde{Q}_{12}$ Model	N	$(\tau_1/\tau_f)^u$	$(\tau_N/\tau_f)^s$	Transfer Time, days	Cost, mm/s
7.5 → 17.5	ΔQ	3	10%	0%	0.93	2.63
7.5 → 17.5	ΔQ	6	10%	0%	0.93	2.30
7.5 → 17.5	\dot{Q}	3	10%	0%	0.93	2.70
15 → 15	ΔQ	3	10%	0%	0.92	2.92

4.6.6 Evaluating the Optimal Costs

In this section, a measure is established to ascertain the quality of the optimal costs achieved in Sections 4.6.1-4.6.5. The Clohessy-Wiltshire-Hill equations of relative motion,²⁷ in the absence of Coulomb forces, are ideal for generating this baseline. These equations of motion have a well known closed form solution, given by Eq. (4.7) for craft 1, in the non dimensional time variable τ .

$$\begin{bmatrix} \mathbf{r}_1(\tau) \\ \dot{\mathbf{r}}_1(\tau) \end{bmatrix} = \begin{bmatrix} 4-3\cos(\tau) & 0 & 0 & \frac{1}{\omega}\sin(\tau) & \frac{2}{\omega}[1-\cos(\tau)] & 0 \\ 6[\sin(\tau)-\tau] & 1 & 0 & \frac{2}{\omega}[\cos(\tau)-1] & \frac{1}{\omega}[4\sin(\tau)-3\tau] & 0 \\ 0 & 0 & \cos(\tau) & 0 & 0 & \frac{1}{\omega}\sin(\tau) \\ 3\omega\sin(\tau) & 0 & 0 & \cos(\tau) & 2\sin(\tau) & 0 \\ 6\omega[\cos(\tau)-1] & 0 & 0 & -2\sin(\tau) & 4\cos(\tau)-3 & 0 \\ 0 & 0 & -\omega\sin(\tau) & 0 & 0 & \cos(\tau) \end{bmatrix} \begin{bmatrix} \mathbf{r}_1(\tau_0) \\ \dot{\mathbf{r}}_1(\tau_0) \end{bmatrix} \quad (4.7)$$

From Eq. (4.7), an analytical two impulse solution to the boundary value problem may be computed, where the boundary constraints correspond to starting and target static equilibria conditions. This then provides a consistent baseline cost for achieving a shape change, in the same τ_{tot} as the numerically optimized solution. And it represents the linearized, relative motion, equivalent of solving Lambert's problem

in the Keplerian gravity model, with specified time of flight.⁶⁵ The analytical two impulse solution is computed as follows ($\tau_0 = 0$ assumed).

1. Algebraically solve for the initial impulse $\dot{\mathbf{r}}_1(\tau_0)$ from the $\mathbf{r}_1(\tau)$ terms of Eq. (4.7). With $\tau = \tau_{\text{tot}}$, and for specified starting configuration $\mathbf{r}_1(\tau_0)$ and target configuration $\mathbf{r}_1(\tau_{\text{tot}})$ position vectors.
2. The final impulse $\dot{\mathbf{r}}_1(\tau_{\text{tot}})$ is then equal to the three $\dot{\mathbf{r}}_1(\tau)$ components of Eq. (4.7), with $\tau = \tau_{\text{tot}}$, $\mathbf{r}_1(\tau_0)$, and $\dot{\mathbf{r}}_1(\tau_0)$ substituted.

Cost comparisons between SQP method optimal reconfigurations and the baseline two impulse analytical solutions are summarized in Table 4.9. It is evident that even with relatively coarse control approximations, the optimization does provide a reduction in ΔV cost, versus a baseline measure. Moreover, it is hypothesized that the resulting optimal ΔV will be driven even closer to zero with increased N , higher order approximations for $\delta\tilde{Q}_{12}(\tau)$, the allowance of free times, and with further tuning of the method. Evidence in support of this hypothesis (at least in part) is supplied in Section 4.6.3, but no matter how close or far from the true optimal control solution, these parameterized solutions yield clear and measurable reductions in fuel cost.

4.6.7 Performance of SQP versus PSO Method

The PSO method was adopted initially as a way to readily achieve results, while avoiding some of the numerical difficulties and sensitivities which often impede gradient based methods. However, upon addressing numerical sensitivity issues in the problem via scaling, the use of non dimensional dynamics, and the implementation of analytical gradients the SQP method was found to outperform PSO. Specifically, by

Table 4.9: SQP Method Optimal Costs versus Two Impulse Baseline Costs

Shape Change, m	$\delta\tilde{Q}_{12}$ Model	Transfer Time, days	Optimized Cost, mm/s	Baseline Cost, mm/s
Radial \rightarrow Radial				
12.5 \rightarrow 25	ΔQ	1.022	3.77	15.34
12.5 \rightarrow 25	\dot{Q}	1.022	4.41	15.34
20 \rightarrow 10	ΔQ	1.194	2.60	5.34
20 \rightarrow 10	\dot{Q}	1.194	3.52	5.34
12.5 \rightarrow 15	ΔQ	0.526	0.59	3.82
12.5 \rightarrow 15	\dot{Q}	0.526	0.72	3.82
Orbit-Normal \rightarrow Orbit-Normal				
15 \rightarrow 20	ΔQ	4.81	0.97	1.95
15 \rightarrow 20	\dot{Q}	4.81	1.095	1.95
15 \rightarrow -20	ΔQ	3.41	0.62	1.16
15 \rightarrow -20	\dot{Q}	3.41	0.67	1.16
25 \rightarrow 12.5	ΔQ	2.86	1.70	3.20
25 \rightarrow 12.5	\dot{Q}	2.86	1.74	3.20
Orbit-Normal \rightarrow Radial				
7.5 \rightarrow 17.5	ΔQ	0.93	2.30	6.97
7.5 \rightarrow 17.5	\dot{Q}	0.93	2.70	6.97
15 \rightarrow 15	ΔQ	0.92	2.92	6.58

delivering higher quality results, with more consistency. The gradient based method exhibits a steady drive towards the optima, whereas this property of descent is not found to occur in PSO. Once properly scaled and benefiting from analytical gradients, the *VF13* algorithm provides repeatable and high quality results, with infrequent divergence. In contrast, PSO convergence is inconsistent, and certainly not reliable. And additional convergence difficulties are encountered as the size of \mathbf{X}_p increases, as

constraints are added, and with increased N_{pop} (or generally with increased problem complexity).

The PSO method necessitates parameter bounds, and therefore practical requirements, such as power limits, are easily built into the problem without added computational complexity. But such bounds can be arbitrary, or difficult to define in general, and can unnecessarily restrict the problem. In contrast, constraints would need to be added to the gradient based method to enforce such bounds, thereby adding complexity. Overall, a well constructed SQP method delivers enhanced optima with reliable convergence behavior, but the power required is not always comparably bounded with PSO. The initial benefits of not needing a quality IG or gradients (and their associated sensitivities), is eventually overwhelmed by trouble achieving reliable convergence and the non intuitive affect of tunable parameters, such as population size and constraint weights. Nevertheless, PSO might be useful in providing an improved IG, prior to executing the SQP method.

4.7 Chapter Conclusions and Additional Considerations

This research shows how invariant manifold theory can aid in targeting reconfigurations, between 2-craft Coulomb formation equilibria, to minimize consumables. The general methodology for optimizing Coulomb reconfigurations exploits uncontrolled flow along invariant manifolds, to complete as much of the trajectory as possible; however, the natural motions necessitate transfers on the order of days. There are many numerical challenges in converging these trajectories, because of the hybrid control formulation, limited Coulomb force controllability, and overall sensitivity. Two nonlinear program solvers, one stochastic based and one gradient based,

are employed in converging the solutions, and each has specific positive and negative attributes. The PSO method eases many numerical and initial guess difficulties, and provides quick solutions to less complex formulations; however, consistent PSO convergence remains troublesome and this worsens with problem size and complexity. In contrast, the gradient based method requires functional derivatives via numerical integration, and these can be prone to round-off errors. However, once properly constructed and scaled, the SQP gradient method is found to be far more consistent, and deliver higher quality solutions, without non intuitive tuning. Future work may seek to better address these challenges by improving the numerical method, and possibly by adopting a hybrid gradient/stochastic solver.

There are innumerable considerations related to this methodology, and optimal Coulomb reconfigurations in general, but the following elicit primary significance for being addressed in further investigations. Additional optimal 2-craft reconfiguration results, involving different final states and more segments would provide further evidence of method robustness. And some important permutations to consider include free segment start times, alternate or higher order control approximations, and the enforcement of charge continuity. Furthermore, inequality constraints that account for thruster plume impingement and minimum separation distance should eventually be appended to the optimization formulation. Invariant manifold theory should be extended to other known static Coulomb formations, and even the periodic Coulomb formations derived in Chapter 3. Those motions could then be analyzed to determine which reconfigurations may be suited to the application of the general method presented here, and in fact such a study is begun for 3-craft equilibria in Section 5.5.4.

Lastly, the 2-craft reconfigurations presented here should be targeted in a higher fidelity dynamical model, that involves parameter uncertainty (e.g. variable λ_d) and primary perturbations (i.e. solar radiation pressure). The initial such continuation step is taken in Section 6.3.3, where the manifolds generated in this Chapter are propagated in an inertial frame, with the inclusion of primary perturbations. Because the transfers mostly occur along the manifolds, ascertaining the accuracy of these uncontrolled motions is principal to characterizing accuracy of the controlled reconfigurations, and thereby how well they lend themselves to a continuation method.

The research in this Chapter represents the first example of utilizing near-heteroclinic orbits in a relative spacecraft motion problem, where Coulomb forces give rise to the chaotic dynamics necessary for such delicate trajectories. Therefore, the techniques and method developed here provide a preliminary assessment for how this type of theory may be applied, and extended beyond its typical realm of low-energy transfers in multi-body gravity fields. The motivation for doing this was to realize the shape change ability of Coulomb formations, without sacrificing the benefits of electrostatic force control, in lieu of inertial thrusting. And although the results may be improved during future revisions to its formulation, the methodology indeed succeeds in its aim of delivering 2-craft equilibria transfers, at demonstrably reduced ΔV cost.

Chapter 5

Three-Craft Collinear Static Equilibria

5.1 Chapter Summary

Berryman and Schaub demonstrate the existence of 3-craft collinear Coulomb formations, where constant charges yield static equilibria solutions with the craft aligned along a Hill axis, although charge values to produce a given shape are not unique.^{17,32} The conditions for equilibria in Ref. 17, however, are not sufficient because they do not explicitly ensure non imaginary charge values, nor do they account for plasma shielding. Therefore in Section 5.2, necessary and sufficient conditions are derived for these 3-craft collinear configurations, with the inclusion of shielding. The sufficiency conditions provide bounds on the charge products \tilde{Q}_{ij}^* which ensure non imaginary solutions, and these bounds result in discrete equilibria regions (or cases).^{43,45}

Since there are infinite equilibrium charge solutions, a constrained nonlinear programming problem is derived in Section 5.2.2 that minimizes the largest potential ϕ on any craft, for a given shape. Some numerically optimal results are generated, and show that a conservative power requirement of < 10 watts can enable formations with up to a 100 meter separation.

In Section 5.5, stability properties for each equilibria region are explored numerically, and all cases are found to be dynamically unstable over wide parameter ranges. Furthermore, invariant manifold theory is applied to the 3-craft collinear equi-

libria, for the first time in Section 5.5.3. The numerically generated manifolds help illustrate and verify certain stability properties. The existence of near-heteroclinic orbits are also considered for this class of 3-craft Coulomb formation, as was done to generate IG trajectories for 2-craft static equilibria reconfigurations in Section 4.6. The goal being the identification of 3-craft reconfiguration scenarios that lend themselves to an extension of the methodology outlined in Section 4.5, for achieving minimal ΔV shape changes.

Recognizing advantageous eigenspace properties is particularly important for reducing station-keeping fuel usage, since the nearly propellantless Coulomb forces have limited reach and controllability.²¹ Limited controllability therefore motivates a thorough investigation of the system stability properties, in order to best utilize charge control for feedback stabilization. Hence, modal instability properties of the system eigendecompositions are utilized in Section 5.3 to aid the design of a feedback stabilization strategy. This is a similar approach to that of Natarajan and Schaub in deriving a charge feedback control to asymptotically remove in-plane perturbations for the Radial 2-craft Hill frame equilibria.³⁵ Linearized dynamical systems associated with these 3-craft equilibria are derived, and small perturbations normal to the reference orbit plane are shown analytically to be bounded for Radial and Along-Track aligned cases. These configurations are also demonstrated to have complete Coulomb force controllability within the \hat{e}_R - \hat{e}_T plane, such that those perturbations may be asymptotically removed using only charge control (no inertial thrust).

Section 5.4 verifies the derived charge feedback law in simulation, and although the systems are not fully stabilizable, any uncontrolled \hat{e}_N axis perturbations remain bounded. These Radial configuration properties are consistent with those

demonstrated by Natarajan and Schaub³⁵ for the analogous 2-craft Radial equilibrium. In comparison, the 2- and 3-craft Along-Track equilibria both exhibit marginal out-of-plane stability, but only the 3-craft configuration has complete Coulomb force controllability within the $\hat{e}_R\text{-}\hat{e}_T$ plane.²⁴

5.2 Three-Craft Collinear Equilibria

Berryman and Schaub¹⁷ show that these equilibrium exist only when the vehicles are aligned along a Hill axis, and provide necessary existence conditions, but without including plasma shielding. These conditions do not explicitly ensure real-valued charges \tilde{q}_i^* , but it is shown that real \tilde{q}_i^* solutions do exist, for each Hill axis alignment and all separation distances. Since each craft is located along a single Hill axis, a concise notation is adopted to describe these equilibria,¹⁷ in which d_i denotes a reference radial magnitude along that line ($d_i = |r_i^*|$), and $d_{ij} = r_{ij}^*$. Since the craft numbering is arbitrary, it is assumed that $r_1^* < 0$ and $r_3^* > 0$, as illustrated in Figure 5.1. Next all derivatives in the Eqs. (2.23a)-(2.23b) of motion are set to zero,

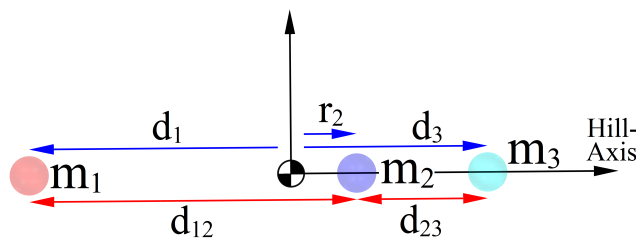


Figure 5.1: Three-Craft Collinear Equilibrium Geometry and Notation

and the Figure 5.1 simplified notation and assumed sign convention for r_1^* and r_3^* are enforced. This results in Eqs. (5.1a)-(5.1b), scalar expressions which define all 3-craft collinear equilibria, where the term a_d differentiates between linearized gravitational terms of Radial ($a_d = -3$), Along-Track ($a_d = 0$), and Orbit-Normal ($a_d = 1$) aligned

formations.

$$a_d m_1 d_1 - c_{13} [d_1 + d_3] - c_{12} \left[M_{r2} d_1 + \frac{m_3}{m_2} d_3 \right] = 0 \quad (5.1a)$$

$$-a_d m_3 d_3 + c_{13} [d_3 + d_1] + c_{23} \left[M_{r3} d_3 + \frac{m_1}{m_2} d_1 \right] = 0 \quad (5.1b)$$

The equilibria must therefore satisfy these two conditions, but recalling that $c_{ij} = \tilde{Q}_{ij}^* \Psi(d_{13})$ there are five unknowns: \tilde{Q}_{12}^* , \tilde{Q}_{13}^* , \tilde{Q}_{23}^* , d_1 , and d_3 (r_2^* solved explicitly from Eq. (2.8)). This underdetermined system can be handled¹⁷ by specifying the geometry, via d_1 and d_3 , and also specifying the charge product \tilde{Q}_{13}^* . Necessary \tilde{Q}_{12}^* and \tilde{Q}_{23}^* values may then be solved explicitly from Eqs. (5.1a)-(5.1b).

5.2.1 Necessary and Sufficient Conditions with Shielding

The bracketed terms in Eqs. (5.1a)-(5.1b) are simply the separation distances d_{ij} . Therefore, substituting the d_{ij} terms into Eqs. (5.1a)-(5.1b) and solving for \tilde{Q}_{12}^* and \tilde{Q}_{23}^* , results in Eqs. (5.2a)-(5.2b).

$$\tilde{Q}_{12}^* = \frac{1}{\Psi(d_{12}) d_{12}} \left[a_d d_1 m_1 - \Psi(d_{13}) d_{13} \tilde{Q}_{13}^* \right] \quad (5.2a)$$

$$\tilde{Q}_{23}^* = \frac{1}{\Psi(d_{23}) d_{23}} \left[a_d d_3 m_3 - \Psi(d_{13}) d_{13} \tilde{Q}_{13}^* \right] \quad (5.2b)$$

These are the necessary charge product conditions for 3-craft collinear static equilibria. And scaled individual craft charges \tilde{q}_i^* are computed according to the Eq. (2.24) convention, outlined in Section 2.5.

An examination of Eqs. (5.2a)-(5.2b) and Eq. (2.24) reveals that not every combination of d_1 , d_3 , and \tilde{Q}_{13}^* will yield non complex individual charge values. In fact, the \tilde{q}_i^* are real-valued if and only if the triple product of the three charge products is non negative. Utilizing this fact enables sufficient equilibria conditions to be defined,

which amounts entirely to bounding \tilde{Q}_{13}^* for a given geometry (values of a_d , d_1 , and d_3). Bounds on \tilde{Q}_{13}^* , which are sufficient to ensure non imaginary \tilde{q}_i^* , thereby yield discrete regions in the design space, outside of which equilibria cannot exist. These regions are presented on a case by case basis, utilizing the c_{ij} notation.

1. **Along-Track:** $\tilde{Q}_{13}^* \geq 0$

2. **Orbit-Normal**

- **Case A:** $\tilde{Q}_{13}^* \geq 0$, $c_{13} \leq m_1 d_1 / d_{13}$, $c_{13} \leq m_3 d_3 / d_{13}$
- **Case B:** $\tilde{Q}_{13}^* > 0$, $c_{13} \geq m_1 d_1 / d_{13}$, $c_{13} \geq m_3 d_3 / d_{13}$

3. **Radial**

- **Case A:** $\tilde{Q}_{13}^* \geq 0$
- **Case B:** $\tilde{Q}_{13}^* < 0$, $|c_{13}| \leq 3m_1 d_1 / d_{13}$, $|c_{13}| \geq 3m_3 d_3 / d_{13}$ ($m_1 d_1 \geq m_3 d_3$)
- **Case C:** $\tilde{Q}_{13}^* < 0$, $|c_{13}| \geq 3m_1 d_1 / d_{13}$, $|c_{13}| \leq 3m_3 d_3 / d_{13}$ ($m_1 d_1 \leq m_3 d_3$)

Trivial cases admitted by Eqs. (5.2a)-(5.2b), where $\tilde{Q}_{12}^* = \tilde{Q}_{23}^* = \tilde{q}_2^* = 0$ ($d_2 = 0$), are included in this categorization and given explicitly by Eq. (5.3).

$$\tilde{Q}_{13}^* = \frac{a_d m_1 d_1}{\Psi(d_{13}) d_{13}} = \frac{a_d m_3 d_3}{\Psi(d_{13}) d_{13}} \quad d_1 = \frac{m_3 d_3}{m_1} \quad (5.3)$$

These are trivial because they reduce to the 2-craft Hill frame configurations (along each axis), previously defined in Section 4.3, and whose stability properties are examined in that section, and by various authors.^{22,35,42} The only technical difference from the 2-craft equilibria, is the addition of a non interacting craft (craft 2), which is located at the CM (origin).

The free charge product \tilde{Q}_{13}^* is thus bounded from above or below (or both above and below for Radial cases B-C). Also, the sign and magnitude of \tilde{Q}_{13}^* explicitly governs the sign and magnitude for all other charge products. This product thereby designates the net force on each craft, as well as whether each of the three forces is repulsive or attractive. For example, Radial case B invokes an attractive force between crafts 1 and 2 and a repulsive force between crafts 2 and 3, whereas Radial case C has opposite signs on those forces. This division is due only to the relative position and mass of crafts 1 and 3. Furthermore, each of these discrete equilibria regions, or cases, bears distinct eigenspaces and varied unstable and stable manifold structures, as defined generally in Section 2.6.2. Specifically, the dimensionality of the unstable and stable eigenspaces (N_u and N_s) varies between cases, along with what Cartesian subspace contains the corresponding eigenvectors.

5.2.2 Computing Optimal Charges to Achieve a Desired Shape

Since an infinite number of individual charges can produce the equilibria cases described in Section 5.2.1, computing ideal or optimal values is of interest. The L_∞ norm of the three \tilde{q}_i^* , is a sensible performance measure to use since that minimizes the largest reference $|\phi|$ on any craft. Because $|\phi|$ is proportional to the power required P_{out} , via Eq. (2.3) (ignoring the $I_{\text{out}}(\phi)$ nonlinear dependence), a minimum L_∞ measure best ensures the entire system can use a charge control device, with the lowest possible P_{out} . In contrast, an L_1 or L_2 norm would result in a larger (or equal) maximum $|\phi|$, and therefore an individual craft would likely require more power. The remaining vehicles would then have to accommodate this, with the practical assumption that identical control hardware is used.

The determination of a specified equilibrium configuration, with minimum L_∞

norm of the charges, is formulated as a constrained nonlinear programming problem, as described in Section 2.7. To handle the L_∞ norm function numerically, the cost function is set equal to a dummy variable α , with α constrained greater or equal to all $|\tilde{q}_i^*|$. The optimization problem is written explicitly in Eq. (5.4), with \mathbf{C} corresponding to Eqs. (5.2a)-(5.2b), and \mathbf{D} derived from the case specific sufficient conditions described in Section 5.2.1, and also $|\tilde{q}_i^*| \leq \alpha$, $i = 1, 2, 3$.

$$\begin{aligned} \text{minimize} \quad & J(\mathbf{X}_p) = \alpha \quad \mathbf{X}_p = [\tilde{q}_1^* \ \tilde{q}_2^* \ \tilde{q}_3^* \ \alpha]^T \\ \text{subject to} \quad & \mathbf{C}(\mathbf{X}_p) = 0 \quad \mathbf{D}(\mathbf{X}_p) \leq 0 \end{aligned} \tag{5.4}$$

The Section 5.2.1 necessary and sufficient conditions, provide for the determination of a feasible \mathbf{X}_p initial guess. Numerically, this optimization problem is well behaved and easily solved. Some optimal results, obtained using MATLAB's *fmincon* as the numerical solver, are presented in Table 5.1. Where the power is computed by Eq. (2.4),

Table 5.1: Minimum Power Results for Three-Craft Collinear Cases

Axis	Case	d_1 , m	d_3 , m	$ \tilde{q}^* _{\max}$, μC	Power, W
Orbit-Normal	A	30	25	1.72	1.24
Orbit-Normal	A	40	60	12.29	8.83
Orbit-Normal	B	30	25	3.52	2.54
Orbit-Normal	B	40	60	8.27	5.95
Radial	A	30	25	3.33	2.39
Radial	A	40	60	10.59	7.61
Radial	B	30	25	5.32	3.82
Radial	B	30	18	4.64	3.34
Radial	C	40	60	13.34	9.60

using a potential (in Volts) found by substituting $|\tilde{q}^*|_{\max}$ into Eq. (2.2). Along-Track results are omitted from Table 5.1, because it is clear from Eqs. (5.2a)-(5.2b) that the optimum occurs when all charges are zero (trivial case).

The Table 5.1 results show that with optimal charge selection, formations of $|d_1 - d_3| \leq 100$ m can be produced with < 10 watts of power. Furthermore, these power requirements should be considered very high estimates, because of the use of a conservative plasma shielding model, and since the largest possible operating current is being used in the calculations. Other observations include nearly equal power requirements between Radial and Orbit-Normal configurations, for similar $|d_1 - d_3|$ (and both configurations exhibit increased power in proportion to $|d_1 - d_3|$).

5.3 Stabilizability of Radial and Along-Track Cases

It is apparent from the Eqs. (2.21a)-(2.21b) dynamics, that \hat{e}_N motions decouple from the \hat{e}_R - \hat{e}_T planar dynamics, to 1st order. Orbit-Normal configurations have \hat{e}_N directed Coulomb forces, and therefore are incapable of \hat{e}_R - \hat{e}_T planar perturbation control, in the linearized sense. For this reason, Orbit-Normal equilibria are omitted in what follows. Although Coulomb forces do not provide full system controllability,²¹ the possibility for Radial and Along-Track equilibria to be linearly stabilizable using only charge control (no inertial thrust), is addressed in this section. The 3-craft linear time invariant (LTI) dynamics, with charge control, are written in the Eq. (5.5) state space form, where \mathbf{A} is defined in Eqs. (2.34a)-(2.34b).

$$\delta \mathbf{X}' = \mathbf{A} \delta \mathbf{X} + \mathbf{B} \delta \mathbf{u} \quad \delta \mathbf{X} = \begin{bmatrix} \delta \mathbf{r}_1 \\ \delta \mathbf{r}_3 \\ \mathbf{v}_1 \\ \mathbf{v}_3 \end{bmatrix}_{12 \times 1} \quad \delta \mathbf{u} = \begin{bmatrix} \delta \tilde{q}_1 / |\tilde{q}_1^*| \\ \delta \tilde{q}_2 / |\tilde{q}_2^*| \\ \delta \tilde{q}_3 / |\tilde{q}_3^*| \end{bmatrix}_{3 \times 1} \quad (5.5)$$

The $\delta \tilde{q}_i$ are variations in craft i net charge from the \tilde{q}_i^* equilibrium values, and the $|\tilde{q}_i^*|$ terms in the control vector $\delta \mathbf{u}$ are used as a scaling for \mathbf{B} matrix terms, such that they are nearly of equal order of magnitude as those in \mathbf{A} . With this scaling the

linearized system input matrix is given by Eq. (5.6).

$$\mathbf{B} = \left[\begin{array}{ccc|c} \mathbf{0}_{6 \times 3} & & & \\ \frac{c_{12}}{m_1} |\tilde{q}_1| \tilde{q}_2 \mathbf{r}_{12} + \frac{c_{13}}{m_1} |\tilde{q}_1| \tilde{q}_3 \mathbf{r}_{13} & \frac{c_{12}}{m_1} |\tilde{q}_2| \tilde{q}_1 \mathbf{r}_{12} & \frac{c_{13}}{m_1} |\tilde{q}_3| \tilde{q}_1 \mathbf{r}_{13} & \\ \frac{-c_{13}}{m_3} |\tilde{q}_1| \tilde{q}_3 \mathbf{r}_{13} & \frac{-c_{23}}{m_3} |\tilde{q}_2| \tilde{q}_3 \mathbf{r}_{23} & \frac{-c_{13}}{m_3} |\tilde{q}_3| \tilde{q}_1 \mathbf{r}_{13} - \frac{c_{23}}{m_3} |\tilde{q}_3| \tilde{q}_2 \mathbf{r}_{23} & \end{array} \right] \Big|_{(\mathbf{X}^*, \mathbf{u}^*)} \quad (5.6)$$

Because the uncontrollable \hat{e}_N axis perturbations decouple, a simple canonical transformation is used to rewrite Eq. (5.5) in the form of Eqs. (5.7a)-(5.7c). Where $\delta \mathbf{X}_c$ is the vector of controllable perturbations, and $\delta \mathbf{X}_{uc}$ is the vector of uncontrollable perturbations.

$$\begin{bmatrix} \delta \mathbf{X}'_c \\ \delta \mathbf{X}'_{uc} \end{bmatrix} = \left[\begin{array}{c|c} \mathbf{A}_c & \mathbf{0} \\ \mathbf{0} & \mathbf{A}_{uc} \end{array} \right] \begin{bmatrix} \delta \mathbf{X}_c \\ \delta \mathbf{X}_{uc} \end{bmatrix} + \begin{bmatrix} \mathbf{B}_c \\ \mathbf{0} \end{bmatrix} \delta \mathbf{u} \quad (5.7a)$$

$$\delta \mathbf{X}_c = \begin{bmatrix} \delta x_1 & \delta y_1 & \delta x_3 & \delta y_3 & v_{x1} & v_{y1} & v_{x3} & v_{y3} \end{bmatrix}^T_{8 \times 1} \quad (5.7b)$$

$$\delta \mathbf{X}_{uc} = \begin{bmatrix} \delta z_1 & \delta z_3 & v_{z1} & v_{z3} \end{bmatrix}^T_{4 \times 1} \quad (5.7c)$$

For this transformed LTI representation, a charge feedback control law can stabilize the Radial and Along-Track configurations, in accordance with the following.

Theorem 5.3.1. *An LTI system is stabilizable if and only if all unstable states are controllable.⁶⁶ Specific to the system in Eqs. (5.7a)-(5.7c), this requires the following postulates are true:*

1. *The pair $(\mathbf{A}_c, \mathbf{B}_c)$ is controllable.*
2. *The matrix \mathbf{A}_{uc} is Hurwitz.*

Also a weaker theorem for controlled uniform stability, specific to LTI systems with decoupled $\delta \mathbf{X}_{uc}$ such as that in Eqs. (5.7a)-(5.7c), is as follows.

Theorem 5.3.2. *A controlled LTI system can exhibit uniformly stable $\delta\mathbf{X}_{uc}$ modes and asymptotically stable $\delta\mathbf{X}_c$ modes, if the following conditions are true:*

1. *The pair $(\mathbf{A}_c, \mathbf{B}_c)$ is controllable.*
2. *The matrix \mathbf{A}_{uc} is a uniformly stable matrix (not necessarily Hurwitz).*

Therefore, the aim of this section is to determine the validity of Theorems 5.3.1-5.3.2 for Along-Track and Radial equilibria, to ascertain under what conditions these can be stabilized (made uniformly stable) with only charge control. The analysis is broken into two parts, the first to assess Coulomb force controllability within the reduced dynamics of the reference orbit plane, and the second concerning stability of out-of-plane perturbations. Of course, any such conclusions do not necessarily hold in the nonlinear system, where higher order dynamical terms, and large perturbations, could cause loss of controlled stability. Lastly, based on literature review, these configurations may be nearly uncontrollable (in the \hat{e}_R - \hat{e}_T plane) and/or highly sensitive, therefore some effort is devoted to computing a relative measure of controllability.^{22,29,42}

5.3.1 Radial and Along-Track In-Plane Controllability

To assess in-plane controllability, the $(\mathbf{A}_c, \mathbf{B}_c)$ quadrants of the \mathbf{A} and \mathbf{B} matrices, defined in Eqs. (2.34a)-(2.35d) and Eq. (5.6), are evaluated for both equilibria types. To simplify the evaluations, the Eq. (5.8) distance ratio parameters are introduced, and these ratios satisfy Eq. (5.9).

$$\bar{d}_1 = \frac{d_{13}}{d_{12}} \quad \bar{d}_2 = \frac{d_{13}}{d_{23}} \quad \bar{d}_3 = \frac{d_1}{d_{12}} \quad \bar{d}_4 = \frac{d_3}{d_{23}} \quad (5.8)$$

$$\bar{d}_1\bar{d}_2 = (\bar{d}_1 + \bar{d}_2) \quad \bar{d}_1 > 1 \quad \bar{d}_2 > 1 \quad \bar{d}_3 > 0 \quad \bar{d}_4 > 0 \quad (5.9)$$

Also relations between the c_{ij} coefficients are defined by Eq. (5.10) for Along-Track equilibria, and by Eq. (5.11) for Radial equilibria, in terms of the Eq. (5.8) ratios.

$$c_{12} = -c_{13}\bar{d}_1 \quad c_{23} = -c_{13}\bar{d}_2 \quad (5.10)$$

$$c_{12} = -c_{13}\bar{d}_1 - 3m_1\bar{d}_3 \quad c_{23} = -c_{13}\bar{d}_2 - 3m_3\bar{d}_4 \quad (5.11)$$

Equation (5.12) then defines the decoupled linear system governing in-plane perturbations, with the \mathbf{A}_c matrix written in block form, and \mathbf{H}_c sub-matrix specific to the axis of alignment.

$$\delta\mathbf{X}'_c = \mathbf{A}_c\delta\mathbf{X}_c + \mathbf{B}_c\delta\mathbf{u} \quad \mathbf{A}_c = \left[\begin{array}{c|c} \mathbf{0} & \mathbf{I} \\ \hline \mathbf{H}_c & \mathbf{G}_c \end{array} \right]_{8 \times 8} \quad \mathbf{G}_c = \begin{bmatrix} 0 & 2 & 0 & 0 \\ -2 & 0 & 0 & 0 \\ 0 & 0 & 0 & 2 \\ 0 & 0 & -2 & 0 \end{bmatrix} \quad (5.12)$$

The matrix \mathbf{B}_c is also axis specific, and is evaluated along with \mathbf{H}_c in Eqs. (5.13a)-(5.13b) and Eqs. (5.14a)-(5.14b), using the c_{ij} and \bar{d}_i notation. Along-Track configurations are given explicitly by Eqs. (5.13a)-(5.13b), for the special case of equal mass ($m_1 = m_2 = m_3 = m$) and negligible plasma shielding ($\lambda_d \rightarrow \infty$).

$$\mathbf{H}_c = \begin{bmatrix} 3 + \frac{c_{13}(1-2\bar{d}_1)}{m} & 0 & \frac{-c_{13}(\bar{d}_1+1)}{m} & 0 \\ 0 & \frac{c_{13}(4\bar{d}_1-2)}{m} & 0 & \frac{2c_{13}(\bar{d}_1+1)}{m} \\ \frac{-c_{13}(\bar{d}_2+1)}{m} & 0 & 3 + \frac{c_{13}(1-2\bar{d}_2)}{m} & 0 \\ 0 & \frac{2c_{13}(\bar{d}_2+1)}{m} & 0 & \frac{c_{13}(4\bar{d}_2-2)}{m} \end{bmatrix} \quad (5.13a)$$

$$\mathbf{B}_c = \frac{d_{13}c_{13}}{m} \begin{bmatrix} \mathbf{0}_{5 \times 3} \\ 0 & -1 & -1 \\ 0 & 0 & 0 \\ 1 & 1 & 0 \\ 0 & 0 & 0 \end{bmatrix} \quad (5.13b)$$

Equations (5.14a)-(5.14b) correspond to Radial configurations, again for the special case of equal mass and negligible plasma shielding ($\lambda_d \rightarrow \infty$).

$$\mathbf{H}_c = \begin{bmatrix} 3 + \frac{c_{13}(4\bar{d}_1 - 2)}{m} + 12\bar{d}_3 & 0 & \frac{2c_{13}(\bar{d}_1 + 1)}{m} + 6\bar{d}_3 & 0 \\ 0 & \frac{c_{13}(1 - 2\bar{d}_1)}{m} - 6\bar{d}_3 & 0 & \frac{-c_{13}(\bar{d}_1 + 1)}{m} - 3\bar{d}_3 \\ \frac{2c_{13}(\bar{d}_2 + 1)}{m} + 6\bar{d}_4 & 0 & 3 + \frac{c_{13}(4\bar{d}_2 - 2)}{m} + 12\bar{d}_4 & 0 \\ 0 & \frac{-c_{13}(1 + 2\bar{d}_2)}{m} - 3\bar{d}_4 & 0 & \frac{c_{13}(1 - 2\bar{d}_2)}{m} - 6\bar{d}_4 \end{bmatrix} \quad (5.14a)$$

$$\mathbf{B}_c = \begin{bmatrix} \mathbf{0}_{4 \times 3} \\ 3d_1 & \frac{-c_{13}d_{13}}{m} - 3d_1 & \frac{-c_{13}d_{13}}{m} \\ 0 & 0 & 0 \\ \frac{c_{13}d_{13}}{m} & \frac{c_{13}d_{13}}{m} + 3d_3 & -3d_3 \\ 0 & 0 & 0 \end{bmatrix} \quad (5.14b)$$

Controllability of the $(\mathbf{A}_c, \mathbf{B}_c)$ pairs, with sub-matrices defined by Eqs. (5.13a)-(5.13b) for Along-Track and Eqs. (5.14a)-(5.14a) for Radial, is assessed via the controllability matrix \mathbf{Q}_c . The \mathbf{Q}_c matrix is written in the Eq. (5.15) block matrix form, where the $\mathbf{A}_c^2, \dots, \mathbf{A}_c^7$ terms denote matrix exponentials.

$$\mathbf{Q}_c = [\mathbf{B}_c \mid \mathbf{A}_c \mathbf{B}_c \mid \mathbf{A}_c^2 \mathbf{B}_c \mid \mathbf{A}_c^3 \mathbf{B}_c \mid \mathbf{A}_c^4 \mathbf{B}_c \mid \mathbf{A}_c^5 \mathbf{B}_c \mid \mathbf{A}_c^6 \mathbf{B}_c \mid \mathbf{A}_c^7 \mathbf{B}_c] \quad (5.15)$$

The linearized systems are fully controllable (using only Coulomb forces) in the reference orbit plane, if and only if \mathbf{Q}_c is full rank (i.e. $|\mathbf{Q}_c| \neq 0$). It is determined numerically that both configuration cases satisfy this condition, not only for $m_1 = m_2 = m_3 = m$ and $\lambda_d \rightarrow \infty$ special case, but also more generally. Both Along-Track and Radial configurations have Coulomb force controllability in the \hat{e}_R - \hat{e}_T plane, and therefore satisfy the first condition of Theorem 5.3.1 and Theorem 5.3.2. This is a direct consequence of the coupling between δx_i and δy_i terms⁶⁷ in Eqs. (2.34a)-(2.34b), and an analogous controllability result is demonstrated for the Radial 2-craft configuration.³⁵

5.3.2 Radial and Along-Track Uncontrolled Modal Stability

Here the \mathbf{A}_{uc} quadrant of the \mathbf{A} matrix defined in Eqs. (2.34a)-(2.35d) is evaluated for Radial and Along-Track equilibrium. The decoupled linear system governing uncontrollable perturbations $\delta\mathbf{X}_{uc}$, is given symbolically by Eqs. (5.16a)-(5.16b).

$$\delta\mathbf{X}'_{uc} = \mathbf{A}_{uc} \delta\mathbf{X}_{uc} = \left[\begin{array}{c|c} \mathbf{0} & \mathbf{I} \\ \hline \mathbf{A}_{zz} & \mathbf{0} \end{array} \right] \delta\mathbf{X}_{uc} \quad (5.16a)$$

$$\mathbf{A}_{zz} = \begin{bmatrix} \left(\frac{c_{12} M_{r2}}{m_1} + \frac{c_{13}}{m_1} - 1 \right) & \left(\frac{c_{12} m_3}{m_1 m_2} - \frac{c_{13}}{m_1} \right) \\ \left(\frac{c_{23} m_1}{m_2 m_3} - \frac{c_{13}}{m_3} \right) & \left(\frac{c_{23} M_{r3}}{m_3} + \frac{c_{13}}{m_3} - 1 \right) \end{bmatrix} \quad (5.16b)$$

The \mathbf{A}_{uc} matrix is that of a 2nd order coupled and undamped ODE system, and therefore \mathbf{A}_{uc} cannot be Hurwitz. Radial and Along-Track configurations can never achieve stabilizability with charge control alone according to Theorem 5.3.1; however, uniform stability is achieved in accordance with Theorem 5.3.2 so long as \mathbf{A}_{uc} has eigenvalues with non positive real parts. For the Eqs. (5.16a)-(5.16b) form, this is true if the following conditions are met.

1. $\text{tr}(\mathbf{A}_{zz}) < 0$
2. $|\mathbf{A}_{zz}| \geq 0$

These conditional checks on \mathbf{A}_{zz} are evaluated explicitly in Eqs. (5.17)-(5.18).

$$\text{tr}(\mathbf{A}_{zz}) = c_{13} \left(\frac{1}{m_1} + \frac{1}{m_3} \right) + c_{12} \left(\frac{M_{r2}}{m_1} \right) + c_{23} \left(\frac{M_{r3}}{m_3} \right) - 2 \quad (5.17)$$

$$|\mathbf{A}_{zz}| = \left[c_{12} \frac{M_{r2}}{m_1} + \frac{c_{13}}{m_1} - 1 \right] \left[c_{23} \frac{M_{r3}}{m_3} + \frac{c_{13}}{m_3} - 1 \right] - \left[c_{12} \frac{m_3}{m_1 m_2} - \frac{c_{13}}{m_1} \right] \left[c_{23} \frac{m_1}{m_2 m_3} - \frac{c_{13}}{m_3} \right] \quad (5.18)$$

5.3.2.1 Along-Track

Equation (5.19) is the result of substituting Eq. (5.10) relations into the Eq. (5.17) condition.

$$\text{tr}(\mathbf{A}_{zz}) = \frac{c_{13}}{m_1} (1 - M_{r2}\bar{d}_1) + \frac{c_{13}}{m_3} (1 - M_{r3}\bar{d}_2) - 2 \quad (5.19)$$

Since $\bar{d}_1 > 1$ and $\bar{d}_2 > 1$ from Eq. (5.9), and so too are M_{r2} and M_{r3} , it is concluded that all terms in Eq. (5.19) are negative. Therefore, Along-Track configurations have $\text{tr}(\mathbf{A}_{zz}) < 0$, satisfying the first requirement for non positive eigenvalues of \mathbf{A}_{uc} .

Equation (5.18) is evaluated similarly, but the algebra is more involved. The expression has c_{13}^2 terms, c_{13} terms, and non c_{13} terms; however, all c_{13}^2 terms cancel. After cancellation and some rearranging the determinant is given in Eq. (5.20).

$$|\mathbf{A}_{zz}| = c_{13} \left(M_{r2}\bar{d}_1 + M_{r3}\bar{d}_2 - \frac{1}{m_1} - \frac{1}{m_3} \right) + 1 \quad (5.20)$$

With certainty $|\mathbf{A}_{zz}| > 0$ so long as $m_1 > 1$ and $m_3 > 1$, which is reasonable since these have units of mass (in kg). Based on the Eq. (5.19) and Eq. (5.18) evaluations, it is concluded that \mathbf{A}_{uc} has non positive eigenvalues for Along-Track equilibria, and therefore will exhibit bounded out-of-plane motion, to 1st order. The controlled linearized systems about Along-Track equilibria may then be uniformly stable by Theorem 5.3.2.

5.3.2.2 Radial Case A

For the Case A equilibria (corresponding to $\tilde{Q}_{13} > 0$ and $c_{13} > 0$), the substitution of Eq. (5.11) into Eq. (5.17) yields Eq. (5.21).

$$\text{tr}(\mathbf{A}_{zz}) = \frac{c_{13}}{m_1} (1 - M_{r2}\bar{d}_1) + \frac{c_{13}}{m_3} (1 - M_{r3}\bar{d}_2) - 2 - 3M_{r2}\bar{d}_3 - 3M_{r3}\bar{d}_4 \quad (5.21)$$

This is identical to Eq. (5.19), but with the addition of the \bar{d}_3 and \bar{d}_4 terms. And since \bar{d}_3 and \bar{d}_4 are positive (and $c_{13} > 0$), all terms in Eq. (5.21) are negative. Equation (5.18) is evaluated similarly, and as in the Along-Track case all c_{13}^2 terms cancel. After some algebraic effort, the determinant is given by Eq. (5.22).

$$|\mathbf{A}_{zz}| = 1 + c_{13} \left(M_{r2}\bar{d}_1 + M_{r3}\bar{d}_2 - \frac{1}{m_1} - \frac{1}{m_3} \right) + 9M_{r2}M_{r3}\bar{d}_3\bar{d}_4 \\ + c_{13} \left[\frac{(1+3M_{r2}\bar{d}_3)(M_{r3}\bar{d}_2-1)}{m_3} + \frac{(1+3M_{r3}\bar{d}_4)(M_{r2}\bar{d}_1-1)}{m_1} \right] \quad (5.22)$$

The same positive terms as found in Eq. (5.18) are present, but there are also some additional terms. Of these, the term not involving c_{13} is obviously positive, and so too are the $M_{r2}\bar{d}_1 - 1$ and $M_{r3}\bar{d}_2 - 1$ terms. Then with $c_{13} > 0$, $\bar{d}_3 > 0$, and $\bar{d}_4 > 0$, all terms are positive so long as $m_1 > 1$ kg and $m_3 > 1$ kg. Therefore, controlled linearized systems about Radial Case A equilibria may be uniformly stable by Theorem 5.3.2.

5.3.2.3 Radial Cases B and C

The following analysis is performed for Radial Case B, but applies similarly to Case C. It is demonstrated here that positive \mathbf{A}_{uc} eigenvalue(s) can arise, resulting in unbounded out-of-plane perturbations (\hat{e}_N axis unstable modes). The $\text{tr}(\mathbf{A}_{zz})$ for these cases is the same as that derived in Eq. (5.21), but now $\tilde{Q}_{13} < 0$ and $c_{13} < 0$. If the Eq. (5.23) inequality is true, then $\text{tr}(\mathbf{A}_{zz}) > 0$ and at least one eigenvalue of \mathbf{A}_{uc} is positive, where again the bounds on \bar{d}_i and M_{r_i} ratios have been applied.

$$\frac{|c_{13}|}{m_1} (M_{r2}\bar{d}_1 - 1) + \frac{|c_{13}|}{m_3} (M_{r3}\bar{d}_2 - 1) - 3 (M_{r2}\bar{d}_3 + M_{r3}\bar{d}_4) > 2 \quad (5.23)$$

As an example, assume equal mass craft ($m_1 = m_2 = m_3 = m$) and a $|\tilde{Q}_{13}|$ at the maximum bound defined in Section 5.2.1. Evaluating Eq. (5.23) for this example

($|c_{13}| = 3md_1r_{13}$) results in Eq. (5.24).

$$d_1 d_{13} (\bar{d}_1 + \bar{d}_2 - 1) - \bar{d}_3 - \bar{d}_4 > \frac{1}{3} \quad (5.24)$$

And Eq. (5.24) is true for the parameter values $d_1 = 5$, $d_3 = 5$, and $d_2 = 0$. In fact, in this example the left side of the inequality is equal to 148.0. This shows by example that out-of-plane instability can occur; however, it does not always. Whether an eigenvalue(s) of \mathbf{A}_{uc} is positive depends on \tilde{Q}_{13} , d_1 , d_3 , and spacecraft masses. Therefore, whether Radial cases B and C can be controlled to exhibit linear uniform stability is parameter dependent, and this modal bifurcation is explored numerically in Section 5.5.

5.3.3 Sensitivity of In-Plane Controllability

All Radial equilibria cases have full charge controllability in the reference orbit plane, but in cases B/C the boundedness of uncontrollable out-of-plane perturbations is not necessarily guaranteed. Natarajan shows that there exist no real-valued gains which can stabilize 2-craft Along-Track Coulomb formations in the reference orbit plane, thereby necessitating some inertial thrusting.²⁴ In contrast, the current investigation shows that 3-craft Along-Track configurations are controllable in the reference orbit plane, with bounded perturbations along the \hat{e}_N axis. However, these equilibria are very nearly uncontrollable numerically (\mathbf{Q}_c tends to have poor condition number), and therefore feedback stabilization is highly sensitive.

An assessment of near uncontrollability is made by computing a distance measure from the true system to an uncontrollable state space, using the method of Boley and Lu.⁶⁸ The distance measure Σ , written explicitly in Eq. (5.25), describes the minimum perturbation to the original system, for it to become uncontrollable. Where η_n

is the smallest magnitude singular value of \mathbf{Q}_c (η_{n-1} the next smallest) and \mathbf{A}_F is the companion matrix to \mathbf{A} .

$$\Sigma(\mathbf{A}_c, \mathbf{B}_c) \leq \left(1 + \frac{\|\mathbf{A}_F\|}{\eta_{n-1}}\right) \eta_n \quad (5.25)$$

To aid in computing Σ it is recognized that the nonzero entries of \mathbf{A}_F are just the coefficients of the characteristic polynomial of \mathbf{A} , and therefore $\|\mathbf{A}_F\| \leq$ to the maximum absolute value coefficient. The measure Σ is on the order of 1.0 for Along-Track equilibria, and on the order of $1.0e^3$ for Radial cases. The relative proximity of the Along-Track state space to an uncontrollable system causes difficulty in designing a charge only controller, and this sensitivity can cause the feedback law to diverge. A coordinate change in the dynamics or the adoption of a nonlinear controller might alleviate some of these difficulties, otherwise a hybrid control might add robustness to the controller design.

5.4 Feedback Stabilized Configurations

In this section a charge feedback law is derived to stabilize the in-plane dynamics for both the Along-Track and Radial configurations, with $\delta\mathbf{X}_{uc}$ perturbation dynamics ignored. Recalling the assumption of perfect full state observability, a charge feedback law is defined by Eq. (5.26), where \mathbf{K} is a feedback gain matrix for the full $\delta\mathbf{X}_c$ vector.

$$\delta\mathbf{u}(\tau) = \begin{bmatrix} \delta\tilde{q}_1/|\tilde{q}_1| \\ \delta\tilde{q}_2/|\tilde{q}_2| \\ \delta\tilde{q}_3/|\tilde{q}_3| \end{bmatrix} = -\mathbf{K} \delta\mathbf{X}_c(\tau) \quad (5.26)$$

It is demonstrated here, for the first time, that small state perturbations in the \hat{e}_R - \hat{e}_T plane can be asymptotically stabilized for both configurations, using only charge

control (no inertial thrust). From the dynamical system of Eq. (5.12), and using either Eqs. (5.13a)-(5.13b) or Eqs. (5.14a)-(5.14b), the gain matrix \mathbf{K} is found by solving the standard Linear Quadratic Regulator (LQR) problem.⁶⁷

For the presented simulations, both LQR weighting matrices are set to identity, and \mathbf{K} is solved using *MATLAB*'s "lqr" function. The formations are numerically integrated using the nonlinear equations of motion defined in Eqs. (2.21a)-(2.21b), with $d_1 = 30$ m, $d_3 = 25$ m, $\tilde{Q}_{13} = 1.0e^4$, and Table 2.1 parameter values.

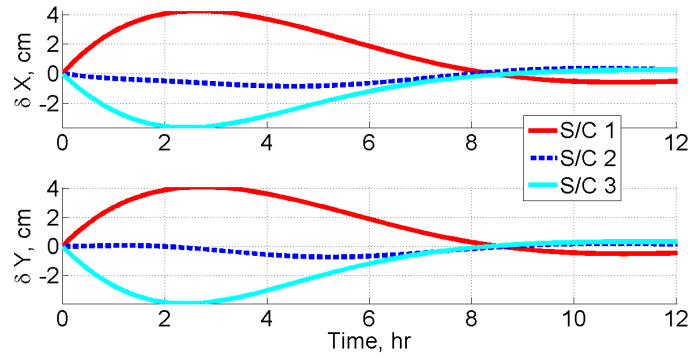


Figure 5.2: Controlled Radial Case A: Planar Position Perturbations after Initial S/C 1,3 $\Delta\mathbf{v}$ Disturbance

A position perturbation history is presented in Figure 5.2, that demonstrates an initially perturbed Radial configuration to be asymptotically stabilized using the Eq. (5.26) charge feedback law. This simulation shows the controlled response after initial $\Delta\mathbf{v}$ to crafts 1 and 3, with equal x and y components of 0.01 mm/s. In Figure 5.3, a similar position perturbation response is shown, but this simulates initial position disturbances to all three craft: $\Delta x_1 = -0.5$ m, $\Delta x_2 = 0.7$ m, $\Delta x_3 = -0.2$ m, $\Delta y_1 = 0.05$ m, $\Delta y_2 = -0.085$ m, and $\Delta y_3 = 0.035$ m.

A stabilized Along-Track configuration simulation (with 3 day propagation time) is shown in Figure 5.4, for the same initial $\Delta\mathbf{v}$ to crafts 1 and 3 as used in

generating Figure 5.2. Charge control histories, governed by the Eq. (5.26) feedback

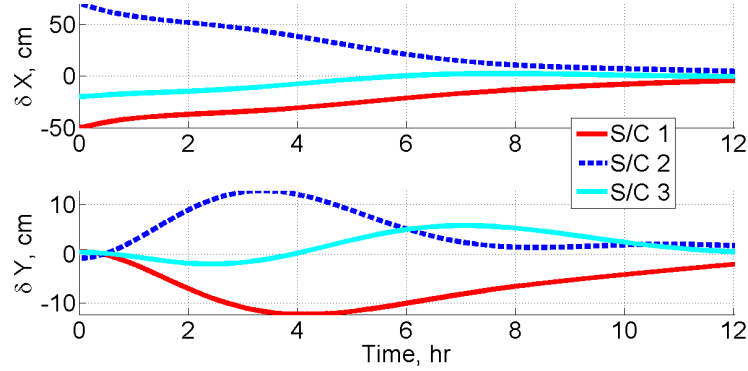


Figure 5.3: Controlled Radial Case A: Planar Position Perturbations after Initial S/C 1-3 $\Delta \mathbf{r}$ Disturbance

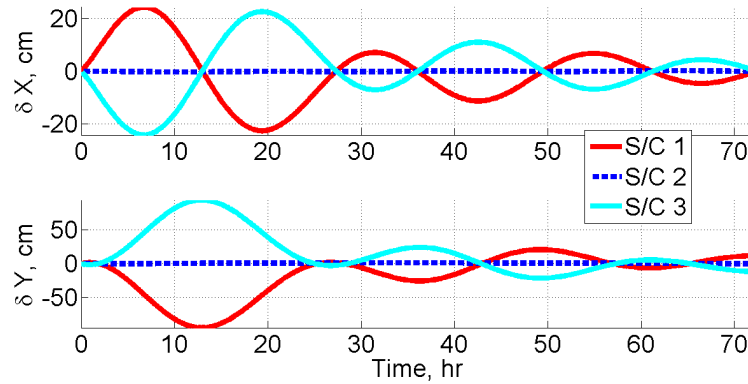


Figure 5.4: Controlled Along-Track: Planar Position Perturbations after Initial S/C 1,3 $\Delta \mathbf{v}$ Disturbance

law, and corresponding to the Figure 5.2 and Figure 5.4 simulations, are presented in Figure 5.5(a) and Figure 5.5(b), respectively. Note that nominal charge levels for either equilibria are quite small, μC order (ϕ_i on the order of 1 – 100 kV), and charge variations required to remove the initial disturbances are similarly small. Moreover, these levels are without minimum L_∞ norm charge selection applied, otherwise ϕ_i magnitudes would be less.

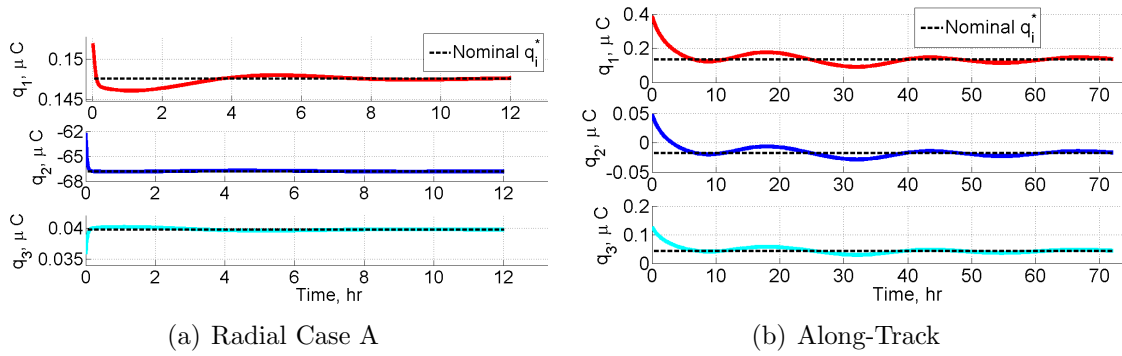


Figure 5.5: Charge Histories after Initial S/C 1,3 Δv Disturbance

There is greater overshoot and longer settling time for the Along-Track simulation than that of the Radial. This is due in part to the sensitivity of the system, and its being nearly uncontrollable. Higher order nonlinear terms also can significantly impact the Along-Track response, such that smaller perturbations are required to ensure 1st order approximation accuracy, compared with the Radial cases. This claim is substantiated in Figure 5.6(a), where the position perturbations used in generating the Figure 5.3 Radial simulation are repeated for the Along-Track configuration. The

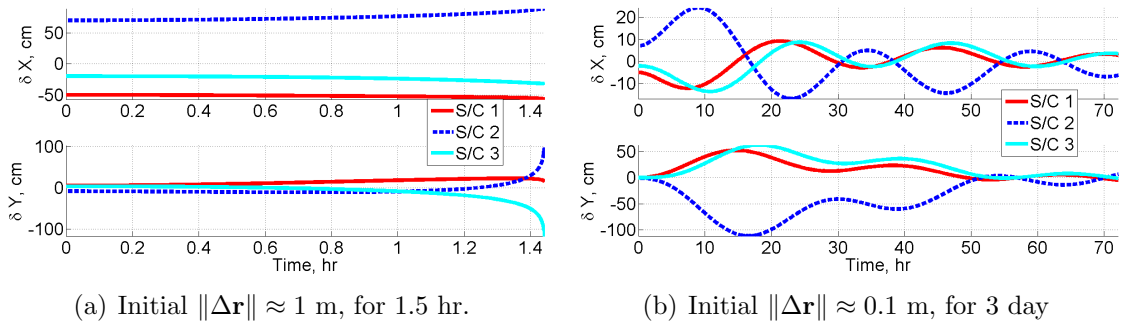


Figure 5.6: Controlled Along-Track: Planar Position Perturbations after Initial S/C 1-3 Δr Disturbances

resulting position perturbation history clearly shows divergence; however, if all initial perturbations are decreased by 1 order of magnitude, then asymptotic stability is

achieved, as illustrated in Figure 5.6(b).

Lastly, it is demonstrated for both configurations that the uncontrollable $\delta\mathbf{X}_{uc}$ perturbations do in fact remain bounded (uniformly stable), even when the complete system is propagated using nonlinear dynamics. Figure 5.7(a) (Radial) and Figure 5.7(b) (Along-Track) illustrate simulated out-of-plane perturbation histories, which remain bounded in response to initial disturbances: $\Delta z_1 = 0.05$ m, $\Delta z_2 = -0.125$ m, and $\Delta z_3 = -0.375$ m. These simulations also utilize the same in-plane initial perturbations as in Figure 5.2 (Radial) and Figure 5.6(b) (Along-Track), and again $\delta\mathbf{X}_c$ disturbances are removed asymptotically. Although these examples

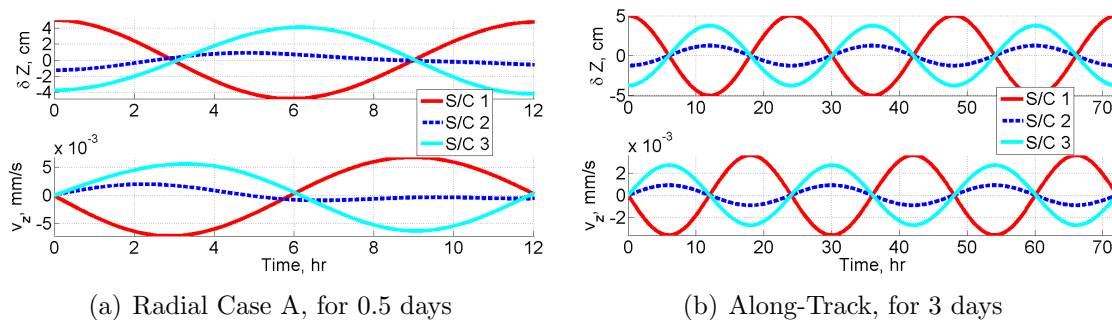


Figure 5.7: Out-of-Plane Position Perturbations after Initial S/C 1-3 $\Delta\mathbf{r}$ Disturbances

use equal mass, and a particular λ_d value, further simulations (not shown) indicate the feedback law is robust for alternate mass ratios and λ_d values.

5.5 Eigenspaces and Manifolds for Three-Craft Equilibria

In this section, eigenspace properties associated with the equilibrium regions derived in Section 5.2.1 are investigated numerically, based on the theoretical development of Section 2.6.2. In addition to these analyses, within each case, no overall stability bifurcations (changes to N_u or N_s) are witnessed upon varying d_1 , d_3 , \tilde{Q}_{13}^* ,

λ_d , and m_i over considerable ranges. This is strong numerical evidence that all configurations are dynamically unstable, although marginal axis stabilities can occur as demonstrated in Sections 5.3.2.1-5.3.2.3. Moreover, no bifurcations occur as $\lambda_d \rightarrow \infty$ (no shielding) for all cases except for the Along-Track, which bifurcates to $N_u = N_s = 0$ (all distinct eigenvalues). But even this special case, which exhibits linear uniform stability, is numerically unstable to small perturbations when considering the nonlinear Eqs. (2.23a)-(2.23c) of motion.

Linearized system eigenspaces are computed numerically from the zero-input state space form of Eqs. (2.34a)-(2.35d), using the necessary and sufficient equilibrium conditions outlined in Section 5.2.1, and with Table 2.1 parameter values. For Along-Track and Radial case A configurations $\tilde{Q}_{13}^* = 1.0e^4$ is used, whereas for Orbit-Normal cases \tilde{Q}_{13}^* is selected just inside the feasible boundary, and for Radial cases B-C it is set equal to the mean of the corresponding upper and lower bound. Resulting eigenspace properties, for each case over variable d_1 and d_3 , are as follows.

1. Along-Track

$N_u = N_s = 1$ (distinct real) - Mode is contained in the \hat{e}_R - \hat{e}_T plane. Perturbations along \hat{e}_N only are marginally stable.

2. Orbit-Normal Case A

$N_u = N_s = 4$ (2 complex pairs) - All unstable/stable modes are contained in the \hat{e}_R - \hat{e}_T plane, and therefore perturbations along \hat{e}_N only are marginally stable.

3. Orbit-Normal Case B

$N_u = N_s = 3$ (1 complex pair, 1 mode real) - The complex mode is contained in the \hat{e}_R - \hat{e}_T plane.

- $|d_1 - d_3|$ Small. Real mode is contained in the \hat{e}_R - \hat{e}_T plane. Perturbations along \hat{e}_N only are marginally stable.
- $|d_1 - d_3|$ Large. Real mode is entirely along \hat{e}_N . Perturbations along \hat{e}_N only are unstable.

4. Radial Case A

$N_u = N_s = 2$ (2 distinct real) - Both modes are contained in the \hat{e}_R - \hat{e}_T plane, and perturbations along \hat{e}_N only are marginally stable.

5. Radial Cases B-C

- $|d_1 - d_3|$ Small. $N_u = N_s = 3$ (1 complex pair, 1 real) - All contained in the \hat{e}_R - \hat{e}_T plane. Perturbations along \hat{e}_N only are marginally stable.
- $|d_1 - d_3|$ Large. $N_u = N_s = 3$ (3 distinct real) - Two modes are contained in the \hat{e}_R - \hat{e}_T plane, and the other mode is entirely along \hat{e}_N . Perturbations along \hat{e}_N only are unstable.

A particularly interesting result from this analysis, is the out-of-plane stability bifurcation that arises for Orbit-Normal case B and Radial cases B-C, as a function of $|d_1 - d_3|$. This represents a numerical verification of what was shown analytically possible for Radial cases B-C in Section 5.3.2.3. The observation is especially important, because it demonstrates how marginal out-of-plane stability for Radial configurations (and line of sight marginal stability for Orbit-Normal) can be achieved through careful selection of the distances d_1 and d_3 , and the charge product \tilde{Q}_{13}^* .

These eigenspace changes depend on $|d_1 - d_3|$ as well as \tilde{Q}_{ij}^* magnitudes, and their existence and the conditions under which they arise, were previously unknown.

For either axis of alignment, the \hat{e}_N instabilities arise when two craft are in close proximity and have a repulsive Coulomb force which becomes larger than restorative forces, including differential gravity. Visual explanations for their appearance are considered in Ref. 43, and reproduced in Sections 5.5.1-5.5.2.

5.5.1 Radial Out-of-Plane Instability

All Radial configuration cases exhibit at least one Coulomb force magnitude that is on the order of differential gravity. For case A, large attractive forces act between inner craft, while the outer craft repel, but with a relatively small force magnitude. For cases B-C, the two craft in closest proximity repel, and all forces are similar in magnitude. Force diagrams for both cases are shown in Figures 5.8(a)-5.8(b), where arrow thickness roughly indicates relative force magnitude. For case A,

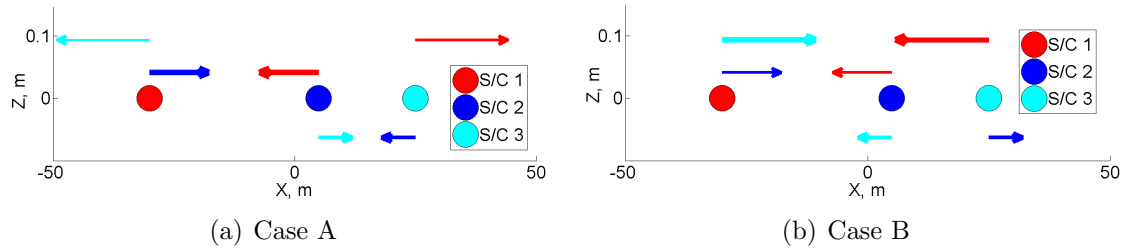


Figure 5.8: Three-Craft Radial Configuration Force Diagrams

any z component perturbations are quickly restored by the strong inner craft forces. Whereas similar perturbations for case B can strengthen the repulsive force acting on craft 2, thereby overcoming restorative forces, and further increasing the z component perturbation. This occurs when d_{23} is small ($|d_1 - d_3|$ large), and when \tilde{Q}_{23}^* is large enough. This qualitative insight agrees with the numerical conclusions of the previous section, and also with the analytical conclusions made in Section 5.3.2.2-5.3.2.3. Moreover, it is the \hat{e}_N axis perturbations which can destabilize the formation; how-

ever, as distances increase those perturbations do remain bounded. The 2- and 3-craft Radial configurations are hereby demonstrated to have in-plane Coulomb controllability and modal stability properties in common, with the exception of this single parameter dependent unstable mode.³⁵

5.5.2 Orbit-Normal Out-of-Plane Instability

The case A Orbit-Normal configurations are marginally stable along the \hat{e}_N direction, a result previously unknown for the 3-craft configurations, but a property known to be true for the 2-craft Orbit-Normal equilibrium.²² Scenarios when the Orbit-Normal case B equilibria no longer retain this property, are again apparent when analyzing the force diagrams. These are shown in Figures 5.9(a)-5.9(b), with the case A configuration having all repulsive forces. Therefore, any contraction of the formation is repelled, and any expansion is countered by differential gravity. In contrast, the case B configuration has attractive forces between inner craft, and therefore perturbations which bring those vehicles closer, may continue to grow, eventually leading to unstable growth. This is important, because so long as d_1 , d_3 , and \tilde{Q}_{13}^* are

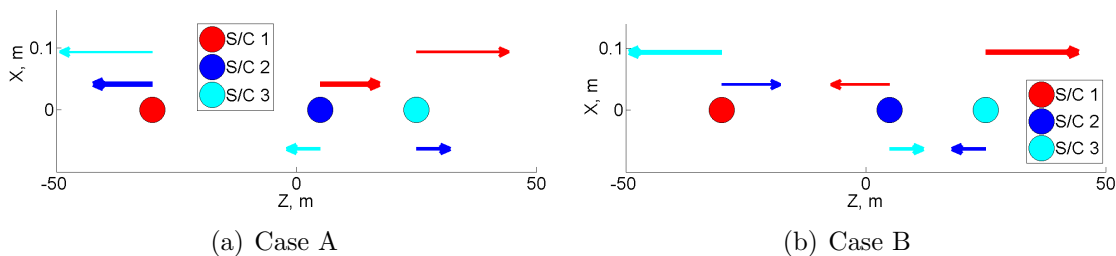


Figure 5.9: Three-Craft Orbit-Normal Configuration Force Diagrams

selected properly, substantial control effort need only be applied to in-plane perturbations. Marginal stability along the \hat{e}_N axis, is utilized by Natarajan and Schaub²² to reduce station-keeping control effort for the 2-craft Orbit-Normal equilibrium. The

same could be done for 3-craft, but now care must be taken to avoid this modal instability.

5.5.3 Invariant Manifolds

Invariant manifolds are generated to illustrate some of the Section 5.5 stability properties, and also for understanding to what extent natural motions can be exploited to aid in formation reconfigurations. Again seeking near-heteroclinic orbits to aid in reconfigurations that may include expansions and contractions of the overall distance d_{13} , transfers between equilibrium regions, and transfers between one axis of alignment to another. In future work, manifolds may be considered to expel or add a craft, by transferring between a 2-craft equilibrium and a 3-craft equilibrium (with one craft leaving or entering the system). The global manifolds are propagated using the Eqs. (2.23a)-(2.23c) nonlinear dynamics, and following the procedure outlined in Section 2.6.2 ($\epsilon = 0.1$ mm/s). The eigenspaces are computed numerically from the Eqs. (2.34a)-(2.35d) state space, as done previously. It is ascertained from the Section 5.5 analysis that Orbit-Normal cases and Radial cases B-C ($|d_1 - d_3|$ large) have

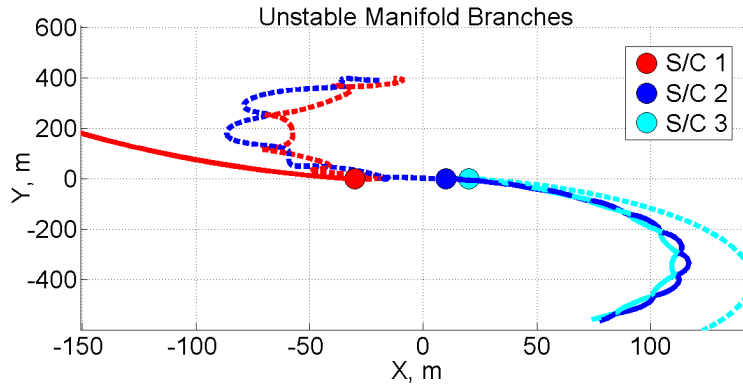


Figure 5.10: Three-Craft Radial Case A Unstable Manifolds Propagated $1.0 T_p$, with $d_1 = 30$ m, $d_3 = 25$ m, and $\tilde{Q}_{13}^* = 1.0e^4$

manifolds in \mathfrak{R}^6 , whereas the remaining cases are in \mathfrak{R}^4 (unstable and stable modes confined to the $\hat{e}_R\text{-}\hat{e}_T$ plane).

Radial case A unstable manifold trajectories, bounded to the reference orbit plane, are reflected in Figure 5.10. These also display strong attractive Coulomb interaction of the inner craft, causing the numerous trajectory intersections. In con-

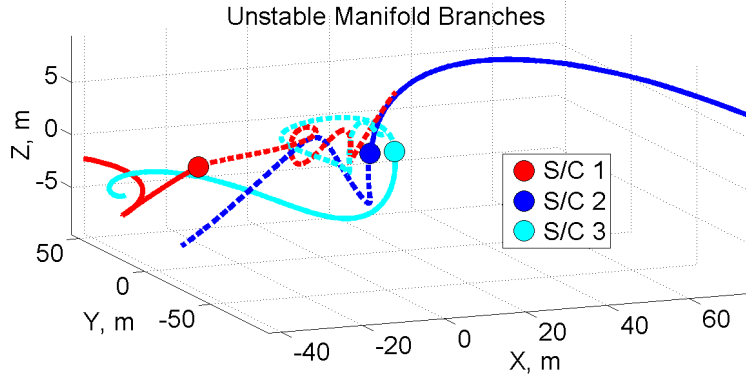


Figure 5.11: Three-Craft Radial Case B Unstable Manifolds Propagated $0.5 T_p$, with $d_1 = 30$ m, $d_3 = 18$ m, and $\tilde{Q}_{13}^* = -2.56e^7$

trast, Figure 5.11 visually demonstrates the out of orbit plane instability that can arise for Radial case B, resulting in a \mathfrak{R}^6 manifold structure, and confirming the analytical result of Section 5.3.2.3 and the numerical eigenspace analysis of Section 5.5. Figure 5.11 provides insight into the instability, showing that initial out-of-plane perturbations invoke attractive forces to bring all vehicles together, which in turn, results in an increasing δz_2 perturbation for craft 2. On both branches, the purely real \hat{e}_N axis unstable mode is quite distinct.

Along-Track stable and unstable manifolds are illustrated in Figures 5.12-5.13. There is great symmetry between stable and unstable branches, and it is rather intuitive to visualize a near-heteroclinic orbit, to expand or contract the shape.

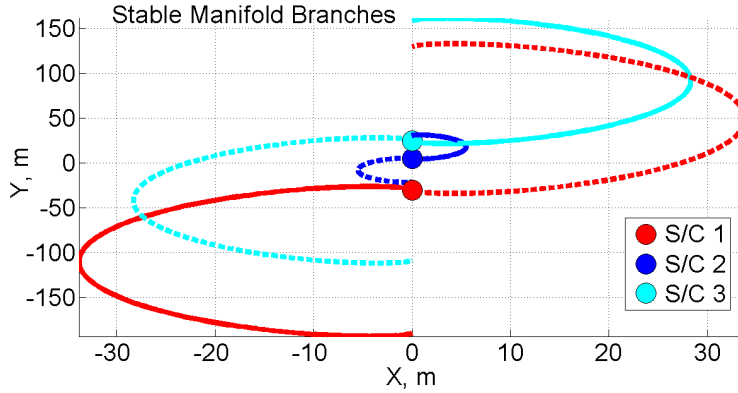


Figure 5.12: Three-Craft Along-Track Stable Manifolds Propagated $1.0 T_p$, with $d_1 = 30$ m, $d_3 = 25$ m, and $\tilde{Q}_{13}^* = 1.0e^4$

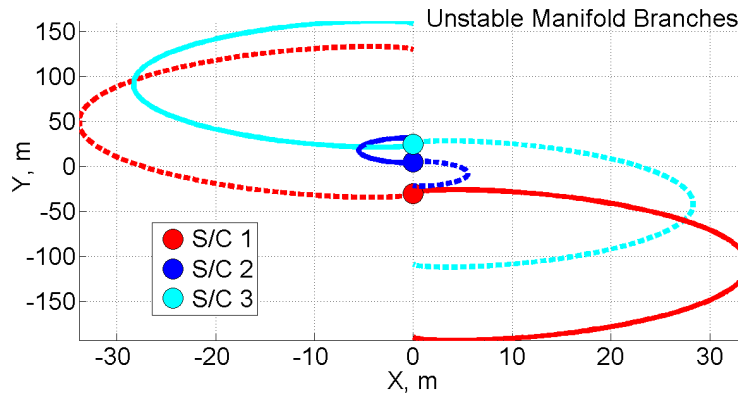


Figure 5.13: Three-Craft Along-Track Unstable Manifolds Propagated $1.0 T_p$, with $d_1 = 30$ m, $d_3 = 25$ m, and $\tilde{Q}_{13}^* = 1.0e^4$

Lastly, Figures 5.14-5.15 depict example Orbit-Normal unstable manifolds. The case A instance resembles the 2-craft Orbit-Normal manifolds of Section 4.4, which also exhibit marginal stability along the line of sight vector. The case B example reflects the strong attractive Coulomb interaction between craft 2 and 3, and again it is this force which can overcome differential gravity and lead to the \hat{e}_N axis unstable mode.

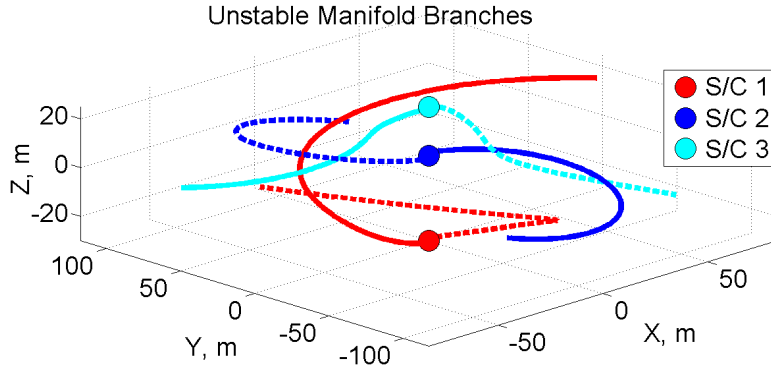


Figure 5.14: Three-Craft Orbit-Normal Case A Unstable Manifolds Propagated $1.0 T_p$, with $d_1 = 30$ m, and $d_3 = 25$ m, and $\tilde{Q}_{13}^* = 5.9e^6$

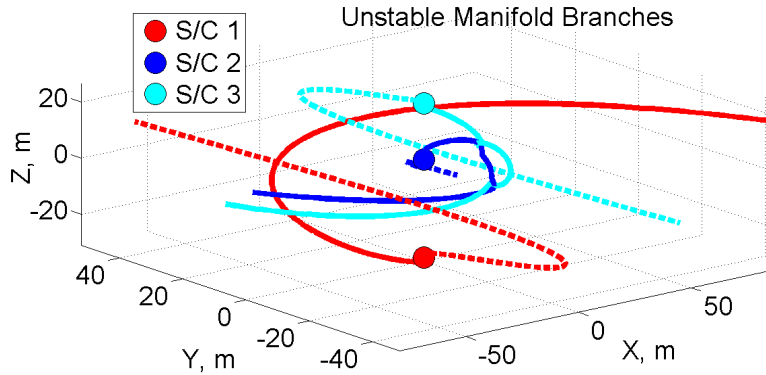


Figure 5.15: Three-Craft Orbit-Normal Case B Unstable Manifolds Propagated $1.0 T_p$, with $d_1 = 30$ m, and $d_3 = 25$ m, and $\tilde{Q}_{13}^* = 1.43e^7$

5.5.4 Near-Heteroclinic Orbits for Three-Craft Equilibria

The identification of reconfiguration scenarios in which natural manifold flows may partially provide the transfer, analogous to those considered in Section 4.6 for 2-craft equilibria, motivates this section. Equally salient is the determination of situations where manifold reconfigurations are impractical. The recognition and improved quality of such initial guess (IG) trajectories, represent important prerequisite steps in extending (to 3-craft collinear formations) the optimal reconfiguration method out-

lined in Section 4.5. As noted, expansions and contractions between Along-Track configurations are relatively intuitive to visualize. An example IG trajectory which would expand the Along-Track configuration is shown in Figure 5.16, where d_{13} is increased by 10 meters and r_2^* is moved from +5 meters to +3 meters. This is merely

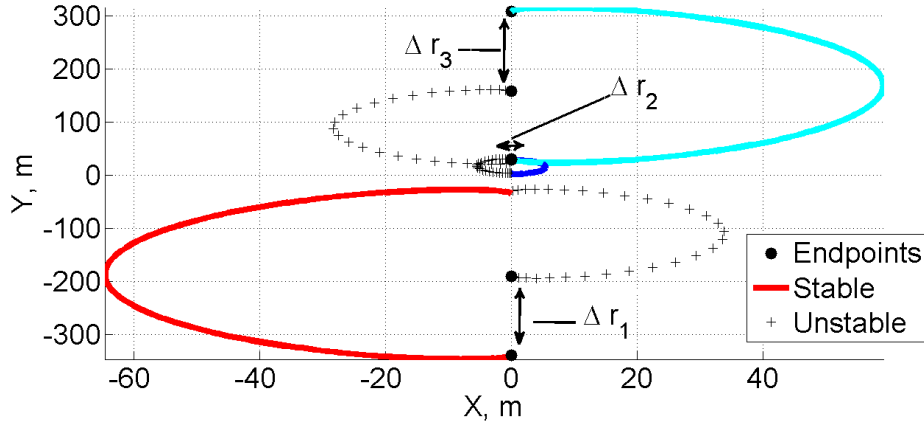


Figure 5.16: Along-Track Discontinuous Expansion along Manifolds Propagated 1 T_p , with $d_1 = 30 \rightarrow 36$ m, and $d_3 = 25 \rightarrow 34$ m

near-heteroclinic, since there are state discontinuities between unstable and stable manifolds at the patch point (endpoints of near manifold intersection). Nevertheless, it is likely these could be differentially corrected, to yield continuous transfers with ΔV minimized, as formulated and demonstrated for 2-craft equilibria in Sections 4.5-4.6 and in Refs. 42, 44.

Another IG expansion example, is presented in Figure 5.17. This time to increase d_{13} by 20 m (and keep r_2^* constant) in an Orbit-Normal case A alignment. This transfer is more difficult to visualize because it is \mathfrak{R}^6 , with velocity directions that are hard to ascertain. Moreover, the Figure 5.17 expansion does not technically represent a near-heteroclinic transfer, since in this scenario, the manifolds are best exploited when the spacecraft numbering is allowed to change. The Figure 5.17

5.6 Chapter Conclusions

Necessary and sufficient conditions which enable, 3-craft collinear, static formations are derived in the presence of a linearized gravity model, and include partial Coulomb force shielding. Linearized stability and controllability analyses are performed, and the configurations are shown to share many, but not all, properties with their 2-craft counterparts (presented in Chapter 4). Key differences for 3-craft (relative to 2) include the Along-Track configuration having in-plane Coulomb force controllability, and the Radial and Orbit-Normal cases exhibiting a, parameter dependent, out-of-plane modal instability.

Perturbations normal to the reference orbit plane are uncontrollable for Radial and Along-Track aligned cases, but can be uniformly stable. And for these cases analytical analyses and derivations, verified by numerical simulation, demonstrate that a linearized charge feedback law (without inertial thrusting) can asymptotically stabilize small in-plane perturbations, using the complete nonlinear dynamics. This result was previously unknown, and demonstrates how the dynamical properties of these systems may be utilized to reduce station-keeping control effort. Unfortunately, Along-Track equilibria are numerically sensitive and nearly uncontrollable, resulting in a small region of linear approximation accuracy.

Future work should test the current linearized feedback controller further, over larger parameter value ranges (e.g. m_i and λ_d) and with the inclusion of prominent continuous disturbances, such as solar radiation pressure. The robustness of the control law might also be improved, and similar controllers might be derived and tested in a higher fidelity dynamical model with more relaxed assumptions. Specifically, the controlled response characteristics could be refined, to achieve desired performance,

by tuning the LQR weighting matrices, or by adopting alternate feedback control strategies, possibly even a nonlinear method. The latter continuation might prove especially relevant for the sensitive Along-Track cases. The observability problem might also be addressed in further research, using a realistic sensor measurement model, in part to assess how state errors affect the conclusions and results presented in this investigation. Optionally, a similar charge feedback law could be derived and tested, but with the objective of expanding and contracting a given configuration (changing the d_{ij} distances).

Invariant manifold theory is applied to all equilibrium configurations, and examples are given showing that transfers between Along-Track equilibria (and to a lesser extent between Orbit-Normal equilibria) offer the best opportunities for near-heteroclinic orbits, which could then be differentially corrected to match continuity. The methodology for converging minimal ΔV transfers between 2-craft Coulomb equilibria, outlined in Section 4.5, now also appears applicable to particular 3-craft collinear scenarios. However, a continued investigation which fully applies the Section 4.5 method, both analytically and numerically, would be necessary to ascertain and quantify how useful the approach actually is. Nevertheless, that pursuit is shown here as being a potentially valuable one in realizing the advantageous property of Coulomb formations to change shape, with reduced fuel cost.

Chapter 6

Perturbed Coulomb Formation Trajectories

6.1 Chapter Summary

All results presented in Chapters 3-5 were acquired assuming the simplified dynamical model outlined in Chapter 2. In this chapter the accuracy of select solutions are considered, when propagated in an inertial frame model that includes nonlinear gravity, primary disturbances, and parameter uncertainties. Such simulations represent the obvious next step in transitioning the ideal solutions to higher fidelity, and also are used to numerically validate various stability properties claimed within the simplified model. In Section 6.2.1, a solar radiation pressure acceleration is given and an interpolated model is developed to simulate the effect of uncertainty in the parameter λ_d . Trajectories integrated within this higher accuracy inertial model, are then transformed to the Hill frame for comparison, as outlined in Section 6.2.2.

Numerical results are presented in Section 6.3 for two-craft periodic Coulomb formations, and two-craft static equilibria invariant manifolds. For all tested examples, despite inducing a smaller instantaneous force magnitude than solar radiation pressure, variable λ_d causes the greatest deviations from nominal. However, this only considers absolute radiation pressure (i.e. zero differential pressure between craft). Qualitative stability conclusions made using Floquet theory in Section 3.4, are validated by these numerical simulations for planar and full state solutions. Moreover, example solutions with maximum Floquet multipliers near unity are shown to remain

in the vicinity of nominal when subjected to primary perturbations, all without feedback control. Such solutions are considered invaluable in terms of station-keeping cost. The invariant manifolds show minimal deviation even with the most unfavorable λ_d variational conditions, and this provides evidence that converged optimal reconfigurations of Chapter 4 may accurately transform to higher fidelity models.

6.2 Inertial Model with Primary Perturbations

Referring back to Figure 2.2, the position vector \mathbf{R}_i of each spacecraft, with respect to the Earth centered inertial frame \mathcal{N} , may be propagated independently in accordance with Eq. (6.1).

$$\mathbf{R}_i''(\tau) = \frac{\mu}{\omega^2 R_i^3} \mathbf{R}_i + \frac{\tilde{q}_i}{m_i} \sum_{\substack{j \\ j \neq i}} \frac{\tilde{q}_j \left(1 + \frac{R_{ij}}{\lambda_d}\right) \mathbf{R}_{ij}}{R_{ij}^3 \exp[R_{ij}/\lambda_d]} + \tilde{\mathbf{f}}_{\text{srp}} \quad (6.1)$$

Where $R_{ij} = \|\mathbf{R}_i - \mathbf{R}_j\|$ is a separation distance (equal to r_{ij}), μ is the Earth's gravitational constant, and $\tilde{\mathbf{f}}_{\text{srp}}$ is a scaled solar radiation pressure (SRP) acceleration. Although not explicitly stated, terms on the right hand side are τ dependent, and the first term is the classical gravitational acceleration scaled into non dimensional time. Charge histories $\tilde{q}_i(\tau)$ are known functions assumed to be dependent on a nominal Hill frame model solution $\mathbf{X}^*(\tau)$. Therefore, deviations from $\mathbf{X}^*(\tau)$ due to $\tilde{\mathbf{f}}_{\text{srp}}$, nonlinear gravity terms, and parameter uncertainties are not reflected in the charge control.

The $\mathbf{X}^*(\tau)$ solution contains initial \mathbf{r}_i and \mathbf{v}_i , such that initial \mathbf{R}_i are obtained via Eq. (2.7) (with \mathbf{R}_{cm} and $\dot{\mathbf{R}}_{\text{cm}}$ specified at the circular reference orbit). Initial $\dot{\mathbf{R}}_i$ are obtained using Eq. (6.2), again assuming initially aligned \mathcal{N} and \mathcal{H} unit vectors, and where $\dot{\mathbf{r}}_i = \omega \mathbf{v}_i$, with velocity vectors subsequently rescaled as $\mathbf{R}'_i = \dot{\mathbf{R}}_i \omega$.

$${}^{\mathcal{N}}\dot{\mathbf{R}}_i = \dot{\mathbf{R}}_{\text{cm}} + \dot{\mathbf{r}}_i + (\boldsymbol{\omega} \times \mathbf{r}_i) \quad (6.2)$$

6.2.1 Perturbation Models

The primary disturbing force for Coulomb formations near GEO is SRP,⁵⁰ and in fact it is shown to be far more important than higher order gravitational terms. The other very important perturbation which is modeled and simulated here, is not a physical force but rather the parametric uncertainty in the Debye length. All prior Coulomb formation trajectories assumed a constant nominal λ_d , but in actuality λ_d varies quite significantly in time and space, and therefore it is important to analyze the sensitivity of the solutions to this variation. The cannonball SRP model is naturally adopted for the spherical craft,^{50,69} such that the dimensional acceleration on craft i is given by Eq. (6.3).

$$f_{\text{srp}} = C_R \frac{\pi R_{sc}^2 \Theta}{m_i c} \quad (6.3)$$

Where $\Theta = 1372.5398 \text{ W/m}^2$ denotes the solar flux constant at 1 AU, c the speed of light, and C_R the coefficient of reflectivity (an average value based on recent data of $C_R = 1.3$ is assumed).^{16,50} For an $R_{sc} = 1 \text{ m}$ spacecraft this amounts to a force of around $18 \mu\text{N}$. The unit vector from Sun to Earth is assumed constant over any simulation and in the $\hat{i}\text{-}\hat{k}$ plane. Therefore, in accordance with \mathcal{N} being an equatorial frame, the scaled acceleration vector is defined by Eq. (6.4).

$$\tilde{\mathbf{f}}_{\text{srp}} = -\frac{f_{\text{srp}}}{\omega^2} \begin{bmatrix} \cos(23.4) \\ 0 \\ \sin(23.4) \end{bmatrix}^{\mathcal{N}} \quad (6.4)$$

In Ref. 20, 10-year averaged experimental plasma data are presented, for the GEO regime, versus local time and K_p (an integer index between 0 – 9, with 1 being

calm and > 5 indicating noisy or stormy geomagnetic activity). From these data, Debye length versus K_p is interpolated, at various local times (equivalent to mean anomaly for GEO spacecraft). A fast Fourier transform (keeping the first four coefficients) is then applied to that data,⁷⁰ for three K_p index values. The resulting analytical interpolated λ_d expressions as a function of mean anomaly (equivalent to τ in radians) are plotted in Figure 6.1, where a mean anomaly of 180 degrees corresponds to being between the Earth and Sun. These interpolated functions are used

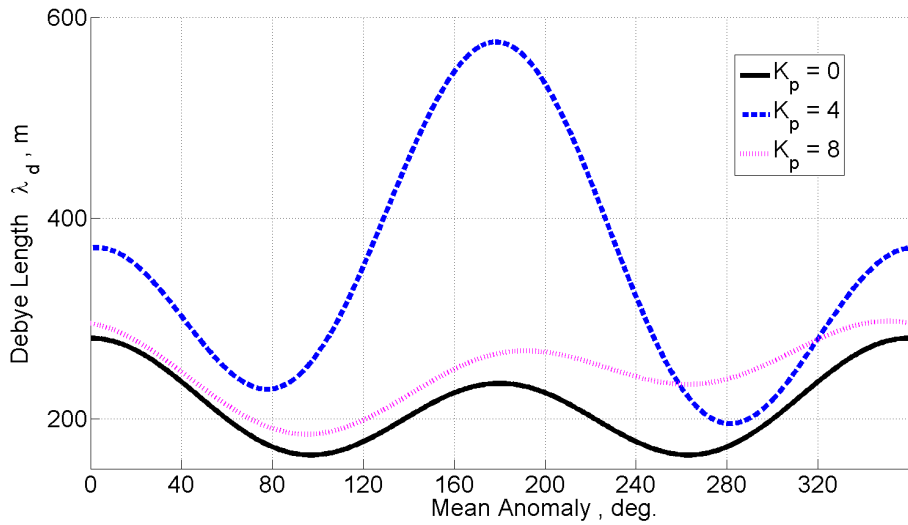


Figure 6.1: Interpolated Debye Length at GEO versus Anomaly and K_p

to simulate realistic variations in λ_d and the disturbances they generate. Although the true $\lambda_d(\tau)$ can involve stochastic and chaotic behavior, this model does capture the largest magnitude time variations. Therefore, it is deemed sufficient to provide an initial assessment of the sensitivity of open-loop Coulomb formation solutions, to λ_d uncertainty.

The magnitude of the Coulomb force perturbation, due to a $\Delta\lambda_d$, may be readily approximated using the truncated Taylor series derived in Eq. (6.5). Where

the Coulomb force expression from Eq. (6.1) has been unscaled prior to performing the partial derivative.

$$m_i \Delta \ddot{R}_i \approx \left(\frac{\partial \ddot{R}_i}{\partial \lambda_d} \right) \Big|_* \Delta \lambda_d = \left(\frac{k_c Q_{ij}^*}{\lambda_d^3 \exp[R_{ij}/\lambda_d]} \right) \Delta \lambda_d \quad (6.5)$$

Equation (6.5) indicates that the perturbation magnitude increases in proportion to Q_{ij}^* , and in inverse proportion to the separation distance R_{ij} . However, this is only valid for a single Coulomb interaction, whereas in formations of more than 2 vehicles the force perturbations may be additive or subtractive. In Table 6.1, 2-craft Coulomb force perturbation magnitudes due to instantaneous $\Delta \lambda_d$ are presented, computed using the fully nonlinear Ψ coefficients and the Table 2.1 constant values. Ranges

Table 6.1: Coulomb Force Perturbation from Variable Debye Length

ϕ_1 , kV	$\Delta \lambda_d$, m	$m_i \Delta \ddot{R}_i$, μN	ϕ_1 , kV	$\Delta \lambda_d$, m	$m_i \Delta \ddot{R}_i$, μN
Radial Equilibrium, $R_{12} = 50$ m			Orbit-Normal Equilibrium, $R_{12} = 50$ m		
37.10	50	0.714	21.42	50	0.238
37.10	300	1.658	21.42	300	0.553
$R_{12} = 20$ m			$R_{12} = 80$ m		
10	50	0.062	10	50	0.045
10	300	0.135	10	300	0.106
50	50	1.506	50	50	1.117
50	300	3.399	50	300	2.668
100	50	6.022	100	50	4.469
100	300	13.598	100	300	10.674

used for ϕ_1 and R_{12} are consistent with those encountered in this dissertation, and the Table 6.1 results verify all parameter dependencies implied by the Eq. (6.5) Taylor series approximation. The instantaneous disturbances are all less than the 18 μN SRP disturbance (often considerably so); however, SRP is constant in magnitude and

direction, whereas the perturbation resulting from $\lambda_d(\tau)$ uncertainty is not.

6.2.2 Transformations from ECI to Hill Frame

Upon integrating via Eq. (6.1), with some combination of the perturbations developed in Section 6.2.1, the vectors $\mathbf{R}_i(\tau)$, $\mathbf{R}'_i(\tau)$, $\mathbf{R}_{\text{cm}}(\tau)$, and $\mathbf{R}'_{\text{cm}}(\tau)$ are known (the latter two computed explicitly from the former two). To compare these higher fidelity \mathcal{N} frame trajectories to the nominal \mathcal{H} frame trajectories, a transformation must be performed. First, position vectors ${}^{\mathcal{N}}\mathbf{r}_i(\tau)$ are computed using Eq. (2.7), and scaled velocity vectors ${}^{\mathcal{N}}\mathbf{v}_i(\tau)$ are transformed using Eq. (6.6).

$${}^{\mathcal{N}}\mathbf{v}_i = \mathbf{R}'_i - \mathbf{R}'_{\text{cm}} - (\mathbf{n} \times \mathbf{r}_i) , \quad \mathbf{n} = \left(\frac{\mathbf{R}_{\text{cm}} \times \mathbf{R}'_{\text{cm}}}{\|\mathbf{R}_{\text{cm}}\|^2} \right) \quad (6.6)$$

Here \mathbf{n} denotes the true angular velocity vector of the \mathcal{H} frame, in contrast to the nominal angular velocity that is denoted $\boldsymbol{\omega}$. The transformed trajectories are still in the \mathcal{N} frame basis, and therefore the Eqs. (6.7a)-(6.7b) rotation (transform) matrix \mathbf{T} is applied, such that ${}^{\mathcal{H}}\mathbf{r}_i = [\mathbf{T}] {}^{\mathcal{N}}\mathbf{r}_i$ and ${}^{\mathcal{H}}\mathbf{v}_i = [\mathbf{T}] {}^{\mathcal{N}}\mathbf{v}_i$.

$$\mathbf{T} = [\hat{\mathbf{T}}_1 \mid \hat{\mathbf{T}}_2 \mid \hat{\mathbf{T}}_3]^T \quad \hat{\mathbf{T}}_1 = \frac{\mathbf{R}_{\text{cm}}}{R_{\text{cm}}} \quad (6.7a)$$

$$\hat{\mathbf{T}}_3 = \frac{\mathbf{R}_{\text{cm}} \times \mathbf{R}'_{\text{cm}}}{\|\mathbf{R}_{\text{cm}} \times \mathbf{R}'_{\text{cm}}\|} \quad \hat{\mathbf{T}}_2 = \hat{\mathbf{T}}_3 \times \hat{\mathbf{T}}_1 \quad (6.7b)$$

6.3 Perturbed Coulomb Formation Numerical Simulations

All subsequent results are generated using the Table 2.1 constant values (except of course for varying λ_d), and are intended to reproduce previously presented ideal trajectories and to verify relative stability claims. To quantify and compare

deviations in the high-fidelity trajectories from nominal, an L_2 norm of the absolute error in the craft 1 position vector is computed at the final time t_f (non dimensional τ_f). Although not necessarily at the time of largest deviation, this measure denoted X_{err} , is defined in Eq. (6.8).

$$X_{\text{err}} = \|\mathbf{r}_1(\tau_f) - \mathbf{r}_1^*(\tau_f)\|_2 \quad (6.8)$$

Where $\mathbf{r}_1(\tau)$ is a disturbed trajectory position vector (transformed to the Hill frame), and $\mathbf{r}_1^*(\tau)$ is a nominal trajectory position vector obtained using the simplified dynamical model.

6.3.1 Perturbed In-Plane Periodic Coulomb Formations

The planar periodic orbits, as derived in Section 3.3.1, are propagated via Eq. (6.1) with only SRP as a perturbing force (i.e. λ_d constant). Some quantifiable

Table 6.2: Planar Periodic Coulomb Formation Deviations with SRP

Case	A_x , m	t_p , hrs.	t_f , hrs.	X_{err} , m
A	20	12	48	$1.05e^3$
A	20	2.4	48	$1.11e^2$
A	50	2.4	48	$3.87e^3$
B	20	12	48	$3.65e^{-2}$
B	20	2.4	48	$7.34e^{-3}$

trajectory error results are given in Table 6.2, which show case B solutions remain near nominal much longer than case A solutions. These data validate stability claims made in Section 3.4.2, including relative instability (measured here by X_{err}) increasing in proportion to A_x and inversely with the relative motion period.

The way in which SRP effects the solutions, in contrast to varying Debye length, is considered here, by integrating a single periodic solution with each dis-

turbance included independently. Deviations from nominal, in components of the position vector \mathbf{r}_1 , are presented in Figures 6.2-6.3 respectively for each perturbation.

It is clear that although the instantaneous perturbation from variable λ_d is smaller

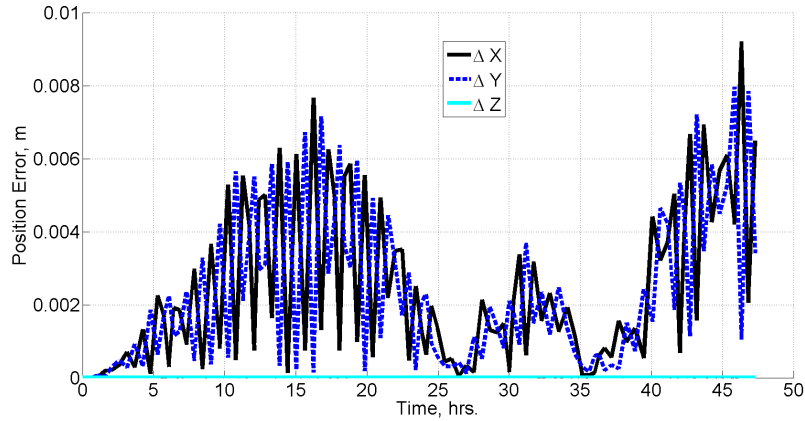


Figure 6.2: Position Deviations for SRP Perturbed Planar Periodic Solution: Case B, $A_x = 20$ m, and $t_p = 2.4$ hrs.

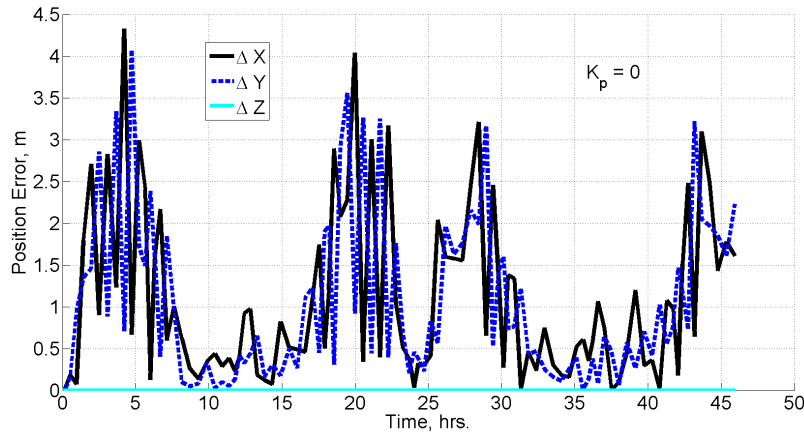


Figure 6.3: Position Deviations for Variable Debye Length Perturbed Planar Periodic Solution: Case B, $A_x = 20$ m, and $t_p = 2.4$ hrs.

in magnitude than SRP, it disturbs the orbit far more (3 orders of magnitude). The non secular terms in the errors (for either modeled perturbation) are quite complex,

and different from each other, with the varied λ_d case clearly showing a 24 hour oscillatory mode. Moreover, there is in fact a non zero out-of-plane error, though it is significantly smaller than the orbit plane deviations.

Relative stability measures laid forth in Section 3.4.2, are immensely important when considering the feedback control effort required to maintain one of these relative orbit types. To illustrate this point, two perturbed periodic Coulomb formations are shown in Figures 6.4-6.5, with the only difference between them being either case A or case B (i.e. how the major axis is aligned). These are integrated with both

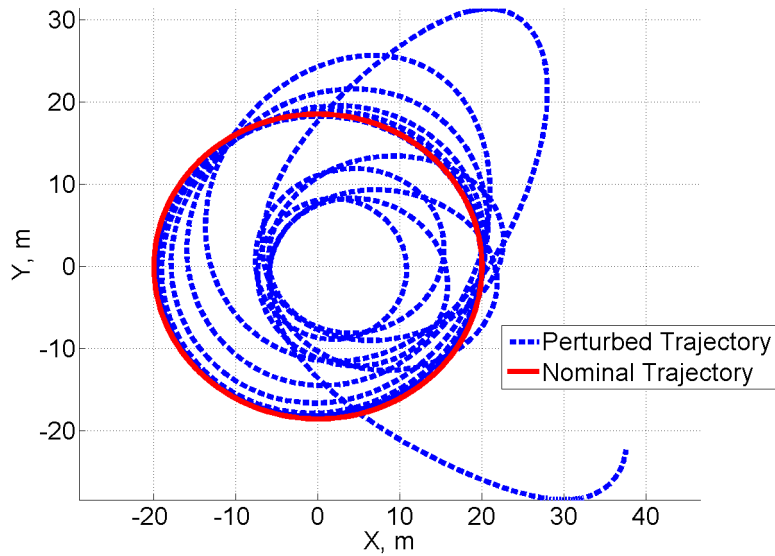


Figure 6.4: Perturbed Planar Periodic Solution Trajectory for 10 Revolutions: Case A, $A_x = 20$ m, and $t_p = 2.4$ hrs.

SRP and variable Debye ($K_p = 0$) present, and the case B solution with major axis along \hat{e}_T remains in the vicinity of nominal for $40 \tau_p$ (4 days), whereas the case A solution becomes wildly departs nominal in less than 10 revolutions (1 day). This invaluable facet is unique to the periodic Coulomb formations, as all static Coulomb formations (with gravity considered) quickly leave nominal when subjected

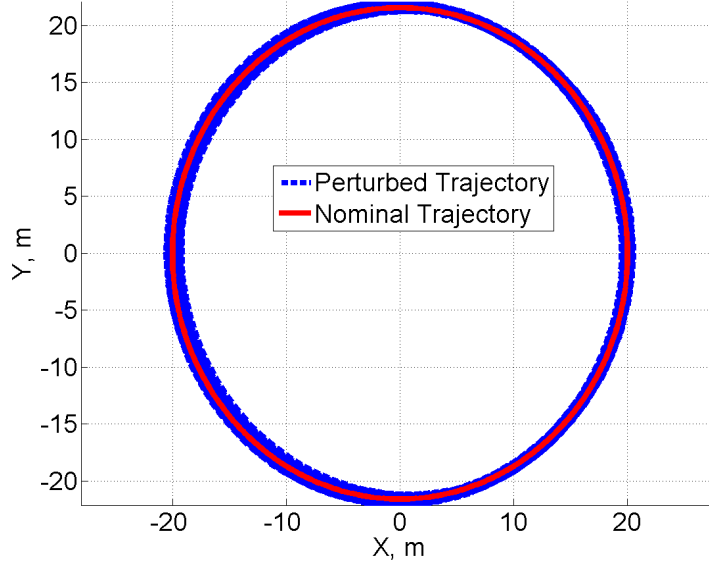


Figure 6.5: Perturbed Planar Periodic Solution Trajectory for 40 Revolutions: Case B, $A_x = 20$ m, and $t_p = 2.4$ hrs.

to a perturbed environment (in fact departing along associated unstable manifolds). Figure 6.5 provides numerical evidence that a relative Coulomb orbit exists which exhibits nonlinear open-loop uniform stability (in the Lyapunov sense).⁴⁸

Table 6.3: Planar Periodic Coulomb Formation Deviations with Varied Debye

Case	A_x , m	t_p , hrs.	t_f , hrs.	X_{err} , m
A	20	2.4	48	$2.66e^3$
B	20	12	48	$3.33e^2$
B	20	2.4	48	$1.76e^{-1}$
B	50	2.4	48	$2.08e^3$
B	20	2.4	336	$5.75e^{-2}$

Table 6.3 summarizes some key results for simulations including only the Debye length variation ($K_p = 0$). These are presented in part to compare with SRP data given in Table 6.2, but also interestingly the last row in Table 6.3, corresponding to

the Figure 6.5 solution, shows deviation no more than tens of centimeters, over a 2 week period.

The Debye variation clearly causes the greatest disturbance, even at relatively quiet $K_p = 0$ geomagnetic conditions. These results also confirm Section 3.4.2 relative instability claims. Specifically, that X_{err} increases in proportion to A_x and inversely with t_p , just as with SRP. And despite the fact that the $\lambda_d(\tau)$ induced force perturbation magnitude instantaneously is less at greater R_{ij} , as determined in Section 6.2.1, resulting state deviations over time are still (somewhat non intuitively) greater for larger R_{ij} orbits.

6.3.2 Perturbed Full State Periodic Coulomb Formations

The testing undertaken in Section 6.3.1 is repeated here, but now for the full state periodic solutions derived in Section 3.3.3. Some error results for $B_z = 2$ nominal orbits with only SRP active are shown in Table 6.4, and these data very clearly assert that case A solutions, are indeed, relatively more unstable than case B. The additional $|\sigma|_{\text{max}}$ trends identified in Section 3.4.6 are also reflected here,

Table 6.4: Full State Periodic Coulomb Formation Deviations with SRP, $B_z = 2$

Case	A_x , m	A_z , m	Revs.	t_f , hrs.	X_{err} , m
A	20	10	2.5	43.9	$1.05e^3$
A	50	5	2.5	43.9	$8.62e^2$
B	20	10	2	98.7	$8.50e^{-2}$
B	40	10	2	98.7	$2.72e^0$
B	10	45	2	98.7	$3.95e^{-3}$

specifically that X_{err} increases in proportion to A_x and B_z . Table 6.5 provides results

with only Debye length variation active, and again this induced perturbation causes greater state deviations than SRP.

Table 6.5: Full State Periodic Coulomb Formation Deviations with Varied Debye

Case	A_x , m	A_z , m	B_z	K_p	Revs.	t_f , hrs.	X_{err} , m
A	20	10	2	0	2.5	43.9	$1.59e^3$
B	20	10	2	0	2	98.7	$3.66e^2$
B	10	45	4	0	1	97	$5.43e^1$
B	10	45	2	0	2	98.7	$4.91e^{-1}$
B	10	45	2	4	2	98.7	$1.85e^1$
B	10	45	2	8	2	98.7	$5.64e^0$

For a particular barely unstable solution, the geomagnetic parameter K_p is shown to cause greater deviations during storm conditions, as expected. Much of

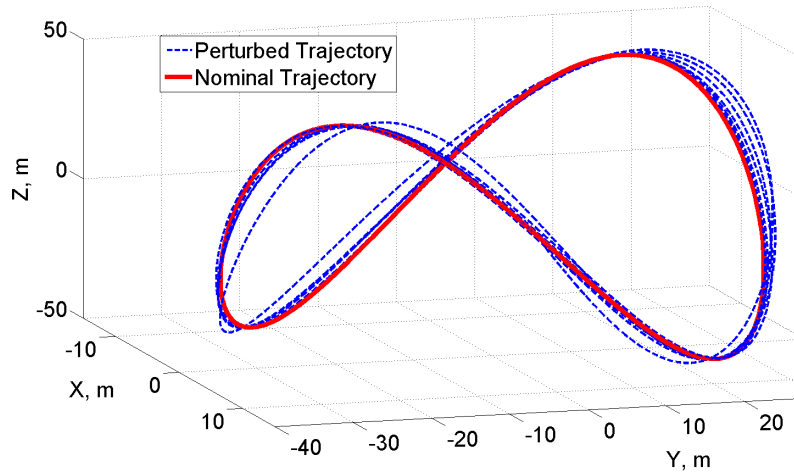


Figure 6.6: Perturbed Full State Periodic Solution Trajectory: Case B, $A_x = 10$ m, $A_z = 45$ m, $B_z = 2$, and $t_f = 296.1$ hrs.

the focus in Table 6.5 is devoted to this particular solution, because it corresponds to the smallest $|\sigma|_{max}$ (least unstable) case found numerically in Section 3.4.6, over

a range of A_x , A_z , and B_z . This solution is therefore integrated for 6 relative orbit revolutions (nearly 300 hours), with SRP and Debye variation present ($K_p = 0$), and the resulting perturbed trajectory is plotted alongside nominal in Figure 6.6. This represents a full state periodic solution that remains in the vicinity of the nominal (deviation < 2.6 m) for considerable time, without feedback stabilization. Compare this to the very unstable analogue integration shown in Figure 6.7, where the case A nominal corresponds to the primary example solution considered in Section 3.4.5. Here the disturbed trajectory exponentially departs in less than half a revolution

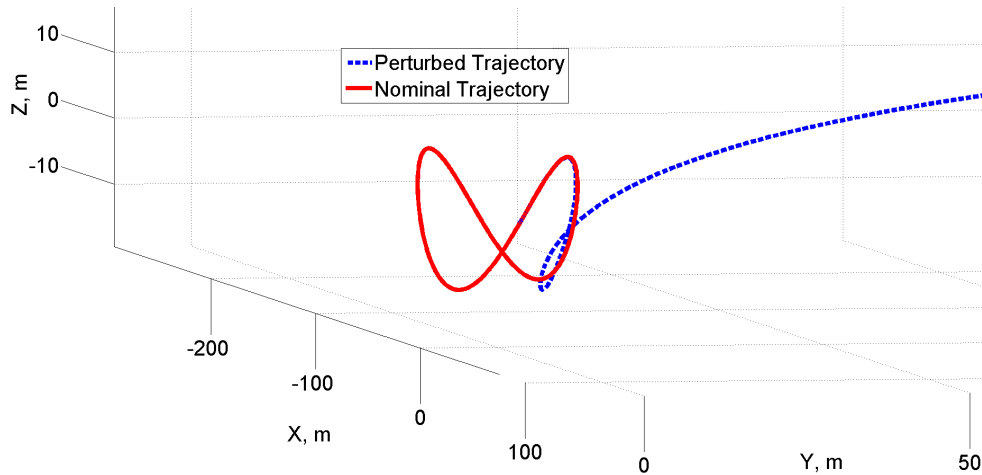


Figure 6.7: Perturbed Full State Periodic Solution Trajectory: Case A, $A_x = 20$ m, $A_z = 10$ m, $B_z = 2$, and $t_f = 17.6$ hrs.

(under 18 hours shown), with SRP and Debye variations present ($K_p = 0$).

Full state periodic solutions in general have larger $|\sigma|_{\max}$ than do planar solutions, and the larger relative instability is generally brought out in these numerical simulations. However, an interesting result is that there do exist full state periodic solutions, as in Figure 6.6, which remain in the vicinity of nominal for long duration, when subjected to primary perturbations.

6.3.3 Perturbed Invariant Manifolds of Two-Craft Equilibria

Because most of the 2-craft optimal transfer durations, targeted in Chapter 4, occur along the natural invariant manifolds, the accuracy of the reconfigurations, in this higher fidelity dynamical model, can be approximately assessed by the accuracy of the manifolds. This is done here by integrating initial manifold state vectors \mathbf{X}^u and \mathbf{X}^s , within the Eq. (6.1) dynamical framework, to generate example trajectories similar to Figure 4.4 (Radial) and Figure 4.6 (Orbit-Normal) from Section 4.4. Craft 1 unstable manifold branches are illustrated in Figure 6.8 (Radial + branch) and in Figure 6.9 (Orbit-Normal both branches), with nominal and perturbed trajectories plotted alongside one another. Both SRP and Debye variation perturbations are

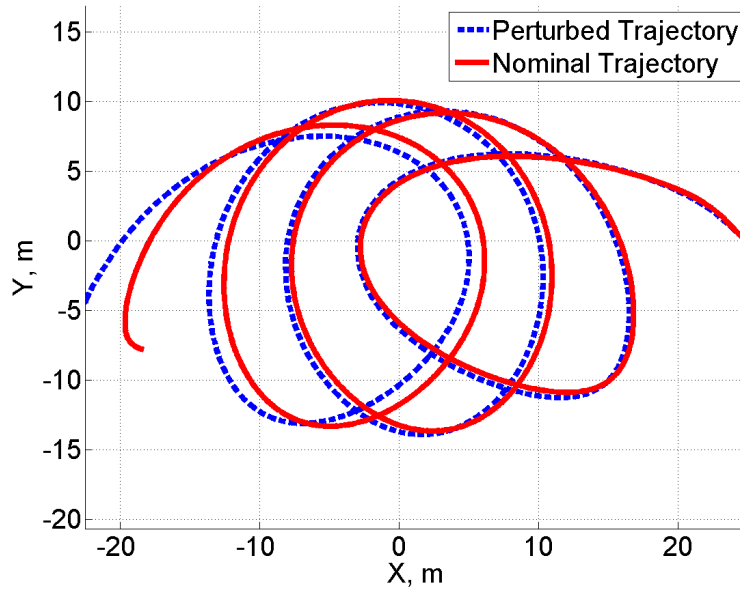


Figure 6.8: Perturbed Radial Equilibria S/C 1 Unstable Manifolds, for 1 T_p

active, with $K_p = 4$ (storm condition) used to yield the greatest disturbance. Nevertheless, the overall deviations are small and therefore a larger equilibrium separation distance of $r_{12}^* = 50$ m is used. Otherwise, all the same parameter values used in

Section 4.4 are repeated here. The Radial branch results in $X_{\text{err}} = 5.24$ m after 1 day (and in fact that deviation decreases with decreasing r_{12}^* and ϵ). The Orbit-Normal branches result in around $X_{\text{err}} = 15$ m after 2 days.

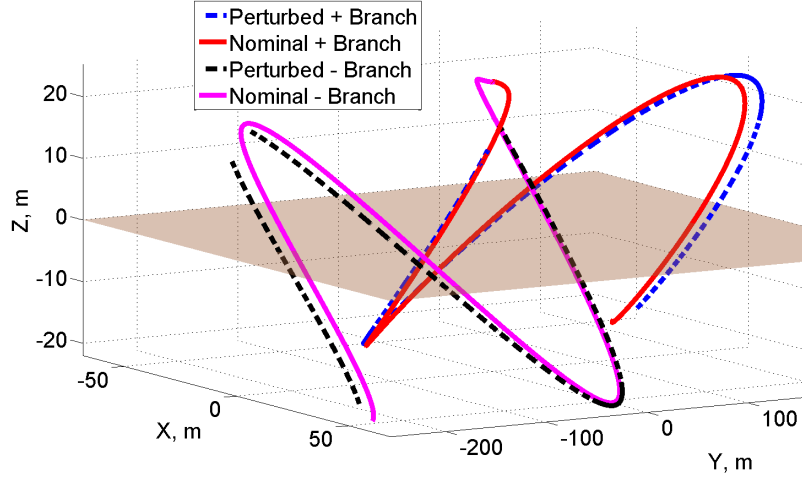


Figure 6.9: Perturbed Orbit-Normal Equilibria S/C 1 Unstable Manifolds, for $2 T_p$

These provide quantitative evidence that 2-craft Coulomb formation invariant manifolds are only slightly altered by worst case primary perturbations, and parametric uncertainty. Therefore optimal 2-craft equilibria shape changes, converged in the Hill frame model with simplified dynamics, should translate accurately to a high-fidelity dynamical model, assuming the simplified (albeit with variable λ_d) electrostatic force model remains valid.

6.4 Chapter Conclusions

Inertial propagation of previously derived trajectories, with the inclusion of solar radiation pressure and an interpolated variable Debye length model, provides insight into how accurately certain solutions and methodologies may translate to a

greater fidelity model. Interestingly, the induced disturbance due to variable and uncertain Debye length has a far greater effect on the Coulomb formation motions than does SRP, despite the latter having a larger instantaneous magnitude.

Of course, feedback stabilization could still overcome such model uncertainties; however, in general this would require some inertial thrusting, that could be costly in terms of mass as well thruster plume impingement. Therefore, all the more important are those periodic Coulomb formations shown to remain in the vicinity of nominal, for many relative orbit cycles, in a higher fidelity environment. These results show that (for certain cases) periodic relative motion solutions are far less unstable than comparable static equilibria solutions. Moreover, particular solutions seem to exhibit uniform stability in the perturbed nonlinear environment, and therefore may have advantageous application. For example, in providing a low cost means of allowing multiple spacecraft to share a single Geostationary slot.

Invariant manifolds associated with the 2-craft static equilibria are mostly insusceptible to primary perturbations, which is positive news for being able to achieve the optimal reconfigurations presented in Chapter 4 in a more realistic dynamical setting. However, these are still incredibly sensitive trajectories and therefore a tiny difference in actual versus expected $\Delta\mathbf{v}$ used to initiate the manifolds can have drastic effects on position as a function of time.

Overall the work in this chapter shows many of the simplified Hill frame model solutions transform quite well to higher accuracy; however, some of the solutions (particularly case A orbits) are very unstable. Also the inertial model used here considers only disturbances in the space environment and gravity model, but does not reflect many other higher order aspects of the electrostatic model. These subtle unmodeled

factors include terms which are truncated from the Vlasov-Poisson model, coupled spacecraft capacitances, and overlapping craft potentials (additionally coupled with the environment).^{2,26} Such considerations, although interesting, are beyond the scope intended here, but should be pondered for extended research.

Chapter 7

Conclusions

7.1 Overall Summary

The research described in this dissertation applies new theory to a variety of current challenges facing Coulomb formation flying. It also introduces new possibilities for effectively and efficiently operating and maneuvering electrostatic spacecraft. In particular, techniques from dynamical systems theory, used extensively in multi-body gravity field trajectory design, are extended to relative motion trajectories, involving the highly nonlinear internal Coulomb forces.

In Chapter 3 the first examples of periodic relative orbits enabled by electrostatic forcing functions are derived, and these represent a desired advancement from the more thoroughly studied static Coulomb formations. The orbits are shown to occur in families and with much variation in terms of relative instability. In Chapter 6 some example orbits are shown to exhibit boundedness in the nonlinear inertial equations of motion with primary perturbations included. This is an important result, since such solutions would require very little station-keeping effort, whereas arbitrary solutions necessitate near continuous control operation.

There are many interesting orbit cases derived, such as an inertially fixed line of sight vector case (at varied distance), but more importantly is the possibility for innumerable other periodic solutions. The derived Hill frame integral of motion, valid for N craft Hill frame model formations (with any arbitrary internal forcing), should

continue to prove useful in seeking such open- or closed-loop motions.

In Chapters 4-5 invariant manifold theory is applied to static Coulomb formations for the first time. A methodology is developed for formulating and solving minimum inertial control effort reconfigurations between 2-craft equilibria, along differentially corrected manifolds. There are a multitude of permutations in formulating these parameter optimization problems, and this work provides broad coverage of these considerations and the numerical effect they can have. The two-craft manifolds are shown in Chapter 6 to be fairly insensitive to primary perturbations, which suffices as evidence that the converged optimal reconfigurations would translate readily to a more accurate dynamical model.

Progress is made in understanding the three-craft collinear Coulomb formations, in a variety of ways, in Chapter 5. First, necessary and sufficient equilibrium conditions are stated concisely, with the inclusion of plasma shielding. Second, a numerical stability analysis for the various equilibrium cases is completed, and it is demonstrated analytical that particular cases may be asymptotically stabilized in the reference orbit plane, using charge control alone. Finally, a Coulomb force feedback law is derived and shown capable of stabilizing the relevant equilibria, subject to small in-plane perturbations. Limited Coulomb force controllability necessitated this thorough investigation of the system stability properties, in order to best utilize charge control for feedback stabilization. Future work can build upon this fundamental result, to advance the controller performance and diversify the control objectives.

7.2 Recommended Future Work

The Coulomb formation is a novel concept, very much still in its infancy, and this dissertation addresses a few specific challenges which are to be overcome or handled more effectively, prior to mission implementation. This research has initiated many more new questions and new pathways of investigation, than it has settled. In analyzing the motions of these systems with techniques from dynamical system theory, an assortment of practical and academically interesting continuations have been brought to light. The following extensions stand out as particularly fruitful, in the opinion of the author.

- The derivation of an approximate closed form solution to the 2-craft Coulomb formation dynamical model, using perturbation and expansion theories.
- An investigation regarding how well the derived Hill frame integral of motion holds in an inertial high-fidelity model, and what implications this has for potential periodic formation solutions, including those utilizing some other internal force mechanism (other than electrostatic force).
- The derivation and analysis of additional periodic Coulomb formations, possibly represented in finite Fourier series. Perhaps with additional spacecraft, or using a somewhat different dynamical model (e.g. CRTBP).
- Determining the existence of non conservative forced periodic solutions, those with charge functions that are not state dependent. And also the derivation of periodic solutions enabled by a general internal force.
- Determining the existence of quasi-periodic solutions, either those resulting from the periodic solutions integrated using higher order or perturbed dynamics,

but also those which may be analytically or numerically derived within the established dynamical model of this dissertation.

- Feedback stabilization of the periodic Coulomb formation solutions, preferably with as little inertial thrusting as possible. There are many options here including discrete feedback methods.
- The application of invariant manifold theory and the optimal reconfiguration method, to consider transfers between periodic Coulomb formation solutions.
- Further examination of the optimal 2-craft reconfiguration problem, including formulations with free times, and improved or otherwise alternate control parameterizations. Added attention should be given to higher order control approximations, and the inclusion of practical constraints for thruster plume impingement and charge control bounds.
- Recast the optimal reconfigurations to minimize a hybrid performance index that includes power required and an inertial thrusting measure. Could also formulate these as optimal control theory problems, and attempt to solve the resulting two-point boundary value problems.
- Extending the 2-craft optimal reconfiguration method to the potentially applicable 3-craft collinear transfers outlined in Section 5.5.4. Moreover, transfers between 2-craft and 3-craft equilibria could be investigated, with one vehicle entering or leaving the system.
- Expand upon the 3-craft collinear feedback stabilization laws, to perform in-plane charge controlled reconfigurations. Also consider improving the robustness of these feedback laws, possibly with the derivation of a nonlinear controller.

- Investigate possibility of using pulse-width modulation (or similar) for charge control, as opposed to the assumed continuously differentiable functions.
- Further assessment of the accuracy of all solutions and methods when considering higher fidelity Coulomb force models, or for scenarios in which certain assumptions used throughout this dissertation are no longer valid.
- Sensitivity of solutions to a slightly eccentric reference orbit, and/or the derivation of similar solutions when allowing for eccentricity in the differential gravity model.
- A continued assessment into the sensitivities and accuracies of solutions with respect to additional parametric uncertainties, and the inclusion of higher order Coulomb force considerations (e.g. added coupling). The numerical study might be supplemented by an analytical parameter sensitivity analysis.
- The development of an observability model and estimation method for Coulomb formation control should be addressed. This should include a realistic sensor model, for the measurement of spacecraft state variables, charge control, and even plasma parameters.

Generally, this investigation utilizes very ideal electrostatic and plasma environment modeling, only accurate under a variety of assumed circumstances. Doing so was important, if not necessary, to allow for much of the analytical development and application of dynamical systems theory techniques. However, the many subtle issues facing spacecraft charging, Coulomb forces, and plasma modeling should be incrementally considered to move the theoretical results of this dissertation closer

to practice. This might include coupled spacecraft capacitance, potential dependent Debye length, six degree of freedom motion due to non spherical charged spacecraft, time dependent and stochastic plasma property variations, and others. Additionally, exactly how to precisely measure, estimate, and control the electric potential remains an open question. Finally, practical considerations such as how to accommodate other spacecraft subsystems (e.g. communications) within a Coulomb formation architecture must also be addressed.

Overall the results presented in this dissertation will be useful to continued and higher fidelity investigations of Coulomb formation maneuvering. This research has established the foundation for investigating open-loop periodic Coulomb formation motions, and for utilizing invariant manifold theory to control and reconfigure the formations optimally. Insights from dynamical systems theory have illuminated various stability properties, crucial to efficiently maintain the shapes and in exploiting natural flows. The application of these techniques should extend to other, perhaps more complex, Coulomb systems, and also in general to relative spacecraft motion problems involving nonlinear force coupling.

7.3 Concluding Remarks

Major achievements of this work include the demonstrable existence of periodic Coulomb formations, the successful application of invariant manifold theory and formal optimization to converge minimum cost Coulomb formation shape changes, and the use of dynamical systems theory to show that certain canonically transformed 3-craft configurations can be feedback stabilized, using charge control alone. These contributions all involve applying particular analytical or numerical techniques, used

in other areas of space mission design, to the specific problem of Coulomb formation flying. This work is not a study to show electrostatic forces as the best mechanism for formation flying control, nor is it an attempt to establish how to implement such a system under practical and higher order considerations. Rather it manifests some first order means to better extract the benefits of charge control, while minimizing the inherent downsides. Much of the latter involves mitigating the limited controllability, and exploiting (rather than begrudging) the nonlinearities.

From a purely theoretical and mathematical standpoint, this subject proved an excellent dissertation topic. From a practical point of view, there is still much uncertainty about Coulomb formations, and electrostatic force control generally. At this time, the concept is still a visionary one; however, with its potential for delivering much needed cost reductions in space operations, it should continue to advance rapidly. The viability of close flying charged spacecraft is dependent on advanced methods for handling the complexities associated with it. Nevertheless, the evolution from monolithic space structures to flexible, reconfigurable, and electromagnetic structures seems an inevitable, and already occurring process. The analyses and methods presented in this dissertation represent an integral, albeit humble, part of the transition to handling the added complexities associated with a particular free-flying system, in order to realize its inherent benefits. A guiding principle throughout this research endeavor, was to deliver a fresh theoretical perspective to the Coulomb formation topic. And the fulfillment of such labors has thereby illuminated some fascinating relative motion dynamics, which may be possible with the implementation of electrostatic forcing.

Appendices

Appendix A

Parameterized Charge Control Bounds

Values for the parameters ΔQ_j and \dot{Q}_j , used in approximating an optimal charge product variation history $\delta\tilde{Q}_{12}(\tau)$, may impose infeasible power, current, or transition time requirements on the charge control device. This section derives expressions to quantify such requirements, and thereby define feasibility bounds for ΔQ_j and \dot{Q}_j . The PSO solver method requires bounds on these parameters, but otherwise the expressions could be used in post processing. The following development assumes time-fixed optimization (i.e. all τ_j remain at their IG values, and are not included in \mathbf{X}_p). And the Eq. (2.22) convention is enforced, such that $\tilde{q}_1(\tau) = +\sqrt{|\tilde{Q}_{12}(\tau)|}$. A constant operating current of $|I_{\text{out}}| = 80 \mu\text{A}$ (based on the worst case experimental I_{en} value for GEO), is used to quantify the power required and transition time needed, as explained in Section 2.2.2. Therefore, these rough computations amount to consistently high P_{out} but low Δt_q estimates.

An instantaneous charge change (i.e. piecewise constant approximation) is only reasonable if steady state is reached on a time scale much less than the spacecraft dynamical response. The Eq. (2.6) expression for the transition time Δt_q can be rearranged to yield Eq. (A.1), an upper bound on the parameters ΔQ_j .

$$|\Delta Q_j|_{\text{max}} \leq k_c \left(\frac{(\Delta t_q)_{\text{max}} I_{\text{out}}}{\omega} \right)^2 \quad (\text{A.1})$$

Where Eq. (2.22) relates scaled \tilde{Q}_{12} to unscaled q_1 , and $(\Delta t_q)_{\text{max}}$ is an input parameter

corresponding to the maximum tolerable transition time to achieve some ΔQ_j at the operating current I_{out} . For the PSO results obtained in Section 4.6 the value of this parameter is set to $(\Delta t_q)_{\text{max}} = 1.0$ ms.

Imposing a maximum power limit is also an important consideration, and therefore Eq. (2.4), used to compute P_{out} , is written in terms of the charge control parameters. To do this, Eq. (2.2) and Eq. (2.22) are substituted into Eq. (2.4) to eliminate ϕ , which results in the following expressions for the impulsive and linear charge control models, respectively.

$$P_{\text{max}} = \frac{\omega |I_{\text{out}}|}{R_{sc}} \left[\sqrt{k_c |\tilde{Q}_{12}^*|} + N \sqrt{k_c |\Delta Q_j|_{\text{max}}} \right] \quad (\text{A.2a})$$

$$P_{\text{max}} = \frac{\omega |I_{\text{out}}|}{R_{sc}} \left[\sqrt{k_c |\tilde{Q}_{12}^*|} + \sqrt{k_c \Delta \tau_{\text{tot}} |\dot{Q}_j|_{\text{max}}} \right] \quad (\text{A.2b})$$

Where P_{max} is an input parameter for the maximum tolerable P_{out} , and $\Delta \tau_{\text{tot}}$ is the total controlled duration along each branch: $\Delta \tau_{\text{tot}} = \tau_f - \tau_1^u$ for unstable, and $\Delta \tau_{\text{tot}} = \tau_N^s - \tau_f$ for stable. Hence, Eqs. (A.2a)-(A.2b) are calculated individually for the unstable and the stable branch, and then the larger right hand side case is taken. Furthermore, whenever Eqs. (A.1)-(A.2b) are applied to define PSO method parameter bounds, or in post processing, the value $|I_{\text{out}}| = 80 \mu\text{A} \geq |I_{\text{en}}|$ is used. Charge control parameter bounds for the PSO method results presented in Section 4.6 are generated as follows.

- **Impulsive:** Simultaneous values for $|\Delta Q_j|_{\text{max}}$ and I_{out} , which satisfy both Eq. (A.1) and Eq. (A.2a) for specified P_{max} and $(\Delta t_q)_{\text{max}}$ are computed.
- **Linear:** A $|\dot{Q}_j|_{\text{max}}$ value is computed from Eq. (A.2b), for a specified P_{max} .

The convention of assuming equal magnitude individual charges, with $q_1(\tau) > 0$ can result in unnecessarily large individual charge discontinuities at the patch point. This is encountered, for example, in Section 4.6.5 concerning Orbit-Normal to Radial transfers, and the problem would be exacerbated if considering 3-craft (or more) reconfigurations. For transfers between Orbit-Normal and Radial equilibria, $\tilde{Q} = \tilde{Q}_{12}^*$ goes from positive to negative, and therefore at least one individual charge must change sign. The magnitude of any discontinuity at τ_f could be reduced simply by relaxing the $|\tilde{q}_1| = |\tilde{q}_2|$ convention (while maintaining the optimal \tilde{Q}_{12} history). As an example, assume $\tilde{Q}_{12}^u(\tau_f) = 1.0e6$ and $\tilde{Q}_{12}^s(\tau_f) = -1.0e6$ (a large discontinuity), with craft 1 transferring to the craft 2 slot. Maintaining the Eq. (2.22) convention results in a $\Delta\tilde{q}(\tau_f) = 2000$ charge change (≈ 13.5 kV). On the other hand if \tilde{q}_1^u is allowed to decrease to $\tilde{q}_1^u(\tau_f) = 100$ (while \tilde{q}_2^u increases), and also if \tilde{q}_2^s is allowed to increase to $\tilde{q}_2^s(\tau_f) = -100$ (while \tilde{q}_1^s becomes larger positive), then a mere $\Delta\tilde{q}(\tau_f) = 200$ change occurs (≈ 1.3 kV). Nevertheless, this alternative convention is beneficial only for reducing power and transition times, since large potential changes (kV order) may be achieved quickly (millisecond order) using moderate power (order of Watts).

Generally, some convention has to be assumed in order to parameterize the two-craft charge control using a single optimization variable (in this work \tilde{Q}_{12} is used). Because of this parameterization, an optimal Coulomb force history does not yield a unique individual charge history, and each permissible individual charge solution will have correspondingly varied feasibility (e.g. power required). Extended investigations might wish to parameterize the charge (or ϕ_i) history of each spacecraft, and enforce continuity of the charges at the patch point, all in a way that ideally addresses the considerations outlined in this section.

Appendix B

Analytical Gradients

The following derivation of analytical gradients for two-craft optimal reconfigurations (used in generating Section 4.6 numerical results), are for time-fixed problems (i.e. τ_j are not included in \mathbf{X}_p). The parameter vector is populated as in Eq. (B.1).

$$\mathbf{X}_p = \begin{bmatrix} \left[\begin{array}{cccc} \Delta Q_1^u & (\Delta \mathbf{v}_1^u)^T & \dots & \Delta Q_N^u & (\Delta \mathbf{v}_N^u)^T \end{array} \right]^T \\ \left[\begin{array}{cccc} \Delta Q_1^s & (\Delta \mathbf{v}_1^s)^T & \dots & \Delta Q_N^s & (\Delta \mathbf{v}_N^s)^T \end{array} \right]^T \\ \Delta \mathbf{v}_f \end{bmatrix} \quad (\text{B.1})$$

Where impulsive charge control parameters $\Delta Q_j^{u/s}$, are simply replaced by $\dot{Q}_j^{u/s}$ parameters when considering a piecewise linear approximation. Recall $\mathbf{X}(\tau)$ denotes a state vector, and $\mathbf{Y}(\tau)$ the Eq. (4.4) augmented state vector. A state propagation matrix for $\delta \mathbf{Y}(\tau)$ perturbations, on either unstable or stable branch, may be written in the Eq. (B.2) quadrant form.

$$\delta \mathbf{Y}' = \left[\begin{array}{c|cc} \mathbf{A}_{6 \times 6} & \mathbf{0}_{3 \times 1} & \mathbf{0}_{3 \times 1} \\ \hline & \Psi(r_1) \mathbf{r}_1 & \mathbf{0}_{3 \times 1} \\ \mathbf{0}_{2 \times 6} & 0 & 1 \\ & 0 & 0 \end{array} \right] \delta \mathbf{Y} \quad (\text{B.2})$$

Where \mathbf{A} and Ψ are as defined in Eqs. (2.30a)-(2.30b). An augmented state transition matrix, denoted Φ_Y , also exists and satisfies the differential equation $\Phi_Y' = [*] \Phi_Y$, where $[*]$ is the Eq. (B.2) matrix. Therefore, $\Phi_Y(\tau_{j+1}, \tau_j)$ may be obtained via numerical integration over each j segment, with $\Phi_Y(\tau_j, \tau_j) = \mathbf{I}$.

Since \mathbf{C} depends on $\mathbf{X}(\tau_f)$, an intermediary step is to derive the partial derivative of $\mathbf{Y}_f = \mathbf{Y}(\tau_f)$ with respect to $\Delta\mathbf{Y}_j = \Delta\mathbf{Y}(\tau_j)$, for all nodes $j = 1 \dots N$. It is determined readily from the Eq. (4.5) variational expression, that these partials are equal to augmented state transition matrix products, as in Eq. (B.3).

$$\left(\frac{\partial \mathbf{Y}_f}{\partial \Delta \mathbf{Y}_j} \right) = \Phi_{\mathbf{Y}}(\tau_f, \tau_j) \quad (\text{B.3})$$

Next, it is recognized that $\Delta\mathbf{Y}_j$ directly correlates with the j segment $\mathbf{X}_{\mathbf{p}}$ elements, based on the definitions of \mathbf{Y} and $\mathbf{X}_{\mathbf{p}}$. The partial derivative of $\Delta\mathbf{Y}_j$ with respect to the Eq. (B.1) parameter vector, is then given by Eqs. (B.4a)-(B.4b), for impulsive and linear charge control approximations, respectively.

$$\text{Impulsive } (\Delta Q_j) : \quad \left(\frac{\partial \Delta \mathbf{Y}}{\partial \mathbf{X}_{\mathbf{p}}} \right)_j = \begin{bmatrix} \mathbf{0}_{3 \times 1} & \mathbf{0}_{3 \times 3} \\ \mathbf{0}_{3 \times 1} & \mathbf{I}_{3 \times 3} \\ 1 & \mathbf{0}_{1 \times 3} \\ \mathbf{0}_{1 \times 3} & 0 \end{bmatrix} \quad (\text{B.4a})$$

$$\text{Linear } (\dot{Q}_j) : \quad \left(\frac{\partial \Delta \mathbf{Y}}{\partial \mathbf{X}_{\mathbf{p}}} \right)_j = \begin{bmatrix} \mathbf{0}_{3 \times 1} & \mathbf{0}_{3 \times 3} \\ \mathbf{0}_{3 \times 1} & \mathbf{I}_{3 \times 3} \\ 0 & \mathbf{0}_{1 \times 3} \\ 1 & \mathbf{0}_{1 \times 3} \end{bmatrix} \quad (\text{B.4b})$$

With this notation it is then easy to combine Eq. (B.3) with Eqs. (B.4a)-(B.4b) to arrive at the Eq. (B.5) expression for the partial of the final augmented state with respect to the parameter vector.

$$\left(\frac{\partial \mathbf{Y}_f}{\partial \mathbf{X}_{\mathbf{p}}} \right) = \left[\left[\Phi_{\mathbf{Y}}(\tau_f, \tau_1) \left(\frac{\partial \Delta \mathbf{Y}}{\partial \mathbf{X}_{\mathbf{p}}} \right) \right]_{8 \times 4} \cdots \left[\Phi_{\mathbf{Y}}(\tau_f, \tau_N) \left(\frac{\partial \Delta \mathbf{Y}}{\partial \mathbf{X}_{\mathbf{p}}} \right) \right]_{8 \times 4} \right]_{8 \times 4N} \quad (\text{B.5})$$

Since Eq. (B.5) is valid along either unstable or stable branch, and $\mathbf{C} = \mathbf{X}^s(\tau_f) - \mathbf{X}^u(\tau_f)$ with $\mathbf{X} \subset \mathbf{Y}$, the gradient of \mathbf{C} may be written in terms of the expressions in Eqs. (B.4a)-(B.5).

$$\left(\frac{\partial \mathbf{C}}{\partial \mathbf{X}_p} \right) \subset \left[\begin{array}{c|c} - \left(\frac{\partial \mathbf{Y}_f}{\partial \mathbf{X}_p} \right)^u_{8 \times 4N} & \left(\frac{\partial \mathbf{Y}_f}{\partial \mathbf{X}_p} \right)^s_{8 \times 4N} \\ \hline & \left[\begin{array}{c} \mathbf{0}_{3 \times 3} \\ - \mathbf{I}_{3 \times 3} \\ \mathbf{0}_{2 \times 3} \end{array} \right] \end{array} \right]_{8 \times (8N+3)} \quad (\text{B.6})$$

Where the right most quadrant in Eq. (B.6) corresponds to the partial of \mathbf{C} with respect to the final maneuver \mathbf{v}_f (assumed to occur on the unstable branch), and the subset indicates that the first 6 rows of the right hand side matrix are included in \mathbf{C} (the elements of \mathbf{Y} that correspond to \mathbf{X} state variables). It is important to notice that substantial round-off errors can accumulate during numerical integration of $\Phi_Y(\tau_{j+1}, \tau_j)$ matrices and also when forming the sequential products of these matrices, required by Eq. (B.5). Hence, some care is taken to reduce this error via scaling and other numerical techniques.

The cost function gradient is far simpler to derive, since J depends directly on \mathbf{v}_j maneuvers (elements of \mathbf{X}_p). Its gradient is therefore given by Eq. (B.7).

$$\frac{\partial J}{\partial \mathbf{X}_p} = \left[0 \quad \Delta \hat{\mathbf{v}}_1^u \quad 0 \quad \dots \quad \Delta \hat{\mathbf{v}}_N^u \quad 0 \quad \Delta \hat{\mathbf{v}}_1^s \quad 0 \quad \dots \quad \Delta \hat{\mathbf{v}}_N^s \quad \Delta \hat{\mathbf{v}}_f \right]_{1 \times 8N+3} \quad (\text{B.7})$$

Where $\Delta \hat{\mathbf{v}}_j$ denotes a unit vector transpose of an impulsive maneuver $\Delta \mathbf{v}_j$.

Bibliography

- [1] Schaub, H., Parker, G., and King, L., “Challenges and Prospects of Coulomb Spacecraft Formation Control,” *Journal of the Astronautical Sciences*, Vol. 52, No. 1-2, 2004, pp. 169–193.
- [2] Stiles, L., Seubert, C., and Schaub, H., “Effective Coulomb Force Modeling in a Space Environment,” *AAS/AIAA Spaceflight Mechanics Meeting*, No. 12-105, January-February 2012, Charleston, SC.
- [3] Schaub, H. and Hussein, I. I., “Stability and Reconfiguration Analysis of a Circularly Spinning Two-Craft Coulomb Tether,” *IEEE Transactions on Aerospace and Electronic Systems*, Vol. 46, No. 4, 2010, pp. 1675–1686.
- [4] King, L., Parker, C., Deshmukh, S., and Chong, J., “Spacecraft Formation-flying Using Inter-vehicle Coulomb Forces,” Tech. rep., NASA Institute for Advanced Concepts, January 2002.
- [5] Cover, J. H., Knauer, W., and Maurer, H. A., “Lightweight Reflecting Structures Utilizing Electrostatic Inflation,” US Patent 3,546,706, October 1966.
- [6] Saaj, C., Lappas, V., Richie, D., Peck, M., Streetman, B., and Schaub, H., “Electrostatic Forces for Satellite Swarm Navigation and Reconfiguration,” Tech. Rep. ARIADNA 05/4107b., European Space Agency, 2006.
- [7] Mullen, E., Gussenhoven, M., and Hardy, D., “SCATHA,” *Journal of the Geophysical Sciences*, Vol. 91, No. A2, 1986, pp. 1474–1490.

- [8] Whipple, E. and Olsen, R., “Importance of Differential Charging for Controlling Both Natural and Induced Vehicle Potentials on ATS-5 and ATS-6,” *Proceedings of the 3rd Spacecraft Charging Technology Conference*, 1980, pp. 888–893.
- [9] Escoubet, C., Fehringer, M., and Goldstein, M., “The Cluster Mission,” *Annales Geophysicae*, Vol. 19, No. 10/12, 2001, pp. 1197–1200.
- [10] Peck, M., “Prospects and Challenges for Lorentz-Augmented Orbits,” *AIAA Guidance, Navigation, and Control Conference*, August 2005, San Francisco, CA, doi: 10.2514/6.2005-5995.
- [11] Jackson, J., *Classical Electrodynamics*, John Wiley and Sons, 3rd ed., 1999.
- [12] Cosmo, M. and Lorenzini, E., “Tethers in Space Handbook,” Tech. rep., NASA Marshall Space Flight Center, 1997.
- [13] Kong, E., Kwon, D., Schweighart, S., Elias, L., Sedwick, R., and Miller, D., “Electromagnetic Formation Flight for Multisatellite Arrays,” *Journal of Spacecraft and Rockets*, Vol. 41, No. 4, 2004, pp. 659–666.
- [14] Lawson, P. and Dooley, J., “Technology Plan for the Terrestrial Planet Finder Interferometer,” Tech. Rep. 05-5, NASA Jet Propulsion Lab, June 2005.
- [15] Seubert, C., Panosian, S., and Schaub, H., “Attitude and Power Analysis of Two-Node, Multi-Tethered Coulomb Structures,” *Journal of Spacecraft and Rockets*, Vol. 48, No. 6, 2011, pp. 1033–1045, doi: 10.2514/1.52185.
- [16] Moorer, D. and Schaub, H., “Geosynchronous Large Debris Reorbiter: Challenges and Prospects,” *AAS/AIAA Kyle T. Alfriend Astrodynamics Symposium*, No. 10-311, May 2010, Monterey, CA.

- [17] Berryman, J. and Schaub, H., “Analytical Charge Analysis for Two- and Three-Craft Coulomb Formations,” *Journal of Guidance, Control, and Dynamics*, Vol. 30, No. 6, 2007, pp. 1701–1710, doi: 10.2514/1.23785.
- [18] Sobiesiak, L. and Damaren, C., “Hybrid Periodic Differential Element Control Using Geomagnetic Lorentz Force,” *AIAA/AAS Astrodynamics Specialists Conference*, August 2012, Minneapolis, MN, doi: 10.2514/6.2012-4584.
- [19] King, L., Parker, C., Deshmukh, S., and Chong, J., “Study of Interspacecraft Coulomb Forces and Implications for Formation Flying,” *Journal of Propulsion and Power*, Vol. 19, No. 3, 2003, pp. 497–505, doi: 10.2514/2.6133.
- [20] Denton, M., Thomsen, M., Korth, H., Lynch, S., Zhang, J., and Liemohn, M., “Bulk Plasma Properties at Geosynchronous Orbit,” *Journal of Geophysical Research*, Vol. 110, No. A07223, 2005, doi: 10.1029/2004JA010861.
- [21] Schaub, H. and Kim, M., “Differential Orbit Element Constraints for Coulomb Satellite Formations,” *AIAA/AAS Astrodynamics Specialists Conference*, No. 04-5213, August 2004, doi: 10.2514/6.2004-5213.
- [22] Natarajan, A. and Schaub, H., “Hybrid Control of Orbit-Normal and Along-Track Two-Craft Coulomb Tethers,” *AAS/AIAA Space Flight Mechanics Meeting*, No. 07-193, January-February 2007.
- [23] Inampudi, R., *Two-Craft Coulomb Formation Study About Circular Orbits and Libration Points*, Ph.D. thesis, University of Colorado, 2010.
- [24] Natarajan, A., *A Study of Dynamics and Stability of Two-Craft Coulomb Tether Formations*, Ph.D. thesis, Virginia Polytechnic Institute and State University,

2007.

- [25] Pettazzi, L., Kruger, H., Theil, S., and Izzo, D., “Electrostatic Forces for Satellite Swarm Navigation and Reconfiguration,” Tech. Rep. ARIADNA 05/4107a., European Space Agency, 2006.
- [26] Bittencourt, J., *Fundamentals of Plasma Physics*, Springer-Verlag New York, Inc., 2004.
- [27] Clohessy, W. and Wiltshire, R., “Terminal Guidance System for Satellite Rendezvous,” *Journal of the Aerospace Sciences*, Vol. 27, No. 9, 1960, pp. 653–658, doi: 10.2514/8.8704.
- [28] Hogan, E. and Schaub, H., “Collinear Invariant Shapes for Three-Craft Coulomb Formations,” *AIAA/AAS Astrodynamics Specialists Conference*, No. 10-7954, August 2010, Toronto, ON, doi: 10.2514/6.2010-7954.
- [29] Hogan, E. and Schaub, H., “Linear Stability and Shape Analysis of Spinning Three-Craft Coulomb Formations,” *Celestial Mechanics and Dynamical Astronomy*, Vol. 112, No. 2, 2012, pp. 131–148, doi: 10.1007/s10569-011-9387-6.
- [30] Hussein, I. I. and Schaub, H., “Stability and Control of Relative Equilibria for the Three-Spacecraft Coulomb Tether Problem,” *Acta Astronautica*, Vol. 65, No. 5–6, 2009, pp. 738–754, doi: 10.1016/j.actaastro.2009.03.035.
- [31] Wang, S. and Schaub, H., “Nonlinear Charge Control for a Collinear Fixed-Shape Three-Craft Equilibrium,” *Journal of Guidance, Control, and Dynamics*, Vol. 34, No. 2, 2011, pp. 356–366, doi: 10.2514/1.52117.

- [32] Berryman, J. and Schaub, H., “Static Equilibrium Configurations in GEO Coulomb Spacecraft Formations,” *AAS/AIAA Space Flight Mechanics Meeting*, No. 05-104, January 2005, Copper Mountain, CO.
- [33] Wang, S. and Schaub, H., “One-Dimensional 3-Craft Coulomb Structure Control,” *7th International Conference on Dynamics and Control of Systems and Structures in Space*, June 2006, Greenwich, England.
- [34] Jasch, P., Hogan, E., and Schaub, H., “Stability Analysis and Out-of-Plane Control of Collinear Spinning Three-Craft Coulomb Formations,” *AAS/AIAA Spaceflight Mechanics Meeting*, No. 12-151, January-February 2012, Charleston, SC.
- [35] Natarajan, A. and Schaub, H., “Linear Dynamics and Stability Analysis of a Two-Craft Coulomb Tether Formation,” *Journal of Guidance, Control, and Dynamics*, Vol. 29, No. 4, 2006, pp. 831–838, doi: 10.2514/1.16480.
- [36] Lee, D.-H., Kumar, K., and Bang, H., “Formation Flying of Small Satellites Using Coulomb Forces,” *International Journal of Aeronautical and Space Science*, Vol. 7, No. 1, 2006, pp. 84–90, doi : 10.5139/IJASS.2006.7.1.084.
- [37] Parker, G., Passerello, C., and Schaub, H., “Static Formation Control Using Interspacecraft Coulomb Forces,” *2nd International Symposium on Formation Flying Missions and Technologies*, September 2004, Washington, D.C.
- [38] Kennedy, J. and Eberhart, R., “Particle Swarm Optimization,” *Proceedings of the International Conference on Neural Networks*, 1995, pp. 1942–1948, Piscataway, NJ.

- [39] Pontani, M. and Conway, B., “Particle Swarm Optimization Applied to Space Trajectories,” *Journal of Guidance, Control, and Dynamics*, Vol. 33, No. 5, 2010, pp. 1429–1441.
- [40] Gomez, G., Koon, W., Lo, M., Marsden, J., Masdemont, J., and Ross, S., “Connecting Orbits and Invariant Manifolds in the Spatial Restricted Three-Body Problem,” *Nonlinearity*, 2004, pp. 1571–1606, doi: 10.1088/0951-7715/17/5/002.
- [41] Russell, R. and Lam, T., “Designing Ephemeris Capture Trajectories at Europa Using Unstable Periodic Orbits,” *Journal of Guidance, Control, and Dynamics*, Vol. 30, No. 2, 2007, pp. 482–491, doi: 10.2514/1.22985.
- [42] Jones, D. R., “Optimal Reconfiguration of Coulomb Formations Along Invariant Manifolds,” *AAS/AIAA Spaceflight Mechanics Meeting*, No. 12-104, January-February 2012, Charleston, SC.
- [43] Jones, D. R. and Schaub, H., “Collinear Three-Craft Coulomb Formation Stability Analysis and Control,” *AIAA/AAS Astrodynamics Specialists Conference*, No. 12-4721, August 2012, Minneapolis, MN, doi: 10.2514/6.2012-4741.
- [44] Jones, D. R. and Schaub, H., “Optimal Reconfigurations of Two-Craft Coulomb Formations along Manifolds,” *Acta Astronautica*, Vol. 83, No. 1, February-March 2013, pp. 108–118, doi: 10.1016/j.actaastro.2012.10.028.
- [45] Jones, D. R. and Schaub, H., “Collinear Three-Craft Coulomb Formation Stability Analysis and Control,” *Journal of Guidance, Control, and Dynamics*, 2013, Accepted for Publication, February 2013.

- [46] Jones, D. R. and Schaub, H., “Periodic Relative Orbits of Two Spacecraft Subject to Differential Gravity and Electrostatic Forcing,” *Acta Astronautica*, Vol. 89, August-September 2013, pp. 21–30, doi: 10.1016/j.actaastro.2013.03.028.
- [47] Floquet, G., “Sur les quations differentielles linaires coefficients priodiques,” *Annales de l’cole Normale Suprieure*, Vol. 12, 1883, pp. 47–88.
- [48] Meirovitch, L., *Methods of Analytical Dynamics*, McGraw-Hill, 1970, pp. 264–276.
- [49] Szebehely, V., *Theory of Orbits: The Restricted Problem of Three Bodies*, Academic Press, New York, 1967.
- [50] Romanelli, C., Natarajan, A., Schaub, H., Parker, G., and King, L., “Coulomb Spacecraft Voltage Study Due to Differential Orbital Perturbation,” *AAS/AIAA Space Flight Mechanics Meeting*, January 2006, Tampa, FL.
- [51] Duffin, W., *Electricity and Magnetism*, John Wiley and Sons, New York, NY, 2nd ed., 1973, pp. 83–85.
- [52] Norman, M. and Peck, M., “Integrals of Motion for Planar Multi-Body Formations with Internal Forces,” *Journal of Guidance, Control, and Dynamics*, Vol. 34, No. 6, 2011, pp. 1790–1797.
- [53] Vadali, S., Schaub, H., and Alfriend, K., “Initial Conditions and Fuel-Optimal Control for Formation Flying of Satellites,” *AIAA Guidance, Navigation, and Control Conference*, August 1999, Portland, OR.
- [54] Perko, L., *Differential Equations and Dynamical Systems*, Springer, 1996, pp. 199–206.

- [55] Guckenheimer, J. and Holmes, P., *Nonlinear Oscillations, Dynamical Systems, and Bifurcations of Vector Fields*, Springer, New York, 1997, pp. 10–16.
- [56] Kailath, T., *Linear Systems*, Prentice-Hall, Inc., 1980, Chap. 9.
- [57] Perko, L., *Differential Equations and Dynamical Systems*, Springer, 1996, pp. 119–130.
- [58] Hull, D. G., *Optimal Control Theory for Applications*, Springer, 2003, pp. 1–14.
- [59] Hull, D. G., *Optimal Control Theory for Applications*, Springer, 2003, pp. 350–352.
- [60] Nocedal, J. and Wright, S., *Numerical Optimization*, Springer, 2006, Chap. 18.
- [61] *Harwell Subroutine Library*, 2013, release 1995, routine VF13ad, [online database], URL: www.hsl.rl.ac.uk/archive/hslarchive.html [retrieved 20 January 2009].
- [62] Slane, J. H., *Analysis of Periodic Nonautonomous Inhomogeneous Systems with Application to Tethered Satellite Systems*, Ph.D. thesis, University of Colorado at Colorado Springs, 2010.
- [63] Meirovitch, L., *Methods of Analytical Dynamics*, McGraw-Hill, 1970, pp. 219–222.
- [64] Ocampo, C. and Munoz, J., “Variational Equations for a Generalized Spacecraft Trajectory Model,” *Journal of Guidance, Control, and Dynamics*, Vol. 33, No. 5, 2010, pp. 1615–1622, doi: 10.2514/1.46953.
- [65] Battin, R., *An Introduction to the Mathematics and Methods of Astrodynamics*, AIAA Education Series, 1999, Chapter 7.

- [66] Kailath, T., *Linear Systems*, Prentice-Hall, Inc., 1980, pp. 205–206.
- [67] Tsui, C.-C., *Robust Control System Design: Advanced State Space Techniques*, Marcel Dekker, New York, 2nd ed., 2004, pp. 13–14, 221–226.
- [68] Boley, D. and Lu, W.-S., “Measuring How Far a Controllable System is from an Uncontrollable One,” *IEEE Transactions on Automatic Control*, Vol. 31, No. 3, 1986, pp. 249–251.
- [69] Alfriend, K., Vadali, S., and Wilkins, M., “Dynamics and Control of Powersail,” *AAS/AIAA Spaceflight Mechanics Meeting*, No. 01-230, February 2001, Santa Barbara, CA.
- [70] Cooley, J. and Tukey, J., “An Algorithm for the Machine Computation of the Complex Fourier Series,” *Mathematics of Computation*, Vol. 19, April 1965, pp. 297–301.

Vita

Drew Ryan Jones was born near Tucson, Arizona in 1985. Upon graduation from Benson Union High School in May 2003, he attended Arizona State University on a full tuition scholarship. In May 2008, Drew completed his B.S.E. in Aerospace Engineering. Afterward he transferred to The University of Texas at Austin (UT), to pursue research in orbital mechanics, earning an M.S.E. degree in Aerospace Engineering, in May 2010. Shortly thereafter, he was honored with the National Defense Science and Engineering Graduate (NDSEG) Fellowship, which provided a majority of the financial support for this dissertation.

Drew worked throughout his post-secondary education, holding positions with Honeywell Aerospace, NASA, the Applied Physics Laboratory, and as a UT Teaching Assistant. He also participated in the 4th and 6th international Global Trajectory Optimization Competitions (GTOC), and worked as a Research Assistant. In the latter role, he helped to develop fuel-optimal, Moon to Earth abort trajectories, in concert with NASA-JSC. His diverse research interests include optimal space trajectories, nonlinear dynamical systems, low-thrust optimal control problems, multiple flyby moon tours, and formation flying. Drew married Ashlee on January 5th 2013 in Arizona. And in July 2013, they will relocate to Pasadena, California, where Drew has accepted a position at the Jet Propulsion Laboratory.

Permanent address: 404 Rio Grande ST, APT 32
Austin, Texas 78701

This dissertation was typeset by the author.